Indian J Pure & Appl Phys, Vol 21 No 10 pp 555-618
OCTOBER 1983
CODEN : IJOPAU ISSN : 0019-5596
21(10) 555-618 (1983)

INDIAN JOURNAL OF PURE & APPLIED PHYSICS

1048
Dat 25/1/84

Published by
PUBLICATIONS & INFORMATION DIRECTORATE, CSIR
NEW DELHI
in association with
THE INDIAN NATIONAL SCIENCE ACADEMY, NEW DELHI

Let the facts speak...

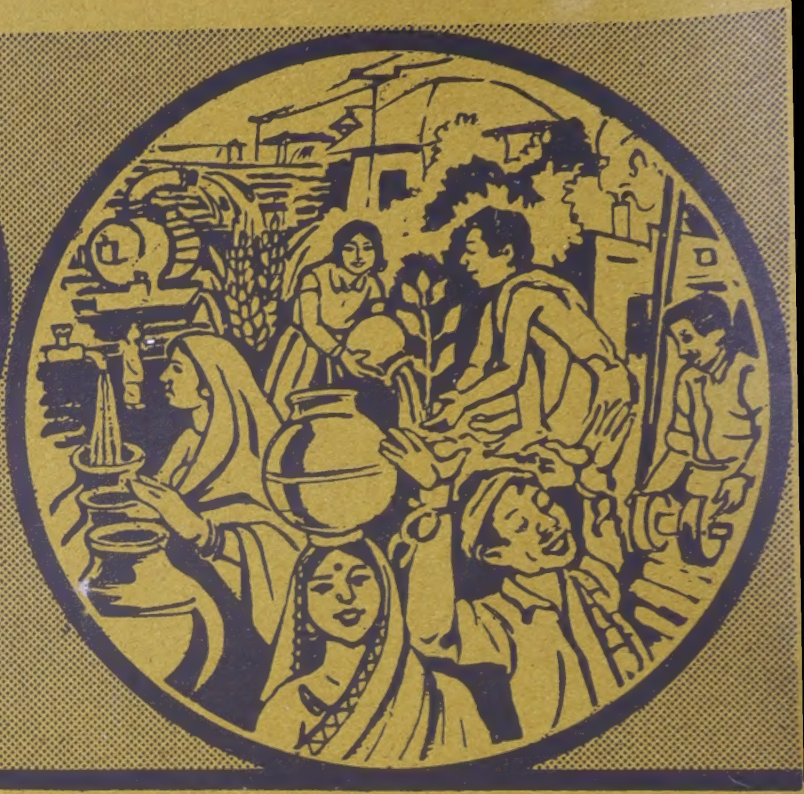

We can be justly proud of the encouraging achievements of the Revised 20-Point Programme—the blueprint for progress and prosperity for the masses. The programmes in which we attained 100 per cent (or more) of the target set out for 1982-83 include:

- Extension of irrigation facilities;
- Integrated Rural Development;
- Rehabilitation of bonded labour;
- Welfare of Scheduled Castes and Scheduled Tribes;
- Drinking water facilities in problem villages;
- Tree plantation; and
- Integrated Child Development Service Blocks.

The administrative machinery, both at the Centre and in the States, has been geared for achieving results at the field level.

With determination and hard work, we can achieve much more.

COME, LET US JOIN HANDS TO FULFIL THE TARGETS OF THE REVISED 20-POINT PROGRAMME

davp: 83 223

RENEWAL NOTICE

Your subscription which expires with the despatch of December 1983 issue of the journal, stands for renewal. We request you to be so good as to return the enclosed order form duly filled early, so as to ensure continuity in despatch.

Manager (Sales & Advertisement)

DATED:

The Manager (Sales & Advertisement)

To our Subscribers

Due to production cost having gone up enormously, we are constrained to make a nominal increase in the rates of subscription for our periodicals.

We have so far done whatever we could to absorb the cost increases for several years without in any way compromising with the quality and standard of the journals. A stage has now come when this is no longer possible and we are obliged to effect the increase. We trust our valued subscribers will appreciate the situation and stand by us as heretofore.

The revised rates for the **Indian Journal of Pure & Applied Physics from January 1984** will be as follows:

Annual Subscription	Rs. 180.00	$ 60.00	£ 34.00
Single Copy	Rs. 18.00	$ 6.00	£ 3.40

a sum of Rs ..... £ ..... $ ..... by Cheque/Demand Draft No. ..... dated ..... in favour of PUBLICATIONS & INFORMATION DIRECTORATE, NEW DELHI.

COMPLETE MAILING ADDRESS

Name .....

Address .....

Country/State .....

(Signature)

Note:

1. Subscribers at annual rates for all the periodicals are enlisted for the full volumes, i.e. for the period from January to December only.
2. The Cheque/Demand Draft may plese be drawn in favour of "PUBLICATIONS & INFORMATION DIRECTORATE, NEW DELHI". Banking charges shall be borne by the subscriber. For inland outstation cheques please add Rs. 3.50. For foreign cheques please add $ 1.00 or £ 0.45.
3. The supply will commence on receipt of subscription in advance.

Indian Journal of Pure & Applied Physics

EDITORIAL BOARD

Prof. D Basu
Indian Association for the Cultivation of Science
Calcutta

Prof. B Buti
Physical Research Laboratory
Ahmedabad

Prof. S C Dutta Roy
Indian Institute of Technology
New Delhi

Dr R Hradaynath
Instruments Research & Development Establishment Dehra Dun

Prof. D Premaswarup
Nagarjuna University
Nagarjuna Nagar

Prof. A N Mitra
Indian National Science Academy
New Delhi/University of Delhi
Delhi

Prof. Probir Roy
Tata Institute of Fundamental Research
Bombay

Prof. E S Raja Gopal
Indian Institute of Science
Bangalore

Prof. G Rajasekaran
Madras University
Madras

Dr A P B Sinha
National Chemical Laboratory
Pune

Prof. C V Vishveshwara
Raman Research Institute
Bangalore

Prof. M S Sodha
Indian National Science Academy
New Delhi/Indian Institute of Technology New Delhi

Shri Y.R. Chadha, Editor-in-Chief, *Ex-officio* Secretary

EDITORIAL STAFF

Editors

D S Sastry, K S Rangarajan & R P Goel

Assistant Editors

G N Sarma, J B Dhawan & Tarun Banerjee

Scientific Assistant

(Mrs) Poonam Bhatt

Published by the Publications & Information Directorate, CSIR, Hillside Road, New Delhi 110012
Editor-in-Chief : Y R Chadha

The Indian Journal of Pure & Applied Physics is issued monthly. The Directorate assumes no responsibility for the statements and opinions advanced by contributors. The editorial staff in its work of examining papers received for publication is assisted, in an honorary capacity, by a large number of distinguished scientists, working in various parts of India.

Communications regarding contributions for publication in the journal should be addressed to the Editor, Indian Journal of Pure & Applied Physics, Publications & Information Directorate, Hillside Road, New Delhi 110012.

Correspondence regarding subscriptions and advertisements should be addressed to the Sales & Distribution Officer, Publications & Information Directorate, New Delhi 110012.

Annual Subscription
Rs. 120.00 £20.00 $45.00

Single Copy
Rs. 12.00 £2.00 $4.50

50% Discount is admissible to research workers and students and 25% discount to non-research individuals, on annual subscription. Payments in respect of subscriptions and advertisements may be sent by cheque, bank draft. money order or postal order marked payable *only* to **Publications & Information Directorate, New Delhi 110012**. Claims for missing numbers of the journal will be allowed only if received within 3 months of the date of issue of the journal plus the time normally required for postal delivery of the journal and the claim.

© 1983 The Council of Scientific & Industrial Research, New Delhi.

Indian Journal of Pure & Applied Physics

VOLUME 21 NUMBER 10 OCTOBER 1983

CONTENTS

Solid State Physics

Effect of Film Thickness on Electrical Resistivity of Thin Antimony Films 555
A A El-Shazly*, M M Ibrahim & M M El-Nahass

A Computer Study of the Crystal Orientation Dependence of Avalanche Zone Width and Efficiency of Single-Drift and Double-Drift GaAs IMPATT Diodes 558
S P Pati, J P Banerjee & S K Roy*

Analysis of the Absorption Spectra of CdS Thin Films Using Annealing Technique ... 563
K K Dey*, U K Chaturvedi & A K Chatterjee

Rotational Barrier Height and Off-center of Mass Displacement for Hydroxyl Ion in Alkali Halide Crystal Matrices 569
Lalan Jha* & Hare Krishna Jha

Frequency & Temperature Dependence of Dielectric & Electromechanical Parameters of Soft Piezoelectric Materials Developed at NPL 573
G C Jain, V N Bindal*, Janardan Singh, Ved Singh, N Narayana Swami & N C Soni

Chemical Physics

Isentropic Compressibilities from Ultrasonic Studies on Binary Mixtures of di-*n*-Butylamine with *n*-Alcohols 579
M Ramamurthy, G S Sastry & P R Naidu*

Radiation Damage in Some Synthetic High Polymers 582
M Ramakrishna Murthy* & S Radhakrishna

Optics

Parallel Plate Interferometer for the Precise Measurement of Radius of Curvature of a Test Plate & Focal Length of a Lens System 587
M V R K Murty & R P Shukla*

Design of Dipping Refractometer with Indian Optical Glasses 592
B N Gupta* & A K Garg

Spectroscopy

Thermal Emission Spectrum of NiCl Molecule in Violet Region 595
R Gopal* & M M Joshi

NOTES

Switching in Single Crystals of the (Mo/W)Se_2 System 599
M K Agarwal*, P D Patel & O Vijayan

Behaviour of Nitrogen in $GaAs_{1-x}P_x$ ($x \geq 0.86$) 602
M Mounir* & N Nartdinov

Continued overleaf

Unit Cell and Space Group Determination of Sesebrinol ($C_{20}H_{26}O_6$) 604
S D Sharma & K N Goswami*

Calculations of Geometry & Molecular Properties by Semiempirical Molecular Orbital Method (SINDO) 605
C P D Dwivedi

Rotational Collision Numbers for Carbon Dioxide 609
P C Jain

Structural Studies on Some Organic Polar Compounds Using Microwave Absorption Technique and NMR 611
Ambesh Srivastava & N K Mehrotra*

Evaluation of Electron Temperature in Glow Discharge from Measurement of Diffusion Voltage 613
S N Sen*, S K Ghosh & B Ghosh

Excitation Energy-dependent Features in the *M*-X-ray Emission Spectrum of Cerium ... 615
K S Srivastava*, Kirti Sinha, A K Srivastava & M Husain

New Spectrum of NiCl Molecule 617
P M Shah, A B Darji* & N R Shah

---

*The author for correspondence is indicated by (*) mark in case of papers with more than one author

Indian Journal of Pure & Applied Physics
Vol. 21, October 1983, pp. 555-557

Effect of Film Thickness on Electrical Resistivity of Thin Antimony Films

A A El-SHAZLY, M M IBRAHIM & M M El-NAHASS
Faculty of Education, Ain Shams University, Cairo, ARE

Received 25 *October* 1982; *revised received* 31 *May* 1983

The electrical resistivity of thin antimony films has been measured as a function of film thickness in the range 400-1800 Å. The experimental results are in good agreement with Mayadas and Shatzkes and Fuchs-Sondheimer theories for lower and higher film thicknesses respectively. The measurements on the temperature dependence of the electrical resistivity show that Sb films always have positive temperature coefficient. The mean free path has been calculated at different temperatures.

1 Introduction

Metallic thin films, due to their structural features and size effects, have properties somewhat different from those of bulk materials. Accordingly, extensive work has been carried out on the physical properties, mainly the electrical properties of thin films of noble metals. However, not much work seems to have been done on the electrical properties of thin antimony films.

In the present work, the effect of film thickness on electrical resistivity of thin Sb films over the thickness range 400-1800 Å has been investigated. An attempt has been made to fit our experimental data to the Fuchs-Sondheimer (FS)[1,2] and Mayadas and Shatzkes (MS)[3] theories. The temperature coefficient of the electrical resistivity of such films has also been determined. Assuming the specularity parameter as equal to zero, the mean free path of the charge carriers at different temperatures has been calculated.

2 Experimental Procedure

Clean glass substrate held at room temperature was placed tangentially to a suitable holder with rotating speed of 240 r.p.m. to produce good film thickness distribution. A molybdenum boat was charged with antimony granules (purity 99.999%) and the vacuum chamber was pumped down to 10^{-5} Torr. The boat was gradually heated until the material started evaporating. A shutter was used during this operation, which was later removed to grow films at the deposition rate of 20 Å/sec. The film thickness was controlled using a crystal quartz monitor, and was measured by the multiple-beam Fizeau fringes method[4].

The electrical resistivity of the Sb specimens was measured either at room temperature or at elevated temperatures using the four-probe method[5].

3 Results and Discussion

The electrical resistivity of thin films can be expressed as[6]:

$$\rho = \rho_0 \left[1 + \frac{3L}{8t}(1-P) \right] \quad \ldots (1)$$

where ρ is the electrical resistivity of the thin film, ρ_0 the electrical resistivity of the bulk material, L the electron mean free path, t the film thickness and P the specularity parameter.

The experimentally measured resistivity of thin films as shown by Mayadas and Shatzkes[3] is dependent not only on the ordinary Fuchs size effect but also on the effect of grain boundary scattering. The thin film electrical resistivity given by MS for small α' is

$$\rho = \rho_0 \left[1 + \frac{3}{2}\alpha' + \frac{3L}{8t}(1-P) \right] \quad \ldots (2)$$

where $\alpha' = LR/d(1-R)$. Here d is the average grain diameter and R the grain boundary reflection coefficient. Fig. 1 illustrates the electrical resistivity measured at room temperature as a function of the film thickness t. As shown, the electrical resistivity is high for low thicknesses and attains nearly a constant value beyond a thickness of 1800 Å. We did not observe continuity of the Sb films for thicknesses less than 400 Å.

Fig. 2 show ρt as a function of t[using Eq. (1)]. The intercept of this graph on the y-axis yields $L(1-P)$ while the slope yields ρ_0 which is the electrical resistivity of an infinitely thick film.

Assuming $P=0$ for total diffuse scattering, we obtain the value of L in Sb films as 1322 Å.

Assuming that the values of ρ_0 and $L(1-P)$ derived from Fuchs model are also appropriate for the MS model, Eq. (2) has been used for estimating the value of α' for two thicknesses, viz. 400 Å and 600 Å. Further,

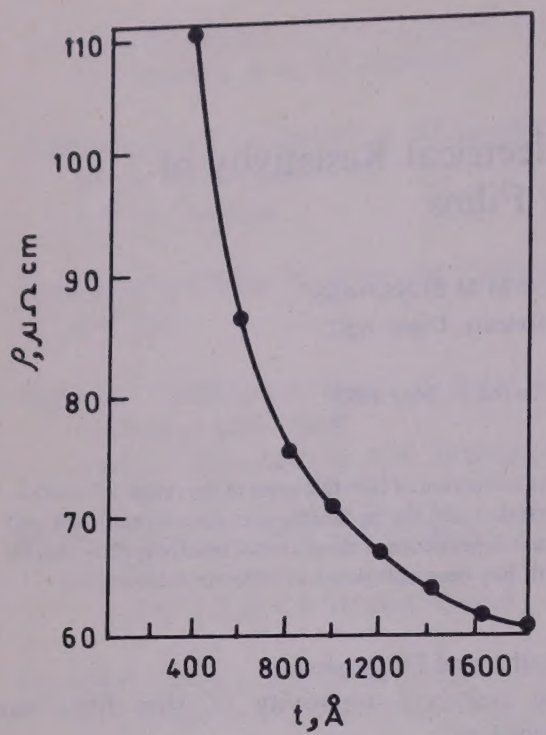

Fig. 1—ρ versus t at room temperature

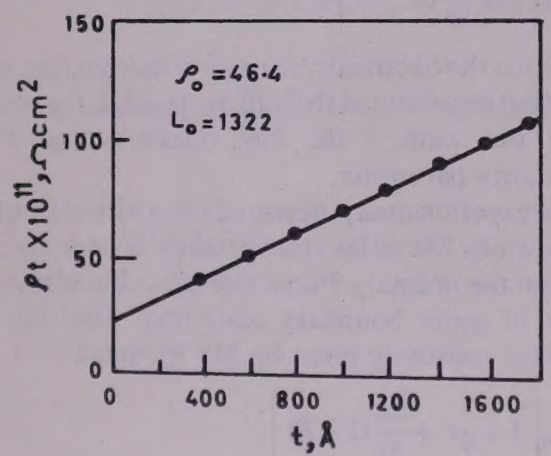

Fig. 2—ρt versus t at 303 K

the values of R have been calculated on the assumption that the grain diameter approximately equals the film thickness.

Data for ρ_0, L, t and R are given in Table 1.

The measurements of the temperature dependence of the electrical resistivity showed that Sb films (600-1600 Å thick) always have positive temperature coefficient.

Applying the assumptions of FS and MS theories, the temperature coefficient of the resistivity α can be expressed as[6]:

$$\alpha = \alpha_g \left[1 - \frac{3}{8} \frac{L_g}{t} (1 - P) \right] \quad \ldots (3)$$

where α_g and L_g are the effective intrinsic values for the temperature coefficient of resistivity and electron mean free path respectively (see Appendix A).

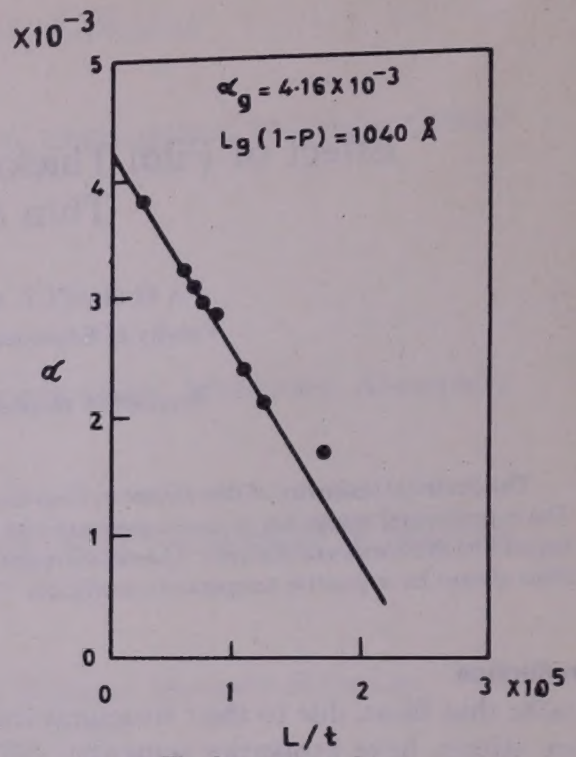

Fig. 3—α versus L/t

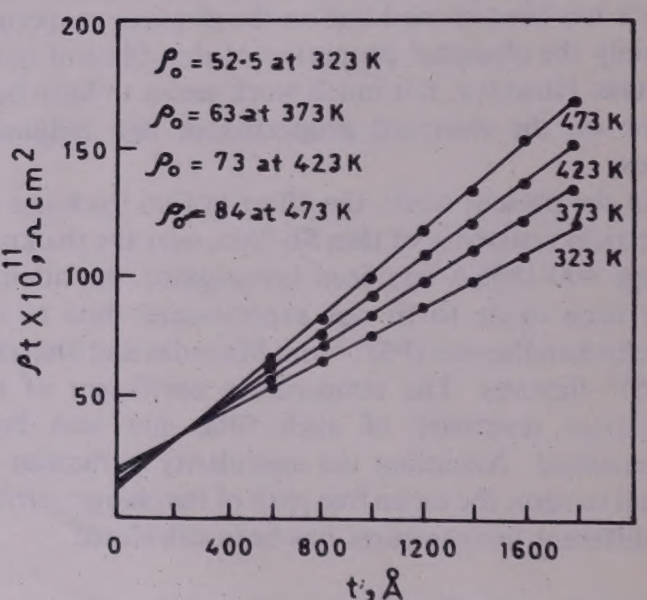

Fig. 4—ρt versus t at different temperatures

Table 1—Values of ρ_0, L, t and R at Room Temperature

ρ_0 $\mu\Omega$-cm	L Å	t Å	R
46.4	1322	400	0.026
		600	0.012

Table 2—Values of L and ρ_0 at Different Temperatures

Temp. K	L Å	ρ_0 $\mu\Omega$-cm
303	1322	46.6
323	1117	52.5
373	847	63.0
423	658	73.0
473	508	84.0

Fig. 3 shows α as a function of L/t. From Fig. 3, the values of α_g and $L_g(1-P)$ were found to be 4.16×10^{-3} per degree and 1040 Å respectively.

The values of L of the conduction electrons were determined at different temperatures according to Eq. (1) with $P=0$ (Fig. 4). The values of L decrease as the temperature increases, while the bulk resistivity ρ_0 increases. Data for L and ρ_0 at different temperatures are given in Table 2.

4 Conclusion

Electrical resistivity measurements conducted on vacuum-evaporated Sb films in the thickness range 400-1800 Å and temperature range 303-473 K show metallic behaviour of the films deposited.

Appendix A

The electrical conductivity of thin films can be expressed as*:

$$\frac{\sigma}{\sigma_0}=1-\frac{3}{4}\left(k-\frac{k^3}{12}\right)E_i(-k)$$

$$-\frac{3}{8k}(1-e^{-k})-\left(\frac{5}{8}+\frac{k}{16}-\frac{k^2}{16}\right)e^{-k} \qquad \ldots \text{(i)}$$

where σ is the conductivity of the film, σ_0 the conductivity of the bulk metal, $k=t/L$ (t is the film thickness and L the electron mean free path in the bulk) and

$$-E_i(-k)=\int_{-\infty}^{\infty}(e^{-x}/t)dt$$

A more convenient form of the expression for the conductivity is given as:

$$\left(\frac{\sigma}{\sigma_0}\right)_{k,P}=(1-P)^2\sum_{n=1}^{\infty}nP^{n-1}\left(\frac{\sigma}{\sigma_0}\right)_{nk,P=0} \qquad \ldots \text{(ii)}$$

where P is the specularity parameter and $(\sigma/\sigma_0)_{nk,P=0}$ is given by Eq. (i) with k replaced by nk. The limiting form of this expression for relatively thick film is

$$\frac{\sigma}{\sigma_0}=1-\left[\frac{3(1-P)}{8k}\right]=1-\frac{3L(1-P)}{8t} \qquad \ldots \text{(iii)}$$

Similarly $\dfrac{\sigma}{\sigma_g}=1-\dfrac{3L_g(1-P)}{8t}$

The temperature coefficient of resistivity is

$$\alpha=\frac{1}{\rho}\frac{d\rho}{dT}$$

and the k dependence of the temperature coefficient of resistivity may be easily calculated if the resistivity is given as:

$\rho=\rho_0 f(k)$

where $f(k)$ is an arbitrary function of k.

It is easy to show that $dk/dt=k_0$ and hence

$$\frac{\alpha}{\alpha_0}=1+\left(\frac{d\ln\rho}{d\ln k}\right)=1-\left(\frac{d\ln\sigma}{d\ln k}\right) \qquad \ldots \text{(iv)}$$

where α_0 is the bulk temperature coefficient of resistivity. Using this expression for α/α_0 when $P<1$, the limiting expression for relatively thick films may be obtained from Eq. (iii), as

$$\frac{\alpha}{\alpha_0}=\frac{\sigma}{\sigma_0}=1-\frac{3L(L-P)}{8t}$$

as $\alpha/\alpha_g=\sigma/\sigma_g$

Thus using Eq. (iv) one can get,

$$\frac{\alpha}{\alpha_g}=1-\frac{3L_g(L-P)}{8t}$$

* Larson D, Phys Thin Film (USA), 6 (1971) 94.

References

1 Fuchs K, *Proc Cambridge Philos Soc (GB)*, **34** (1938) 100.
2 Sondheimer E H, *Adv Phys (GB)*, **1** (1952) 1.
3 Mayadas A F & Shatzkes M, *Phys Rev B (USA)*, **11** (1970) 1382.
4 Tolansky S, *Philos Mag (GB)*, **30** (1945) 225.
5 Valdes L B, *Proc IRE (USA)*, **42** (1954) 420.
6 Campbell D S, in *The use of thin films in physical investigations*, edited by J C Anderson (Academic Press, New York), 1966, 299.

Indian Journal of Pure & Applied Physics
Vol. 21, October 1983, pp. 558-562

A Computer Study of the Crystal Orientation Dependence of Avalanche Zone Width and Efficiency of Single-Drift and Double-Drift GaAs IMPATT Diodes

S P PATI, J P BANERJEE & S K ROY
Centre of Advanced Study in Radio Physics and Electronics, University of Calcutta, 1 Girish Vidyaratna Lane Calcutta 700009

Received 23 *August* 1982; *revised received* 7 *December* 1982

A computer study of the field and carrier current profiles and associated dc properties governing the microwave performance of ⟨111⟩, ⟨110⟩ and ⟨100⟩, oriented, flat-profile, single-drift p^+nn^+, n^+pp^+ and double-drift n^+npp^+ IMPATT structures, has been carried out for different donor and acceptor concentrations using Pearsal's ionization rate data for GaAs. The calculations show that p^+nn^+ GaAs IMPATTs have narrowest avalanche zone for ⟨111⟩ orientation which, in turn, should provide higher conversion efficiency and rf power delivery from the device as compared to those for other orientations. It has been observed that the properties of p^+nn^+ SDR diode depend strongly on orientation while those of the n^+pp^+ SDR diode are only slightly dependent on orientation. For double-drift n^+npp^+ diode, ⟨111⟩ emerges as the best orientation; but the efficiency of ⟨111⟩ oriented p^+nn^+ SDR exceeds that of similarly-oriented DDR device for X-band structures.

1 Introduction

The ionization rate of charge carriers in a semiconductor is one of the principal parameters which governs the dc and microwave properties of IMPATT diodes. Studies on noise of avalanche photodiodes and microwave properties of high efficiency GaAs IMPATTs indicated inequality of the ionization rates (α_n, α_p) of electrons and holes. This inequality of carrier ionization rates was later on experimentally verified by Stillman *et al.*[1] and Ito *et al.*[2] In 1978, the measurements made by Pearsall *et al.*[3] showed that the ionization rates of electrons and holes for different crystal orientations, i.e. ⟨111⟩, ⟨110⟩ and ⟨100⟩, are different. The ratio α_p/α_n is greater than unity for ⟨111⟩ and ⟨100⟩ directions while that for ⟨110⟩ direction is slightly less than unity. The difference between hole and electron ionization rates is maximum for ⟨111⟩ orientation. These ionization rate data were used by Lee and Sze[4] for the calculation of diode voltage of ⟨100⟩, ⟨110⟩ and ⟨111⟩ oriented GaAs abrupt *p-n* junction at breakdown for different background doping. The purpose of the present work is to study the effect of crystal orientation on the dc and microwave properties of different GaAs IMPATT structures in the presence of mobile space charge. Using appropriate ionization rate data[3] for different orientations, the field and carrier current profiles in the depletion region of various structures have been computed for ⟨111⟩, ⟨110⟩ and ⟨100⟩ orientations. These profiles have been used to study the dependence of avalanche layer width and efficiency of p^+nn^+, n^+pp^+ and n^+npp^+ GaAs diodes on crystal orientation of the active region. The computation shows that ⟨111⟩ oriented p^+nn^+ GaAs diodes have thinnest avalanche zone and the efficiency of such structure surpasses that of double-drift structures in the *X*-band.

2 Theory

A double iterative computer method which involves iterations over the magnitude of the field maximum (E_m) and its location in the depletion layer[5] has been employed for simultaneous numerical solution of Poisson and continuity equations satisfying the boundary conditions at the edges of the depletion layer. Realistic doping profiles have been used for the computation which incorporate appropriate exponential and error functions at the junction and at the interface of the epitaxy and substrate. The effect of mobile space charge in the depletion layer has been taken into account while computing the profiles. The field variation of ionization rates for different orientations has been obtained from Pearsal *et al.*[3] The electron velocity is obtained from Kramer and Mircea[6], and is given by the expression

$$v_n(E) = \frac{[\mu_n E(x) + v_{sn}(E(x)/E_c)^4]}{[(1 + E(x)/E_c)^4]}$$

The hole velocity as a function of electric field has an exponential field dependence[7] and can be fitted to an expression

$$v_p(E) = v_{sp}[1 - \exp(\mu_p E(x)/v_{sp})]$$

The fundamental equations involved in the computer calculation are Poisson's equation given by

$$\frac{dE}{dx} = \frac{q}{\varepsilon}(N_D - N_A + p - n) \quad \ldots (1)$$

and combined carrier continuity equation given by

$$\frac{\partial}{\partial x}\left(\frac{J_p - J_n}{J_0}\right) = (\alpha_n + \alpha_p) - (\alpha_n - \alpha_p)\left(\frac{J_p - J_n}{J_0}\right) \quad \ldots (2)$$

where $J_0 = (J_n + J_p)$ is the total dc current density. The carrier current density due to both drift and diffusion is given by

$$J_p = qpv_p - qD_p\frac{dp}{dx} \quad \ldots (3)$$

$$J_n = qnv_n + qD_n\frac{dn}{dx} \quad \ldots (4)$$

The diffusion component of carrier current density is small relative to the drift component except near the avalanche region where diffusion current would be appreciable fraction of the drift current. However, perturbation technique has been used to obtain the following equations for electron and hole density in the depletion layer from Eqs (3) and (4):

$$p = \frac{J_p}{qv_p} + \frac{D_p}{qv_p^2}\ddot{J}_p + \frac{D_p^2}{qv_p^3}\dddot{J}_p + \frac{D_p^3}{qv_p^4}\bar{J}_p \text{ and}$$

$$n = \frac{J_n}{qv_n} - \frac{D_n}{qv_n^2}\ddot{J}_n + \frac{D_n^2}{qv_n^3}\dddot{J}_n - \frac{D_n^3}{qv_n^4}\bar{J}_n \quad \ldots (5)$$

(where dot represents derivative with respect to x). J_p, J_n and their higher derivatives are obtained from the transport equations. $D_n(E)$ is obtained from Kramer and Mircea[6] and the value[8] of D_p is taken to be 20 cm^2s^{-1}.

Considering the origin ($x=0$) of the distance co-ordinate in the depletion layer to be the plane of the metallurgical junction, the boundary conditions for electric field and carrier current densities at the n-side and p-side edges ($-x_1$ and x_2) of the depletion layer are respectively given by

$$E(-x_1) = 0, \left(\frac{J_p - J_n}{J_0}\right)_{x=-x_1} = \frac{2J_{ps}}{J_0} - 1 = \frac{2}{M_p} - 1$$

and

$$E(x_2) = 0, \left(\frac{J_p - J_n}{J_0}\right)_{x=x_2} = 1 - \frac{2J_{ns}}{J_0} = 1 - \frac{2}{M_n}$$

where $M_p (= J_0/J_{ps})$ and $M_n (= J_0/J_{ns})$ are the hole and electron multiplication factors. J_{ps} and J_{ps} are the reverse saturation hole and electron currents at the edges of the depletion layer and J_0 is the total bias current density. M_n and M_p are large numbers and usually greater than 10^5 under breakdown condition, so that the boundary conditions can be written as

$$\left(\frac{J_p - J_n}{J_0}\right)_{x=-x_1} \simeq -1 \text{ and } \left(\frac{J_p - J_n}{J_0}\right)_{x=x_2} \simeq 1$$

Field and carrier current profiles have been obtained from simultaneous numerical solution of Eqs (1) and (2) with one thousand space steps. The width of avalanche zone (x_A) is obtained as the distance between two points on either side of the junction where $|J_p - J_n| = 0.95J_0$. The breakdown voltage (V_B), voltage drops across drift zone (V_D) and avalanche zone (V_A) have been obtained from numerical integration of the field profile over the respective regions. Thinner avalanche zone and lower avalanche voltage drop lead to higher dc to microwave conversion efficiency (η) and a qualitative estimation of the same has been obtained by using Scharfetter and Gummel's semiquantitative formula involving dc voltage drops across the drift and the avalanche zone.

3 Results

Studies on flat profile single-drift p^+nn^+, its complementary n^+pp^+ and symmetrically doped double-drift n^+pp^+ GaAs diodes for $\langle 111\rangle$, $\langle 110\rangle$ and $\langle 100\rangle$ orientations have been carried out, using computer solution of field and carrier current profiles in the depletion layer of the devices. The calculations for $E(x)$, $[J_p(x) - J_n(x)]/J_0$ have been carried out for values of background doping concentration (N_A or N_D) of p or n regions in the range of $10^{22}/m^3$ to $10^{23}/m^3$ at a dc current density (J_0) or 10^7 A/m^2, and the extensions of the depletion layer are so adjusted that the devices are just non-punch through (considering the effect of mobile space charge). The maximum electric field (E_m), the ratio of avalanche to depletion layer width (x_A/W), and the voltage drops V_A, V_D have been computed. The results are shown in Table 1 for three different values of doping concentrations, which would approximately correspond to three frequencies of operation at 10, 35 and 50 GHz.

The field and carrier current profiles in the depletion regions of SDR p^+nn^+, n^+pp^+ and DDR n^+npp^+ diodes are shown in Figs 1, 2 and 3 respectively for

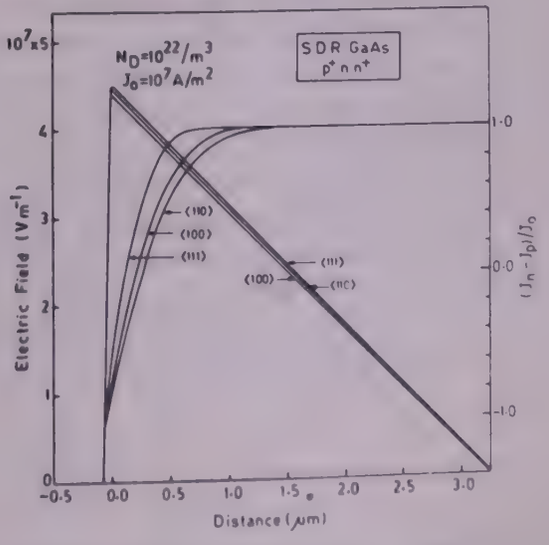

Fig. 1—Electric field and current density profiles of single-drift GaAs p^+nn^+ diode for different orientations

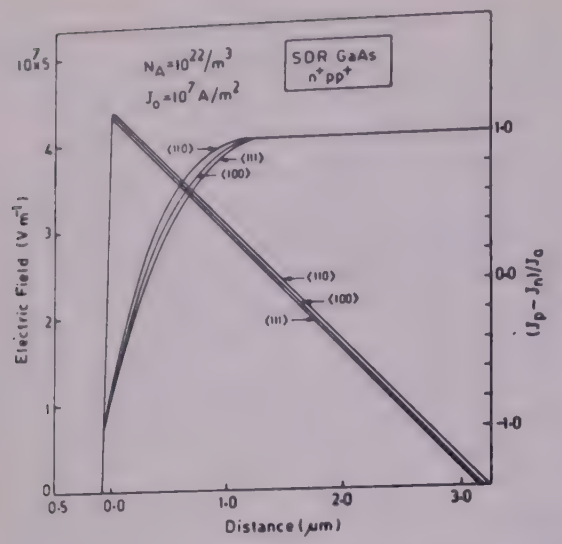

Fig. 2—Electric field and current density profiles of single-drift GaAs n^+pp^+ diode for different orientations

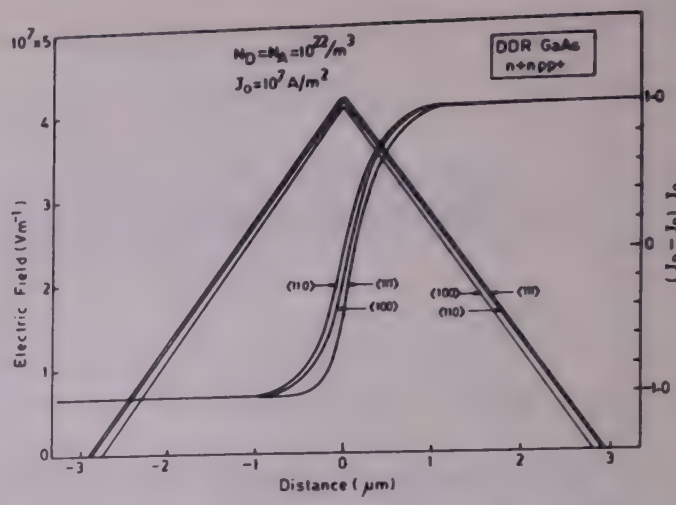

Fig. 3—Electric field and current density profiles of double-shift GaAs n^+npp^+ diode for different orientations

different orientations (i.e. ⟨111⟩, ⟨110⟩ and ⟨100⟩) of the diodes having $N_A = N_D = 10^{22}/m^3$ at $J_0 = 10^7\ A/m^2$. The value of η for ⟨111⟩, ⟨110⟩ and ⟨100⟩ oriented GaAs IMPATT structures has been plotted against doping concentration in Fig. 4. As seen from Figs 1, 2 and 3 the effect of crystal orientation is more pronounced on carrier current profiles than that on the field profiles. Table 1 and Fig. 1 show that the avalanche zone of SDR p^+nn^+ diode is thinnest for ⟨111⟩ orientation as compared to ⟨110⟩ and ⟨100⟩ orientations. For example x_A/W in case of ⟨111⟩ oriented p^+nn^+ diode is only 18.1% while the same for ⟨110⟩ and ⟨100⟩ oriented diodes are 34.0% and 28.1% respectively for a doping concentration of $10^{22}/m^3$. The output high-frequency power from the device at any current density is proportional to the product of diode voltage (V_B) and efficiency ($\simeq(1/\pi)(V_D/V_B)$ and can be qualitatively estimated from the voltage drop across the drift region (V_D). Since V_D in case of p^+nn^+ diode is largest (50.8 V) for ⟨111⟩ orientation (Table 1), highest output power should be obtained from the same device. $E(x)$ profiles for different orientations are very close to one another and the breakdown voltages given by $\int E\,dx$ across the whole of depletion layer are nearly the same. The extension of avalanche zone (x_A) as defined earlier depends on oreintation since the spatial variation of carrier currents in the depletion layer for a given structure is different for different orientations as observed from $|J_n - J_n|/J_0$ profiles (Figs 1-3). Thus $V_D = \int_{x_A}^{W} E\,dx$ is different for different orientations although $E(x)$ profiles are very close to one another. For the complementary n^+pp^+ diode with $N_A = 10^{22}/m^3$, x_A/W for ⟨110⟩ orientation is 37.2%, while the same for ⟨100⟩ and ⟨111⟩ are 38.4% and 38.0% respectively. The variations of the values of x_A/W, V_D and η with orientation are small for this device (Table 1 and Fig. 4). For DDR n^+npp^+ diode

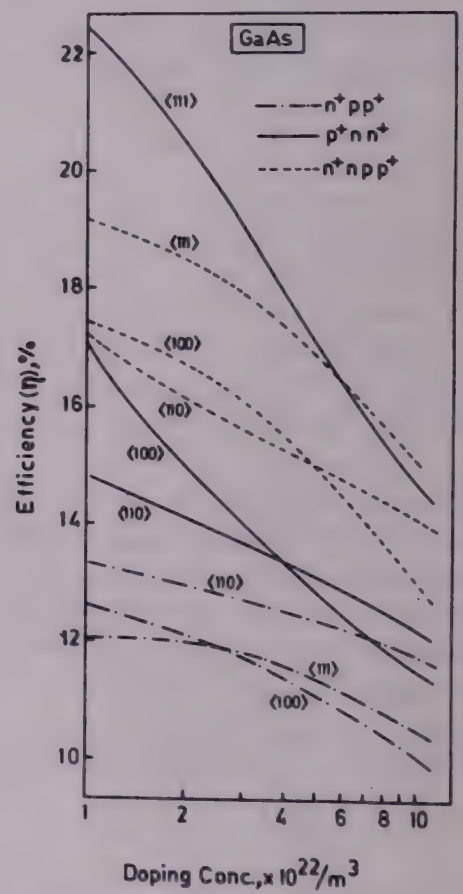

Fig. 4—Plot of efficiency versus doping concentrations of SDR and DDR diodes for different orientations

($N_A = N_D = 10^{22}/m^3$) x_A/W is 26.7% for ⟨111⟩ and 34% and 30.6% for ⟨110⟩ and ⟨100⟩ respectively. Thus amongst different orientations, ⟨111⟩ should be preferred for SDR p^+nn^+ as well as for DDR nn^+pp^+ diodes for realization of low x_A and large V_D, leading to higher η and rf power output.

4 Discussion

The highly localized avalanche zone for p^+nn^+ ⟨111⟩ oriented GaAs IMPATTS and consequent better

Table 1 - Calculated Values of Characteristic Parameters of SDR and DDR GaAs Impatt Diodes for Different Orientations and for Three Values of Background Doping Concentration

Structure		SDR n^+pp^+				SDR p^+nn^+				DDR n^+npp^+			
$\lvert N_D - N_A \rvert$ $10^{22}m^{-3}$	Orientation	E_m $10^7 V m^{-1}$	x_{AW} %	V_B V	V_D V	E_m $10^7 V m^{-1}$	x_{AW} %	V_B V	V_D V	E_m $10^7 V m^{-1}$	x_{AW} %	V_B V	V_D V
1.0	⟨100⟩	4.33	38.4	66.5	26.4	4.39	28.1	69.9	37.9	4.03	30.6	104.6	57.3
	⟨110⟩	4.38	37.2	68.6	28.7	4.44	34.0	71.3	33.3	4.09	34.0	107.0	53.8
	⟨111⟩	4.31	38.0	66.5	26.8	4.47	18.1	73.0	50.8	4.15	26.7	109.6	66.3
3.5	⟨100⟩	5.25	42.1	27.6	10.0	5.25	35.0	27.6	12.0	4.72	31.7	44.7	21.8
	⟨110⟩	5.15	39.0	26.5	10.3	5.24	37.0	27.6	11.3	4.75	32.2	45.4	22.0
	⟨111⟩	5.02	39.3	25.2	9.3	5.14	25.0	26.6	15.3	4.67	27.7	43.9	24.6
6.0	⟨100⟩	5.78	45.9	19.4	6.5	5.73	39.6	19.0	7.5	5.14	32.5	31.0	14.1
	⟨110⟩	5.56	41.0	18.0	6.9	5.64	40.1	18.5	7.5	5.11	31.9	30.7	14.1
	⟨111⟩	5.59	44.9	18.2	6.4	5.53	30.3	17.8	9.1	5.00	28.7	29.4	15.4

performance as regards d.c. to microwave conversion efficiency can be understood by noting that the hole ionization rate (α_p) is highest for ⟨111⟩ compared to that for ⟨110⟩ and ⟨100⟩ and is considerably larger than α_n for ⟨111⟩. From the maximum field point in the depletion layer of p^+nn^+ diode (located at the p^+n junction) up to the avalanche centre ($J_p = J_n$) situated in the n region, the density of holes is higher than that of electrons. Thus the intensity of multiplication in the higher-field region of avalanche zone in SDR (from field maximum to avalanche centre) is considerably enhanced when the p^+nn^+ devices are oriented along ⟨111⟩ which causes a reduction of x_A. The relative width of the avalanche zone (x_A/W) for ⟨111⟩ p^+nn^+ device is therefore narrowest (Fig. 1) compared to the same for other orientations which, in turn, should lead to highest η for such devices (Fig. 4).

It is seen from Fig. 4 that the efficiency of p^+nn^+ diode is higher for ⟨100⟩ compared to ⟨110⟩ at lower doping concentration ($\sim 10^{22} m^{-3}$) while the reverse is the case for higher doping levels ($\sim 10^{23} m^{-3}$). This can be explained in the following manner. It has already been noted that holes are the dominant carriers between field maximum and avalanche centre for p^+nn^+ diodes. It is further noted from the ionization rate expressions that α_p for ⟨100⟩ is considerably larger than α_n at lower field range ($\simeq 3 \times 10^7 V m^{-1}$ to $4 \times 10^7 V m^{-1}$) corresponding to the avalanche layer field for lower doping concentration ($\sim 10^{22} m^{-3}$), whereas for the same field range $\alpha_p \simeq \alpha_n$ for ⟨110⟩. Also, for this field range the magnitude of α_p for ⟨100⟩ is larger than that for ⟨110⟩. The inequality of ionization rates[9] and larger value for α_p in case of ⟨100⟩ causes thinner avalanche layer (x_A/W) which leads to higher efficiency. At higher field range ($\simeq 5 \times 10^7 V m^{-1}$ to $6 \times 10^7 V m^{-1}$), corresponding to avalanche field at higher doping concentration ($\sim 10^{23} m^{-3}$), α_p for ⟨110⟩ is slightly larger than that for ⟨100⟩. The ionization rates of two carriers are almost equal in higher field range for both the orientation unlike in the lower field range. These factors lead to slightly wider and larger x_A and lower η for ⟨100⟩ compared to ⟨110⟩ at higher doping levels.

In case of n^+pp^+ GaAs SDRs, the ionization rate of the predominant carrier (electrons) between the field maximum and the avalanche centre (Fig. 2) is only slightly different for different orientations with ⟨110⟩ having a slight edge over ⟨100⟩ and ⟨111⟩. Thus ⟨110⟩ oriented n^+pp^+ diode would give slightly narrower x_A (Fig. 2) and higher η than the same device with other orientations.

In the case of n^+npp^+ DDR diodes, the avalanche centre is very close to the maximum field point and is situated almost at the metallurgical junction and electrons predominate on the n side and holes on the p side of the avalanche zone. Thus the high-field region of DDRs do not have a clear predominance of either type of carriers and the properties are intermediate between p^+nn^+ and n^+pp^+. The net effect gives narrower x_A and higher η for ⟨111⟩ oriented DDR devices (Fig. 3) than those differently oriented. It is interesting to see from Fig. 4 and Table 1 that ⟨111⟩ oriented SDR p^+nn^+ devices made of GaAs are having lower x_A and higher η than similarly-oriented DDR devices up to a doping density of $6 \times 10^{22}/m^3$. For X-band (doping density $\sim 10^{22}/m^3$), ⟨111⟩p^+nn^+ SDR should give much better performance (as regards x_A and η) than corresponding DDR devices.

Acknowledgement

The authors wish to acknowledge the support for the research project on IMPATTs received from the University Grants Commission, New Delhi. Two of them (SPP and JPB) are also grateful to the UGC for

the award of teacher-fellowships. Thanks are also due for the cooperation received from the staff of the Computer Centre, University of Calcutta.

References

1 Stillman G E, Wolfe C M, Rossi J A & Foyt A G, *Appl Phys Lett* (*USA*), **24** (1974) 471.

2 Ito M, Kagawa S, Kanoda T & Yamaoka T, *J Appl Phys* (*USA*), **49** (1978) 4607.

3 Pearsall T P, Capasso F, Nahory R E, *et al.*, *Solid State Electron* (*USA*), **21** (1978) 297.

4 Lee M H & Sze S M, *Solid State Electron* (*USA*), **23** (1980) 1007.

5 Roy S K, Sridharan M, Ghosh R & Pal B B, *Proc* NASECODE-I *Conf. on Numerical Analysis of Semiconductor Devices*, (Boole Press, Dublin, Ireland) 1979, 266.

6 Kramer B & Mircea A, *Appl Phys Lett* (*USA*), **26** (1975) 623.

7 Dalal V L, Dreeban A B & Triano A, *J Appl Phys* (*USA*), **42** (1971) 2864.

8 Bauhahn P & Haddad G I, *IEEE Trans Electron Devices* (*USA*), **ED-24** (1977) 634.

9 Gibbons G, *Avalanche diode microwave oscillators* (Oxford University Press, Oxford) 1973, 68.

Indian Journal of Pure & Applied Physics
Vol. 21, October 1983, pp. 563-568

Analysis of the Absorption Spectra of CdS Thin Films Using Annealing Technique

K K DEY & U K CHATURVEDI
Department of Physics, Banaras Hindu University, Varanasi 221 005
and
A K CHATTERJEE
Physics Section, Harish Chandra Degree College, Varanasi 221 001

Received 24 *August* 1982; *revised received* 10 *January* 1983

The absorption spectra of CdS thin films ($\simeq 0.1\ \mu$m thick), grown under identical conditions, show low intensity peaks (which are interference effects superimposed on the absorption spectra) with absorption less than 10% of the value at the absorption edge. The wavelength range used is 7500-3500 Å, since the intensity of the peaks in this region is large enough for analysis. After the first annealing run at 100°C, the fundamental absorption edge remains fixed but the spectral trace lying on the longer wavelength side of the absorption edge gradually drifts towards the edge as the annealing temperature is increased. A theoretical model is proposed, using a lattice of trap levels located at the grain boundaries within the films, to explain the experimental results.

1 Introduction

The optical absorption spectra of CdS thin films have been investigated by a number of workers in order to evaluate trap level energies existing in the films. Cook[1] has shown that the spectral structure of CdS films differs markedly from that of single crystals and depends on the substrate temperature during deposition. Deep level trap defects in polycrystalline CdS junctions have been determined by Besomi and Wessels[2]. Bujatti and Marcelja[3] have reported that the absorption edge of CdS films is independent of temperature. Recently, Salkov *et al.*[4] have shown that in plastically deformed CdS crystals, the absorption peaks shift to shorter wavelengths with decrease in temperature from 140 to 4.2K in the region of transparency. It is expected that the effect of annealing in air is likely to affect the absorption characteristics of thin films. We have therefore studied the effect of annealing temperature on the absorption spectra of CdS thin films.

In the present paper, the effect of annealing on the optical absorption of CdS thin films grown under identical conditions is reported. In this study, the films were annealed in air successively at 100, 150 and 250°C, and the absorption spectra were taken at room temperature after each annealing run. It is well known that no significant chemical change occurs in CdS films in the course of the process of annealing up to a temperature of 250°C, the maximum oxidation being less than 0.1% at 300°C (Ref. 5). After the first annealing at 100°C, with increasing annealing temperature, the fundamental absorption edge remains fixed, but the absorption trace lying on the longer wavelength side of the absorption edge along with interference peaks drifts towards shorter wavelengths. The results have been explained with the help of a theoretical model, in which the film matrix has been taken in the form of a chain of crystallites, with a fixed angle between neighbouring crystallites. However, the theory fails to explain the shift of peaks to longer wavelengths, when the temperature is taken from 30 to 100°C.

2 Theoretical Analysis

2.1 Film as a Lattice

A thin film may be considered to be made up of a number of crystallites grown on a substrate with or without any specific orientation. In the present work, a thin film of CdS has been deposited on a mica sheet on the usual (001) cleavage plane. The film matrix may be considered to be made up of a large number of crystallites arranged in parallel rows, each crystallite making an angle θ with its neighbour and separated from it by a grain boundary (Fig. 1). This is similar to the model used by Deptuch *et al.*[6].

The inclined arrows give crystallite orientation and the vertical arrows give substrate orientation. The difference between the crystallite and substrate orientations can be explained quite easily. From the basic ideas of epitaxial growth from vacuum evaporated material on crystalline substrates, it has been established that the epitaxial growth continues up to about 100 Å ($\simeq 0.01\ \mu$m). Beyond this the orientation changes and so the second layer will have crystallites, whose orientation makes a small angle with that of the substrate. The deviation will increase as one goes from the substrate upwards. This means that

the angle θ between the neighbouring crystallites will decrease from one layer to the next above it (Fig. 1).

Consider a single value of θ for a given layer of crystallites. Such a layer will look like a zigzag chain of crystallites, when viewed along the film width (Fig. 1). In Fig. 2, d denotes the apparent crystallite size as viewed under the microscope, and it is measured up to the centre of the grain boundary. The geometry of Fig. 2 gives the actual crystallite size l as,

$$l = d \text{ cosec } (\theta/2) \quad \ldots (1)$$

The junction between the crystallites is the region where the grain boundary exists. The grain boundary is the region where, due to lattice mismatch, a density of unsaturated bonds exists. This charge density is primarily responsible for the occurrence of a trap level at the grain boundary. The trap level energy should depend upon θ and the crystallite orientation.

Hence we may consider a grain boundary with a given θ to give rise to a trap level having energy lying between the band gap of the material. Such a consideration is in accordance with the Shockley-Read theory of recombination. A large number of trap level energies may be expected for values of θ ranging from 0 to π.

Consider the structure of a single layer of crystallite as shown in Fig. 2, with a crystallite size equal to l and a trap level at each grain boundary. From this we may develop a one-dimensional lattice as shown in Fig. 3, with l as the lattice parameter. The Vs in Fig. 3 mark lattice points where the grain boundaries are located. These are the sites where a conduction electron has to overcome a certain potential, in order to move further into the lattice. The case becomes analogous to the tight binding approximation in real lattice, the basic difference is that the total wavefunction need not be written down as a summation, as the crystallite size l is large enough to prevent any overlap of the wavefunctions located at the Vs.

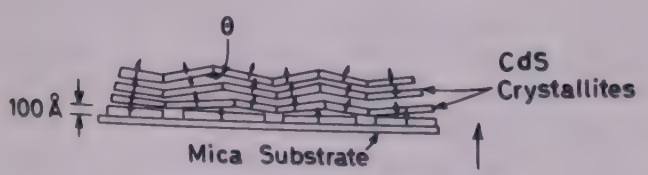

Fig. 1—CdS film on mica substrate

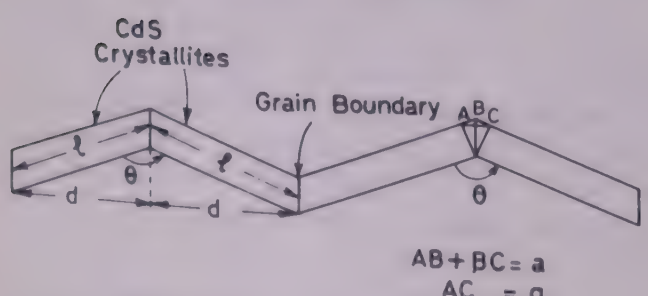

Fig. 2—Proposed CdS crystallite chain

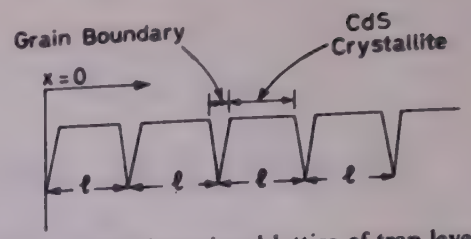

Fig. 3—One-dimensional lattice of trap levels

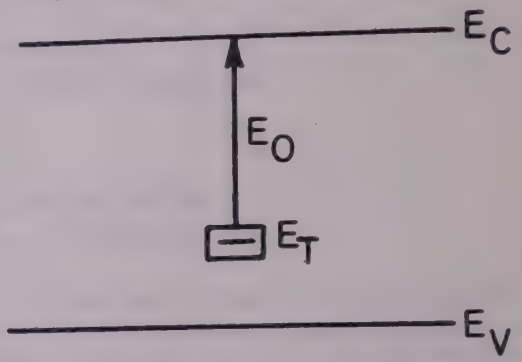

Fig. 4—Trap level E_T located in the band gap

Referring to Eq. 1, we note that the effective part of d is merely equal to the apparent grain boundary thickness g, since we need to consider only the effect of traps located at the grain boundaries. The lattice of Fig. 3 will then include only the Vs. The effective lattice parameter a which is equal to the actual grain boundary thickness can be calculated by considering a pair of neighbouring crystallites. Using Fig. 2, with g = AC, a can be written as

$$a = g \text{ cosec } (\theta/2) \quad \ldots (2)$$

However, it is to be remembered that in between two grain boundaries the electronic energy is equal to E_C, the energy of the conduction band edge, whereas the tip of the Vs denotes an energy equal to the trap level energy in a single chain of crystallites.

Fig. 4 shows a trap level with energy E_T filled with an electron at room temperature. It requires an energy equal to E_0 to reach the conduction band. Hence to cross the trap, a conduction electron within a crystallite must have an energy equal to E_C, i.e. 2.42 eV in CdS plus the trap level energy E_0. This is because a conduction electron with energy E_C faces a potential barrier of height E_0 in the vicinity of the trap at the grain boundary. Hence for a mobile electron in this lattice, we may write for its energy E as

$$E = E_C - E_0 \exp(ikx) \quad \ldots (3)$$

where the minus sign implies that the trap level decreases the energy of a conduction electron, k denotes the propagation constant, and x the distance along the lattice. The complex value of E in Eq. 3 includes the phase factor. For $x = a$, E is maximum for $k = \pm\pi/a$, and minimum for $k = 0$.

The effective electronic mass (m^*) is given by

$$m^* = -\frac{\hbar^2}{(\partial^2 E/\partial k^2)}$$

Using Eq. 3,

$$m^* = -\left(\frac{\hbar^2}{E_0 x^2 \exp[ikx]}\right)$$

We need to maximize the value of E in Eq. 3 as we are dealing with mobile electrons.

For $x = a = g\,\mathrm{cosec}(\theta/2)$, $k = (\pi/a)$ and setting $\theta = \pi$, we get

$$m^* = +\left(\frac{\hbar^2}{E_0 g^2}\right) \qquad \ldots (4)$$

with $E = E_C + E_0$. Now substituting one of our observed values of E_0 as $E_0 \simeq 2$ eV, and g being of the order of 10 Å (Ref. 7), the value of m^* turns out to be $+3.46 \times 10^{-29}$ g, as against 3.18×10^{-28} g in CdS crystals (Ref. 8). This is, of course, an extreme case. For values of $k \leq (\pi/a)$, m^* is positive and still remains of the order of 10^{-29} g.

This decrease in m^* with a corresponding increase in energy can be interpreted as due to the Coulomb attraction between a mobile electron and fixed positive charges at the grain boundary which are likely to be doubly ionized cadmium atoms (Cd^{2+}). The consequent increase of energy is sufficient to carry it over the trap at the grain boundary and into the next crystallite.

2.2 Calculation of Energy

To evaluate the electronic energy in the lattice, we introduce a pseudo-atomic wavefunction $\psi(x)$, given by

$$\psi(x) = \psi_0 e^{ikx} \qquad \ldots (5)$$

where ψ_0 corresponds to the trap level energy E_0, having a maximum at $x = a, 2a, \ldots$ and falls off as one goes away from the grain boundary.

Let us now consider ψ between adjacent crystallites having a common grain boundary and a given θ, as this is sufficient to study the possible electronic energies within the film.

The Schrödinger equation then reads

$$H\psi = E\psi \qquad \ldots (6)$$

$$\text{with} \quad E = \frac{\int_v \psi^* H \psi\, dv}{\int_v \psi^* \psi\, dv} \qquad \ldots (7)$$

where the integrals extend over the volume occupied by the two crystallites. The denominator is obviously equal to one.

We define H, as usual, by

$$H = \left[-\frac{\hbar^2}{2m^*}\nabla^2 + V(x)\right] \qquad \ldots (8)$$

where $V(x)$ is the potential energy. Using Eq. 5, we may write Eq. 7 as

$$E = \int_v \psi_0^* e^{-ikx}\left[-\frac{\hbar^2}{2m^*}\nabla^2 + V(x)\right]\psi_0 e^{ikx}\, dv \qquad \ldots (9)$$

A little simplification leads to

$$E = \left(\frac{\hbar^2 k^2}{2m^*}\right) + \int_v \psi_0^* V(x)\psi_0\, dv \qquad \ldots (10)$$

This is the energy expression as given in Eq. 2.

If the system is at a temperature T, we may write E^T instead of E in Eq. 10 and equate with Eq. 2. Thus

$$E^T = \left(\frac{\hbar^2 k^2}{2m^*}\right) + \int_v \psi_0^* V(x)\psi_0\, dv = E_C - E_0 e^{ikx} \qquad \ldots (11)$$

At the pseudo-lattice point, $x = a$, $k = \pi/a$ and $V(x) = E_0$. Eq. 11 then gives

$$E^T_{x=a} = \left(\frac{\hbar^2 k^2}{2m^*}\right)_{x=a} + \left[E_0 \int_v \psi_0^* \psi_0\, dv\right]_{x=a} = E_C + E_0 \qquad \ldots (12)$$

The integral now expresses the probability of finding the electron in the vicinity of $x = a$.

For a mobile electron in the conduction band, the probablity of finding it at $x = a$ is very small. The value of the integral in Eq. 12 is quite small and hence the second term in third bracket in Eq. 12 can be neglected. This gives

$$E^T_{x=a} = \left(\frac{\hbar^2 k^2}{2m^*}\right)_{x=a} = E_C + E_0 \qquad \ldots (13)$$

If the film is annealed at a higher temperature, say $(T + \Delta T)$, the crystallite chain of Fig. 2 will tend to adjust itself to a state of lower potential energy. This will cause θ to increase to θ'. The new lattice constant a' will be given by

$$a' = g'\,\mathrm{cosec}\,(\theta'/2) \qquad \ldots (14)$$

The associated wavefunction now becomes

$$\psi'(x) = \psi_0' e^{ik'x} \qquad \ldots (15)$$

where ψ_0' corresponds to the new trap level energy E_0', and k' is the new value of k.

The Schrödinger equation becomes,

$$H'\psi' = E'\psi' \qquad \ldots (16)$$

where

$$H' = \left[-\frac{\hbar^2}{2m'^*}\nabla^2 + V'(x)\right] \qquad \ldots (17)$$

m'^*, $V'(x)$ and E' are the new values of m^*, $V(x)$ and E respectively. If E_0' is the new value of E_0, then solving as in Eq. 9 above, we may write

$$E' = E^{T+\Delta T} = \left(\frac{\hbar^2 k'^2}{2m'^*}\right) + \int_v \psi_0'^* V'(x)\psi_0'\, dv = E_C - E_0' e^{ik'x} \qquad \ldots (18)$$

At $x = a'$, $k' = \pi/a'$, $V'(x) = E_0'$,

$$E^{T+\Delta T}_{x=a} = \left(\frac{\hbar^2 k'^2}{2m'^*}\right)_{x=a'} + \left[E_0' \int_v \psi_0'^* \psi_0'\, dv\right]_{x=a'} = E_C + E_0' \qquad \ldots (19)$$

Neglecting the second term in third bracket in Eq. 19 as has been done in Eq. 12, we obtain

$$E_{x=a'}^{T+\Delta T} = \left(\frac{\hbar^2 k'^2}{2m'^*}\right)_{x=a'} = E_C + E_0' \qquad \ldots (20)$$

The change in trap level energy $\Delta E (= E_0' - E_0)$ can be calculated from Eq. 13 and Eq. 20. Thus

$$\Delta E = E_0' - E_0 = \left(\frac{\hbar^2 k'^2}{2m'^*}\right)_{x=a'} - \left(\frac{\hbar^2 k^2}{2m^*}\right)_{x=a} \qquad \ldots (21)$$

Using Eqs. 2 and 14 and noting that at $x = a$, $k = \pi/a$ and at $x = a'$, $k' = \pi/a'$, we have

$$\Delta E = \frac{\hbar^2}{8}\left[\frac{\sin^2(\theta'/2)}{m'^* g'^2} - \frac{\sin^2(\theta/2)}{m^* g^2}\right] \qquad \ldots (22)$$

Since change in g and m^* is not appreciable, we may write $g \simeq g'$ and $m^* \simeq m'^*$. This gives

$$\Delta E = \frac{\hbar^2}{8m^* g^2}[\sin^2(\theta'/2) - \sin^2(\theta/2)] \qquad \ldots (23)$$

Hence with the increase of annealing temperature, θ' will increase and so $[\sin^2(\theta'/2) - \sin^2(\theta/2)]$ will also increase. Since ΔE is positive, the trap level energy will increase. This means that the absorption spectra will shift towards shorter wavelengths with increasing annealing temperature.

3 Experimental Details

Three mica substrates (dimension, $1 \times 3 \times 0.01$ cm) were cut from the same mica sheet, so that their thickness and orientation remained the same. They were washed with nitric acid, rinsed in sodium hydroxide solution and then washed in trichloroethylene. They were then washed with distilled water and cleaned ultrasonically.

Two of the substrates were fixed inside the vacuum evaporation unit, while the third was preserved to act as a reference in the absorption spectrophotometer.

The CdS powder used was 99.999% pure, manufactured by Koch-Light Laboratories, UK. The powder was pressed in a die (diam., 2.54 cm), using a pressure of 10 tons for 5 min to form a 2 mm thick pellet of CdS. A portion of the pellet was placed on a tungsten filament in a coating unit. The temperature of the substrate was maintained at 350°C to give a good crystallinity. The deposition rate was 100 Å/min and the film thickness measured by a quartz oscillator was 0.1 μm. Pressure during the deposition was maintained around 10^{-5} Torr. By using X-ray technique in a Debye-Scherrer camera, using a fixed beam to film plane angle of 25°, the estimated particle size was about 0.1 μm in Film 1 and 0.5 μm in Film 2.

The absorption traces of the two films (Figs. 5 and 6) were recorded in the wavelength range 7500-3500 Å with a Beckman Spectrophotometer (Model 5240) using the clean mica substrate for reference.

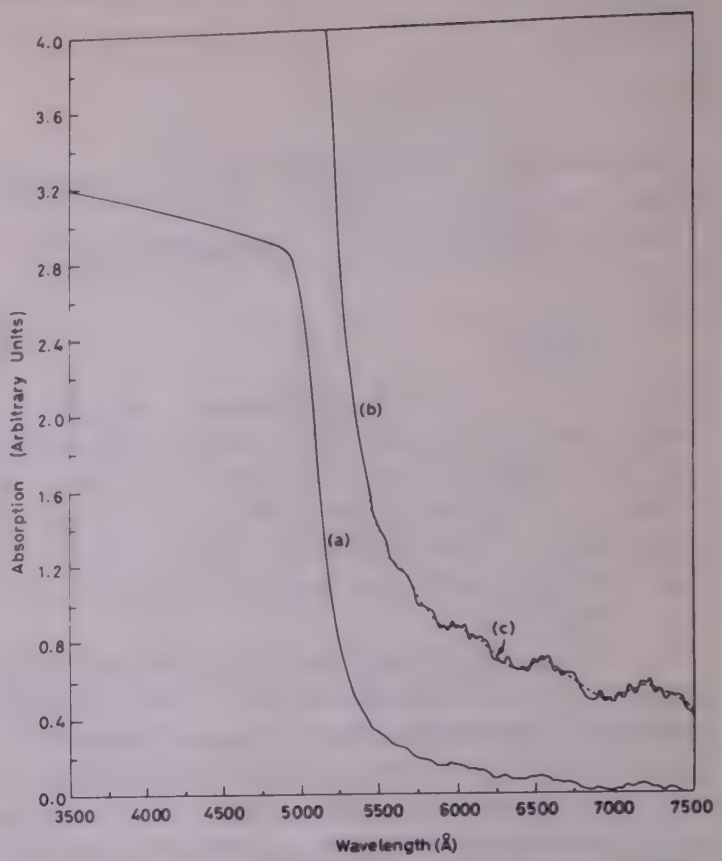

Fig. 5—Absorption spectra of Film 1 at room temperature (30°C) [(a), low resolution; (b), high resolution; and (c), average]

Both the films have maximum absorption around 5000 Å, i.e., 5500 Å for Film 1 and 5300 Å for film 2, obtained by evaluating the wavelength for the maximum slope of the edge in the two cases. At low resolution of the spectrophotometer, the low intensity peaks lying on the longer wavelength side of the absorption edge (trace a, Figs 5 and 6) cannot be seen clearly. However, at high resolution, they appear quite distinctly (trace b, Figs 5 and 6). An interesting feature is the large number of peaks which appear in the trace b of Fig. 5 (Film 1), as against trace b of Fig. 6 (Film 2). We have drawn the average trace given by the dashed line c (by the average area method) in Fig. 5 and it agrees well with the trace of Film 2 of Fig. 6. The room temperature was 30°C and the wavelengths corresponding to the three peak positions were noted.

The temperature of the films exposed to air was raised to 100°C, as also the reference substrate, at the rate of 10°C/min and maintained at the same temperature for 30 min, after which they were cooled to the room temperature at a slower rate of 5°C/min. The absorption spectra of the two films were again taken. It may be mentioned that the use of the reference mica sheet during all operations as also in the spectrophotometer ensures that the effects of CdS film alone are obtained in the spectral trace. The annealing treatment was similarly done at 150 and 250°C and the absorption trace was obtained after each annealing run. The wavelengths corresponding to the peak positions were obtained.

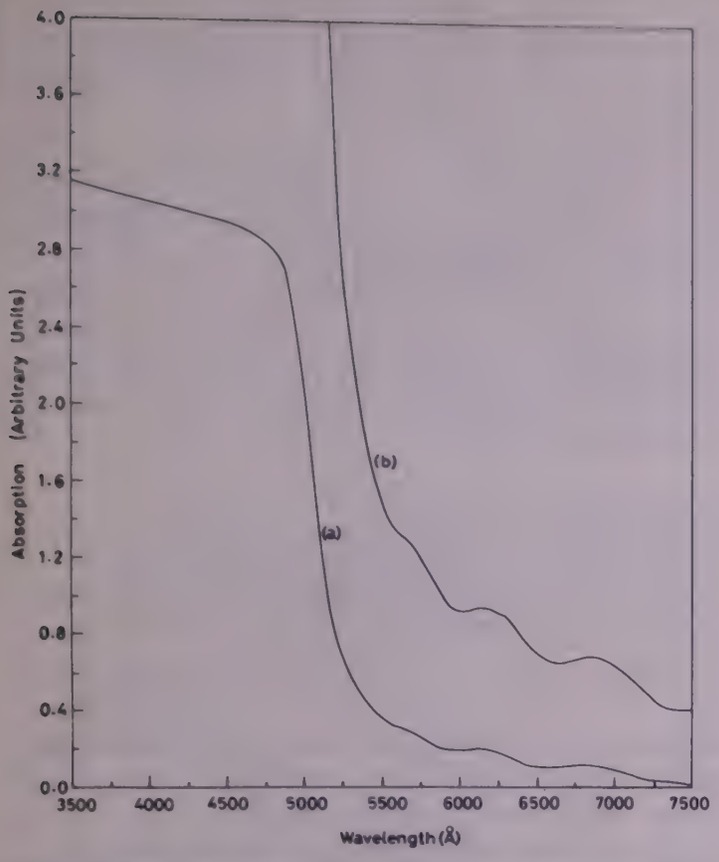

Fig. 6—Absorption spectra of Film 2 at room temperature (30°C) [(a), low resolution; and (b), high resolution]

Table 1—Wavelength Shift ($v\lambda$) and Energy Shift (ΔE) with Increasing Annealing Temperature (T_A)

Peak No.	Wavelength, Å				$\Delta\lambda$ Å	ΔE† eV
	*30°C	**T_A =100°C	T_A =150°C	T_A =250°C		
			(Film No. 1)			
1	7200	7250	7200	7150	−100	0.020
2	6550	6600	6580	6520	−80	0.030
3	6000	6100	6090	6050	−50	0.017
			(Film No. 2)			
1	6870	6780	6750	6650	−130	0.040
2	6150	6100	6100	6040	−60	0.018
3	5620	5600	5580	5570	−30	0.016

*Before annealing; **As annealing begins
†Conversion formmula: $\lambda(\mu m) = 1.24/E$ (eV)
Note: $\Delta\lambda$ and ΔE values are w.r.t. 100°C

After the first annealing run at 100°C, the peaks in Film 1 drifted towards longer wavelengths and those in Film 2 towards shofter wavelengths. Since the two traces were taken simultaneously, no experimental error is possible. However, after the first annealing at 100°C, further annealing at 150 and 250°C gave unidirectional drift of the peaks towards shorter wavelengths. Hence the drift of the peaks was measured with reference to the 100°C run. The results are presented in Table 1.

The drifts of the peaks as obtained from the absorption spectra of the films are summarized in

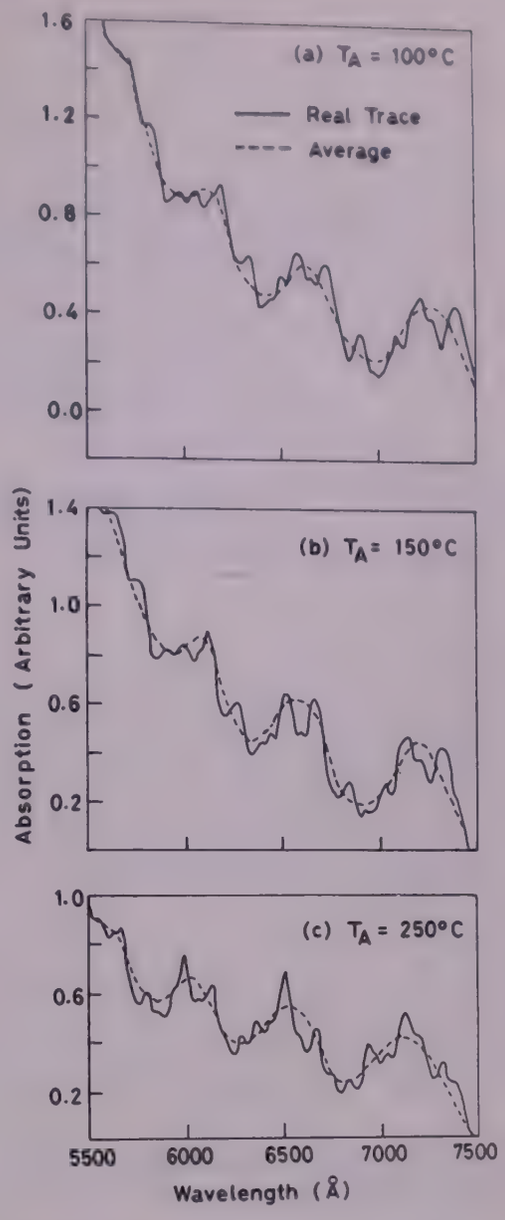

Fig. 7—Positions and intensities of the peaks for Film 1 for three different annealing temperatures

Figs 7 (Film 1) and 8 (Film 2); only the relevant portions of the absorption spectra are presented.

4 Discussion

The absorption spectra of the films as shown in Figs 7 and 8 do indicate that the two films are not structurally identical. In fact, the particle or crystallite size is 0.1 μm in Film 1 as against 0.5 μm in Film 2. Film 1 obviously has greater number of grain boundaries. which act as light scattering centres, giving rise to a large number of low intensity peaks in its absorption trace. Film 2, however, appears to be structurally more stable. This is evident from the fact that in this film the drift of the peak with increasing T_A remains unidirectional, i.e. towards shorter wavelengths. Film 1 gives a similar drift, but only after the first annealing run at 100°C. After the first annealing run, the two films give unidirectional drift of the peaks. However. scattering phenomena continue to give a large number

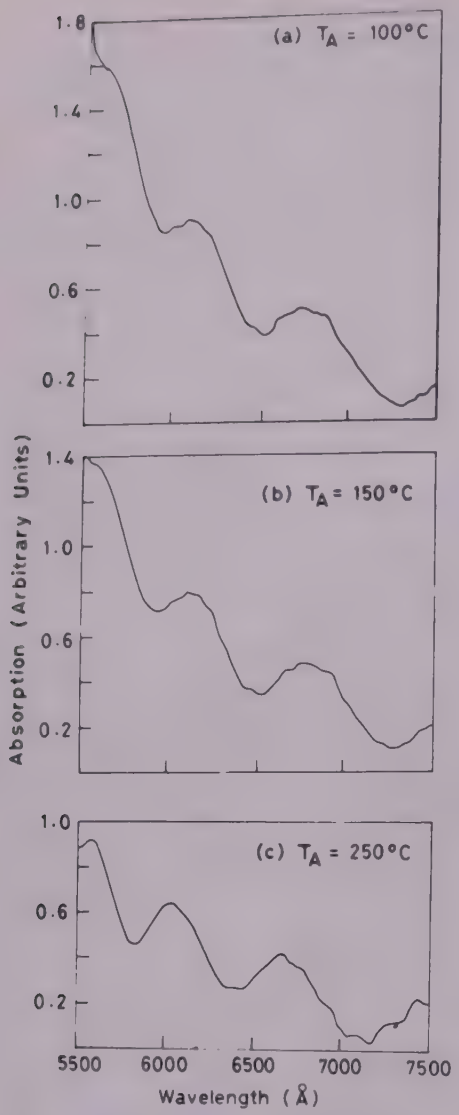

Fig. 8—Positions and intensities of the peaks for Film 2 for three different annealing temperatures

of peaks in the absorption trace of Film 1, even after being annealed at 250°C.

The traps located at grain boundaries are primarily doubly ionized cadmium atoms (Cd^{2+}), the density of Cd^{2+} atoms within the grain boundary increases as the crystallites tend to move towards a state of lower potential energy with increasing annealing temperature. This is because the grain boundary thickness decreases as the angle θ between the crystallites increases with increase in T_A. Such an increase in the density of Cd^{2+} atoms gives rise to a greater field intensity at the grain boundary. Hence the trap level energy increases with increasing annealing temperature. This is in agreement with the calculations based on the theoretical model and expressed in Eq. 23.

Since θ can have a large number of values ranging from 0 to π, the value of E_T, the trap level energy, can also have a large number of values between 0 and 2.42 eV. This is the reason for a uniform increase in absorption due to the films from the longer wavelength region to the absorption edge.

Using Eq. 23 and setting $\theta' = \pi$, $m^* = 3.46 \times 10^{-29}$ g, $g = 10$ Å, $\Delta E = 0.02$ eV for 100°C to 250°C annealing temperature change, θ comes out as 127°. This means that in the crystallites just above the substrate, the angle between the crystallites may be expected to change by 53° over this range of annealing temperature. It appears, therefore, that the proposed theoretical model can explain reasonably well the experimental results.

5 Conculsion

The unidirectional drift of the peak positions and the absorption spectra of CdS thin films lying on the longer wavelength side of the absorption edge after the first annealing run at 100°C, as also the decrease in the intensity of the peaks, lead us to conclude that, to obtain greater structural stability, it is always better to anneal CdS thin films to a sequence of successively increasing annealing temperatures.

The variation of particle size in the two films grown under identical conditions and the gradual decrease in absorption associated with the peaks as T_A is increased (as shown in Figs. 7 and 8) are yet to be investigated. It would be interesting to analyze the relative intensities of the peaks and the nature of variation of the angle θ between the crystallites with T_A. Lastly, we need only mention that we have kept our work limited up to 250°C. This is because annealing at higher temperatures should be done in vacuum as CdS gets oxidized in air rapidly beyond 300°C. Further work on these problems is in progress.

Acknowledgement

The authors are indebted to Prof. Suresh Chandra for his helpful discussions during the course of this investigation.

References

1 Cook R K, *J Appl Phys (USA)*, **51** (1980) 668.
2 Besomi P & Wessels B, *J Appl Phys (USA)*, **51** (1980) 4305.
3 Bujatti M & Marcelja F, *Thin Solid Films (Switzerland)*, **11** (1972) 249.
4 Salkov E A, Tarabaev N I & Shepelskii G A, *Ukr Fiz Zh (USSR)*, **24** (1979) 1908.
5 Chizhikov D M, *Cadmium*, Translated in English by D E Hayler (Pergamon, London) 1966, p. 27, Table 22.
6 Deptuch A, Grus M, Horodecki A J & Lepek M, *Phys Status Solidi a (Germany)*, **37** (1976) k101.
7 Hill R M, *Nature (GB)*, **204** (1964) 35.
8 Bube R H, *Photoconductivity of Solids* (John Wiley, New York), 1967, p. 209, Table 7.2-1.

Indian Journal of Pure & Applied Physics
Vol. 21, October 1983, pp. 569-572

Rotational Barrier Height and Off-center of Mass Displacement for Hydroxyl Ion in Alkali Halide Crystal Matrices

LALAN JHA & HARE KRISHNA JHA
University Department of Physics, L N Mithila University, Darbhanga 846004

Received 8 *February* 1983

Rotational barrier height and off-center of mass displacement parameter for hydroxyl ion in alkali halide matrices have been calculated on the basis of the model developed by G K Pandey and D K Shukla [*Phys Rev B (USA)*, 3 (1971); 4 (1971) 4598], and including all the possible interaction terms. The calculated barrier parameters give a good understanding of the librational and tunnelling frequency of the impurity in the matrix.

1 Introduction

Diatomic impurities like OH^- in alkali halide matrices have attracted considerable attention during the last two decades[1]. The angular motion of the impurity in the matrix cavity is of particular interest as it causes pronounced changes in the dielectric constant, specific heat, thermal conductivity, etc. of the system at low temperatures. The interpretation of these and other related observations, e.g. infrared absorption and para-electric resonance, requires a definite knowledge of the potential barrier hindering angular motion of the impurity in the matrix cavity. The other thing of importance in this connection is the possible off-center of mass displacement parameter of the impurity in the matrix. There are strong evidences[2-4] that in certain crystals, the OH^- impurity enters substitutionally, but its center of mass is slightly displaced from the normal lattice position. Under such circumstances, the point of the impurity which rests at the normal lattice site is known as center of interaction (CI) and the separation between the CI and the center of mass (CM) is known as the off-center of mass displacement parameter. It is also believed that the anisotropy of angular interaction is minimum about the CI, and hence the impurity when left to itself performs angular motion about the CI in the matrix cavity. The effective moment of inertia and hence the rotational constant of the impurity is thus changed, which shows its effect on the observed infrared spectra and other bulk properties of the crystal.

An idea of the potential barrier hindering angular motion also throws important light on the nature of the rotational motion of the impurity. For example, if the potential barrier is low, the molecule can be treated as performing almost free rotation or at the best, slightly hindered rotation. However, if the potential barrier is high, the molecule is mostly confined in certain minimum energy orientational configurations and performs only librational motion about the mean equilibrium orientation. This changes the nature of the infrared spectra and other bulk properties of the system. Also, while performing librational motion in individual potential wells, the molecule can make quantum mechanical tunnelling between the equivalent wells. This causes splitting of the torsional oscillator levels. This shows its effect on the low-temperature specific heat (the well known Schottky anomaly), thermal conductivity and dielectric properties of the system. The well known paraelectric resonance is also obtained due to the tunnelling phenomenon.

A clear understanding of these motional states requires theoretical knowledge of the barrier-hindering angular motion and possible off-center of mass displacement parameter of the impurity in the matrix cavity.

Some attempts have been made for calculating theoretically these parameters for the OH^- impurity in alkali halide crystals. Lawless[5] used a point charge-point dipole model to calculate the rotational barriers. Chandra *et al.*[6] calculated the barrier height on a more realistic approach but did not consider the possibility of off-center of mass displacement of the impurity in an explicit way. The most successful attempt was made by Pandey and Shukla[7]. It used the general method of multipole expansion of intermolecular interaction and then summed it over all the vital lattice points. In this process, it was found that only those interactions which have a fourth-power dependence on the angular coordinates contribute to the barrier height. This is due to the octahedral symmetry of the crystal. Thus, Pandey and Shukla concluded that only the following interactions should contribute to the barrier height: (i) Charge-hexadecapole moment interaction (ii) Quadrupole-quadrupole induced dipole interaction, and (iii) Charge-hexadecapole moment induced dipole int-

eraction. From the work of Kielich[8], it could be demonstrated that even the dipole-octupole induced dipole interaction term has a fourth-power dependence on angular coordinates of the impurity. Hence, this should also contribute to the barrier height. Also, there is a small inadvertent error in the calculation of Ref. 7 in considering the contribution of the charge-hexadecapole induced dipole interaction term[9]. We, in the present work, have tried to recalculate the potential barrier-hindering angular motion and off-center of mass displacement parameter on the lines of Pandey and Shukla, but including all the possible interaction terms and also correcting the small mistake made in their work[9]. The final results have been discussed in the light of the recent trend of work in the field.

2 Potential Barrier and Off-center of Mass Displacement Parameter

The barrier arises due to the angular anisotropy of interaction between the trapped impurity and the atoms of the host lattice. The dominant interactions which have been considered and which contribute to the barrier height are the following:

(i) Electrostatic interaction between the charges of the host lattice atoms and the multiple moments of the impurity. Only the interaction between the hexadecapole moment of the impurity and the charges of the host lattice atoms contribute to the barrier height.

(ii) Polarization interaction, i.e. the interaction between the multipole moments of the impurity and the dipole moment induced in the host lattice atoms due to these multipole moments. In this, only the quadrupole-quadrupole induced dipole, hexadecapole moment-charge induced dipole and octupole moment-dipole induced dipole terms contribute to the barrier height. The explicit expressions for these are well known[8]. These can be rearranged and written in terms of spherical harmonics, summed over all the neighbouring and far-neighbouring atoms of the host crystal to give the barrier parameter as

$$K=\sum_{i=\text{Diff shells}}\rho_i\left[\frac{9\alpha_H\Theta_{S^2}}{2R_i^8}-\frac{7C_H\varphi_S}{2R_i^5}+\frac{35\alpha_H C_S\varphi_S}{4R_i^8}+5\frac{\alpha_H\mu_S\Omega_S}{R_i^8}\right]$$

or ...(1)

$$K=A\Theta_{S^2}+B\varphi_S+C\mu_S\Omega_S \qquad ...(2)$$

where

$$A=\sum_i\rho_i\left[\frac{9\alpha_H}{2R_i^8}\right] \qquad ...(3)$$

$$B=\sum_i\rho_i\left[-\frac{7C_H}{2R_i^5}+\frac{35\alpha_H C_S}{4R_i^8}\right] \qquad ...(4)$$

$$C=\sum_i\rho_i\left[5\frac{\alpha_H}{R_i^8}\right] \qquad ...(5)$$

The subscripts H and S denote respectively the host lattice and the solute or the impurity ion. The symbols C, μ, Θ, Ω and φ stand for the net charge, dipole, quadrupole, octupole and hexadecapole moments respectively. Here, ρ_i is a shell summation constant, R the lattice parameter, and R_i the distance of the impurity ion from any ion of the ith shell. The values of ρ_i, R_i/R are given in Table 1.

The molecular moments μ_S, Θ_S... etc. are those expressed about the CI (the point which rests at the normal lattice site). These can be expressed in terms of the impurity multipole moments expressed with respect to the CM and the (CM-Cl) separation, as follows:

$$\varphi_{S(CI)}=\varphi_{S(CM)}-4a\Omega_{S(CM)}+6a^2\Theta_{S(CM)}-4a^3\mu_{S(CM)}+a^4C_S$$

$$\Omega_{S(CI)}=\Omega_{S(CM)}-3a\Theta_{S(CM)}+3a^2\mu_{S(CM)}-a^3C_S$$

$$\Theta_{S(CI)}=\Theta_{S(CM)}-2a\mu_{S(CM)}+a^2C_S$$

$$\mu_{S(CI)}=\mu_{S(CM)}-aC_S$$

and

$$C_{S(CI)}=C_{S(CM)} \qquad ...(6)$$

Substitution of these relations in Eq. (2) gives,

$$K=[A\Theta_{S^2}+B\varphi_S+C\mu_S\Omega_S]-a[4A\Theta_S\mu_S+4B\Omega_S+C(C_S\Omega_S+3\mu_S\Theta_S)]+a^2[A(4\mu_{S^2}+2\Theta_SC_S)+6B\Theta_S+C(3C_S\Theta_S+3\mu_{S^2})]-a^3[2A\mu_SC_S+4B\mu_S+4C\mu_SC_S]+a^4[AC_{S^2}+BC_S+CC_{S^2}] \qquad ...(7)$$

The barrier parameter K is also a measure of the strength of the angular anisotropy of interaction. Hence, according to the definition of CI, dK/da should vanish and d^2K/da^2 should be positive. This gives,

$$a^3[AC_{S^2}+BS_S+CC_{S^2}]-3a^2[A\mu_SC_S)/2+B\mu_S+C\mu_SC_S]+a[A(2\mu_{S^2}+\Theta_SC_S)+3B\Theta_S+C\left(\frac{3}{2}C_S\Theta_S+\frac{3}{2}\mu_{S^2}\right)]-A\Theta_S\mu_S+B\Omega_S+\frac{C}{4}(C_S\Omega_S+3\mu_S\Theta_S)]=0 \qquad ...(8)$$

Table 1—Shell Summation Constants of Eq. (5)

Shell No.	Number of atoms in the shell	ρ_i	(R_i/R)
First	6	1.0	1
Second	12	−0.5	$\sqrt{2}$
Third	8	−0.88889	$\sqrt{3}$
Fourth	6	+1.0	2
Fifth	24	+0.8	$\sqrt{5}$
Sixth	24	−1.0	$\sqrt{6}$
Seventh	12	−0.5	$\sqrt{8}$
Eighth	30	−0.92593	3

The constants A, B and C depend only upon the matrix parameters. Eqs (7) and (8) in this way give the values of the barrier parameter and the off-center displacement of the impurity's CM respectively, in terms of the multipole moments of the impurity and the constants of the matrix.

3 Effect of Lattice Distortion Near the Impurity

In cases where the size and/or the charge distribution in the impurity is different from that of the substituted ion of the host lattice, a distortion of the lattice is always expected. It was concluded by Pandey and Shukla[10] that for the present systems, an isotropic lattice contraction takes place. The extent of lattice contraction[10] was calculated by using Brauer's method[11]. We have taken the lattice contractions as such and considered them in the calculation of the barrier height and the off-center displacement parameter.

4 Results and Discussion

Tables 2 and 3 give the various constants used in the calculations. Table 4 gives the percentage lattice contraction around the OH^- impurity, which was calculated using Brauer's method as reported in Ref. 10. Table 5 gives the calculated values of the barrier parameter K and the off-center of mass displacement parameter a for the five crystal matrices, viz. KCl, KBr, KI, NaCl and RbCl. We should now show that these calculated values of K and a are in accordance with some experimental results. The most convenient experimental observations which they could be related to are the librational frequency observed in the infrared and the tunnelling frequency observed in the paraelectric resonance experiments and low-temperature specific heat measurements. The fourth column of Table 5 gives the values of the librational frequencies obtained with the help of the K and a values of columns 2 and 3. Column 5 of Table 5 gives the experimental values. A comparison of columns 4 and 5 shows that our calculations give a nice explanation of the librational frequencies as well as their variation on isotopic substitution. Columns 6 and

Table 2—Lattice Parameters Used in the Calculations

Parameter	KCl	KBr	KI	NaCl	RbCl
R(Å) (Ref. 12)	3.12	3.25	3.53	2.80	3.26
α^+ (Å^3) (Ref. 13)	3.29	3.29	3.29	1.57	4.56
α^- (Å^3) (Ref. 13)	4.98	6.44	8.68	4.98	4.98

Table 3—Constants of Hydroxyl Ion Impurity Used in the Calculations

	OH^-	OD^-
Rotational constant		
B (in cm^{-1})	18.9	10.0
μ_S (Debye)	4.59	4.59
Θ_S (Debye Å)	0.424	0.424
Ω_S (Debye Å^2)	0.074	0.074
φ_S (Debye Å^3)	−1.57	−1.57
Bond length (Å)	0.974	0.974

Table 4—Percentage Lattice Contraction around the OH^- Impurity as Calculated in Ref. 10 and Used in Our Calculation

Crystal	Lattice contraction %
KCl	3.0
KBr	4.2
KI	8.2
NaCl	4.2
RbCl	2.0

Table 5—Calculated Values of K and a (From these, the values of Librational Frequency and Tunnelling Frequency have been Calculated and Compared with the Experimental Values)

System	Calculated barrier height (cm^{-1})	Displacement of impurity's CM (Å)	Librational frequency, cm^{-1}		Tunnelling frequency, cm^{-1}	
			Calc.	Obs.	Calc.	Obs.
KCl–OH^-	584	0.2801	297.43	297[14], 293[15]	0.195	0.21[16], 0.18[3]
KBr–OH^-	470	0.2102	308.41	309[14], 309.7[15]	3.72	—
KI–OH^-	385	0.2015	286.32	279[14]	2.86	—
NaCl–OH^-	736	0.2018	392.16	390[14], 385[15]	1.65	1.60[17]
RbCl–OH^-	621	0.3178	263.35	270[14]	0.015	—
KCl–OD^-	584	0.3310	232.01	231.5[14]	—	—
KBr–OD^-	470	0.2611	232.54	233[14], 235[15]	—	—
KI–OD^-	385	0.2514	201.86	213[15]	—	—
NaCl–OD^-	736	0.2517	286.32	—	—	—

Note: Superscripts indicate the Ref. Nos.

7 give respectively the calculated values of the tunnelling frequencies as obtained by our calculations and those obtained by different experiments. We can clearly see that the limited data of tunnelling frequencies are also explained well in terms of our model calculations.

References

1 Narayanamurti V & Pohl R O, *Rev Mod Phys (USA)*, **42** (1970) 201.

2 Schearer L D & Estle T L, *Solid State Commun (USA)*, **4** (1966) 639.

3 Bron W E & Dreyfus R W, *Phys Rev (USA)*, **163** (1967) 304.

4 Wedding B & Klein M V, *Phys Rev (USA)*, **177** (1969) 1274.

5 Lawless W N, *J Phys & Chem Solids (USA)*, **28** (1967) 1755.

6 Chandra S, Agrawal V K & Pandey G K, *J Phys & Chem Solids (USA)*, **30** (1969) 1644.

7 Pandey G K & Shukla D K, *Phys Rev B (USA)*, **3** (1971) 4391.

8 Kielich S, *Acta Phys Pol (Poland)*, **22** (1962) 65.

9 Private communication to G K Pandey, 1983.

10 Pandey G K & Shukla D K, *Phys Rev B (USA)*, **4** (1971) 4598.

11 Brauer P, *Z Naturforsch a (Germany)*, **7** (1952) 372.

12 Mott N F & Gurney R W, *Electronic processes in ionic crystals* (Clarendon Press, London), 1940.

13 Roberts S, *Phys Rev (USA)*, **81** (1951) 865.

14 Klein M V, Wedding B & Levine M A, *Phys Rev (USA)*, **180** (1969) 902.

15 Harrison D & Luty F, *Far infrared librational excitations of* OH^- and OD^- *dipoles in alkali halides*, paper presented to the International Symposium of Color Centers in Alkali Halides, Rome, 1968.

16 Feher G, Shepherd I W & Shore H B, *Phys Rev Lett (USA)*, **16** (1966) 501; **16** (1966) 1187.

17 Eldrich R E, Burke W J & McCarthy K A, *Solid State Commun (USA)*, **5** (1967) 899.

Indian Journal of Pure & Applied Physics
Vol. 21, October 1983, pp. 573-578

Frequency & Temperature Dependence of Dielectric & Electromechanical Parameters of Soft Piezoelectric Materials Developed at NPL

G C JAIN, V N BINDAL, JANARDAN SINGH, VED SINGH, N NARAYANA SWAMI & N C SONI
Division of Materials, National Physical Laboratory, New Delhi 110012

Received 9 *August* 1982; *revised received* 14 *January* 1983

The frequency and temperature dependence of dielectric constant (K_3^T), dielectric loss factor (tan δ) and some of the electromechanical properties of four soft piezoelectric materials for low power applications, developed at NPL, have been studied. The measurements of K_3^T and tan δ carried out over the frequency range from 1 kHz to 1.5 MHz at room temperature have been reported. The variation of K_3^T, tan δ and electrical resistivity over the temperature range from −50 to 200 C, and planar coupling factor, frequency constant and mechanical quality factor over the temperature range from −80 to 100 C have been presented. These studies reveal that there exists a distinct difference in variation of various dielectric and electromechanical parameters with temperature for these materials. The temperature and frequency characteristics of the different parameters are quite useful for the fabrication of transducers for various low power applications.

1 Introduction

It is well established that in the range of morphotropic phase boundary, the electromechanical properties of lead zirconate titanate ceramics are more pronounced and exhibit a two-phase system with tetragonal and rhombohedral structures. In case of exactly identical ceramic processing parameters, the dielectric and electromechanical properties of these ceramics depend strongly on the additives as well as on the Zr/Ti ratio. The various additives used for modifying the electromechanical properties may be divided under three broad categories, viz. softeners (La, Nb)[1], hardners (Fe, Sc)[2,3] and stabilizers (Cr, Mn)[4,5]. The additives like La_2O_3, Nb_2O_5 and Ta_2O_5 (Ref. 1) and WO_3 (Refs 6 and 7) in $Pb(Zr, Ti)O_3$ are known to produce soft piezoelectric ceramics characterized by low mechanical quality factor and relatively higher dielectric constant and dielectric loss factor along with higher electromechanical coupling factor suitable for low power, general purpose electromechanical transducers.

Apart from the room temperature dielectric and electromechanical properties, the temperature characteristics of these parameters of the transducer materials play an important role in the ultimate performance of various ultrasonic and piezoelectric devices. As such data were not available to the indigenous users of piezoelectric materials for low power applications, studies were carried out by us and data in respect of the four soft piezoelectric materials developed at NPL and detailed in the following, are presented in this paper. These materials are the modified forms of lead zirconate titanate, and have been designated as NPLZT-5, NPLZT-5A, NPLZT-5B and NPLZT-$5H_1$ (the first three letters, viz. NPL, are after the name of the Laboratory).

NPLZT-5—It has relatively high electromechanical coupling coefficient, and is suitable for general purpose low power applications, e.g. for making acoustic sensing devices, probes for flaw detectors, bimorph elements, etc.

NPLZT-5A—It possesses higher coupling coefficient and higher voltage sensitivity as compared to NPLZT-5. These properties make it suitable for impact-type gas igniters and also for low power transducers. It also has a higher Curie temperature as compared to NPLZT-5.

NPLZT-5B—It has relatively low mechanical quality factor and is suitable for making probes for flaw detectors. It is similar to NPLZT-5A in most other respects.

NPLZT-$5H_1$—It has high dielectric constant and highest charge sensitivity as compared to the other three piezoelectric materials mentioned above. Typical applications of this material are in making gramophone pickup elements, microphones, hydrophones, etc.

The values of electrical, electromechanical and physical constants at room temperature (28.5°C) for these materials are given in Table 1.

2 Experimental Details

The indigenously available raw materials, such as lead oxide, titanium oxide and zirconium oxide along with suitable additives like La_2O_3, Nb_2O_5, $SrCO_3$ and Ta_2O_5 were used in proper proportions to prepare the various grades of piezoelectric ceramic materials; a flow-chart of the procedure followed is given in Fig. 1 and brief details of each step of the procedure are reported elsewhere[8,9]. The sample pieces in the form of discs (diameter, 20 mm; and thickness, 1 mm) were prepared, electroded with fired-on silver and poled[8,9]

Table 1 — Typical Room Temperature Data (Low signal) for Various Soft Piezoelectric Materials Developed at NPL

Properties	Symbol	Unit	NPLZT-5	NPLZT-5A	NPLZT-5B	NPLZT-5H$_1$
Electrical properties						
Dielectric constant	K_3^T	—	1750	1550	1450	2500
Dielectric loss factor	$\tan\delta$	—	0.02	0.02	0.02	0.02
Resistivity	ρ_{el}	Ω-cm	$\sim 10^{13}$	$\sim 10^{13}$	$\sim 10^{13}$	$\sim 10^{13}$
Electromechanical properties						
Planar coupling coefficient	k_p	—	0.55	0.60	0.58	0.52
Piezoelectric charge constant	d_{33}	10^{-12} C/N	330	360	338	380
Piezoelectric voltage constant	g_{33}	10^{-3} V.m/N	21.3	26.2	26.3	17.2
Mechanical and thermal properties						
Mechanical quality factor	Q_m	—	85	75	65	70
Frequency constant	N_{3t}	m.Hz	1900	1950	1900	1900
Density	ρ_m	10^3 kg/m^3	7.5	7.6	7.6	7.5
Curie temp.	Θ	°C	285	340	345	195

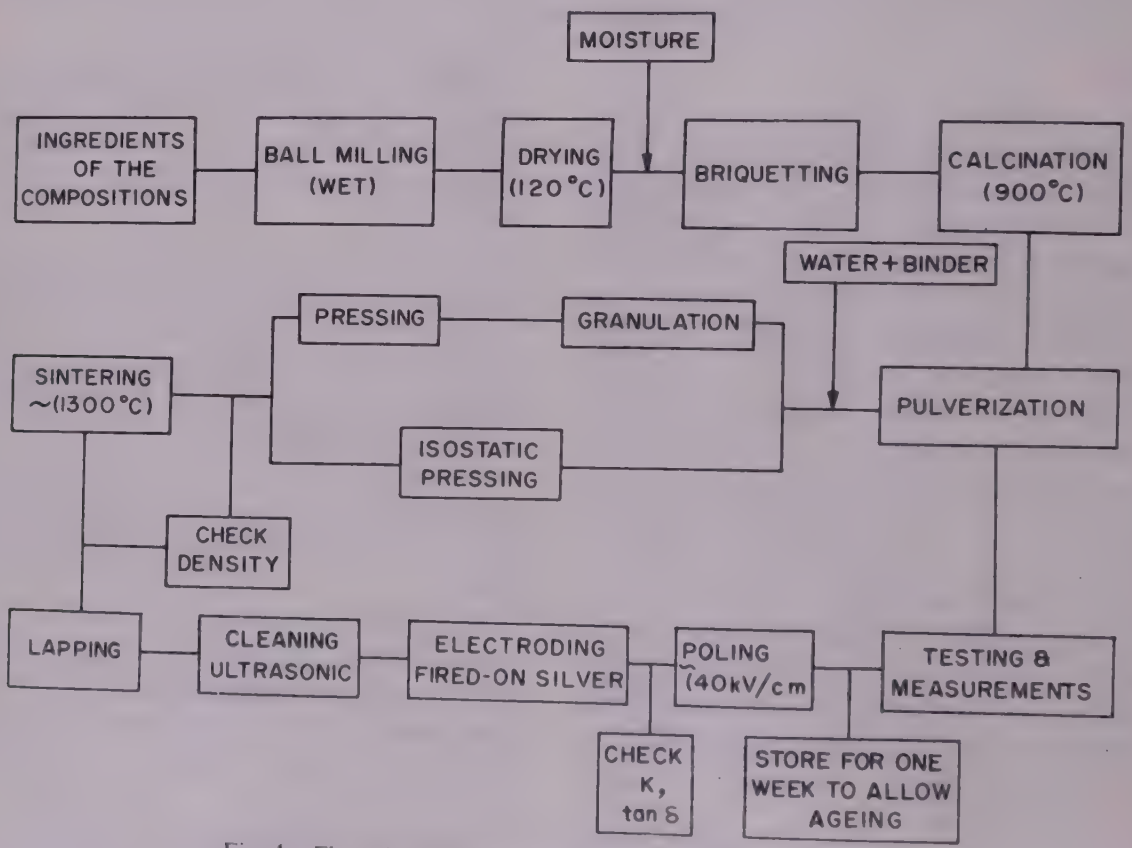

Fig. 1 — Flow-chart for manufacturing piezoelectric materials

with a dc electric field of 3-4 kV/mm at elevated temperature.

The variation of electromechanical parameters with temperature was measured in the temperature range from −80 to 100 C and that of dielectric parameters with temperature in the range from −50 to 200 C, employing various measurement set-ups described below.

Measurements at room temperature —The measurements of electrical, electromechanical and mechanical parameters at room temperature were carried out after a lapse of one week of the poling of the discs to effect the stabilization of various parameters due to ageing. While the measurements of capacitance and dielectric loss factor ($\tan\delta$) at 1 kHz were made by 0.1% LCR Bridge, the same from 10 kHz to 1.5 MHz were measured by Siemens Impedance Bridge-Type R-2077. The measurements of resistivity were carried out by employing Keithley Electrometer Amplifier Model 610 along with Resistivity Adopter-6105, by applying a dc field of 250 V/mm to the samples. The electromechanical parameters were measured in accordance with the 1961-IRE standards on piezoelectric crystals (Ref. 10). The piezoelectric charge constant (d_{33}) was measured by employing Berlingcourt's d_{33}-meter model CPDT-3300 (Channel Products Inc., USA). The mechanical

quality factor (Q_m) and piezoelectric voltage constant (g_{33}) were derived from the measured values of dielectric and electromechanical parameters with the help of the following expressions:

$$Q_m = \frac{f_n^2}{2\pi f_m Z_m C (f_n^2 - f_m^2)}$$

$$g_{33} = \frac{d_{33}}{\varepsilon_0 K_3^T}$$

where ε_0 is the permittivity of free space (8.85×10^{-12} F/m), K_3^T the dielectric constant, Z_m the magnitude of minimum impedance in ohms and C the capacitance measured at 1 kHz in picofarads, and f_n and f_m are the frequencies of the maximum and the minimum impedances respectively.

Measurements at low temperature—Fig. 2 shows a schematic diagram of the experimental set-up used for measuring the variations of electrical parameters, viz. K_3^T, $\tan\delta$ and resistivity (ρ_{el}), and electromechanical parameters, viz. planar coupling factor (k_p) and frequency constant (N_{3t}) in the temperature range from -100 to $+100$°C. The sample was kept in the sample holder loaded with spring to ensure a good electrical contact at all temperatures. The thermocouple was suitably inserted to record the temperature at the sample. Pyrex glass wool insulation was inserted between the inner sample cell and the outer container and the whole assembly was placed in a thermocole box in which liquid nitrogen was poured to obtain the desired low temperature. The thermocole box was covered at the top to reduce further the radiation effect. A dehydrant (calcium chloride) was kept in the sample cell to avoid frosting on the sample at low temperature. The sample cell chamber was also wound with a heating coil to obtain higher temperature. The sample was connected to various measuring instruments depending on the requirements of the measurements as shown in Fig. 2.

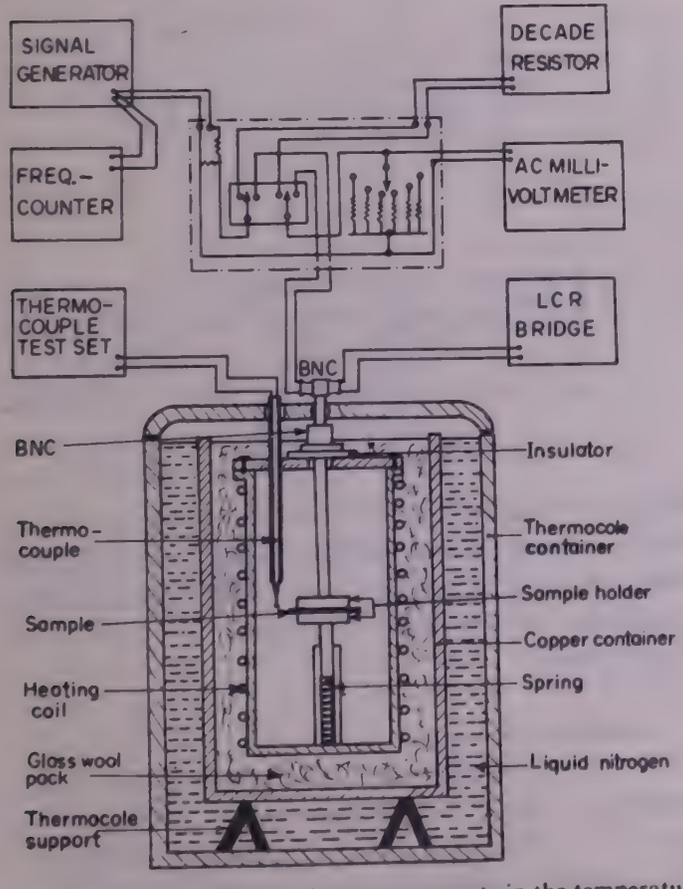

Fig. 2—Experimental set-up for measurements in the temperature range from -100 to $+100$°C

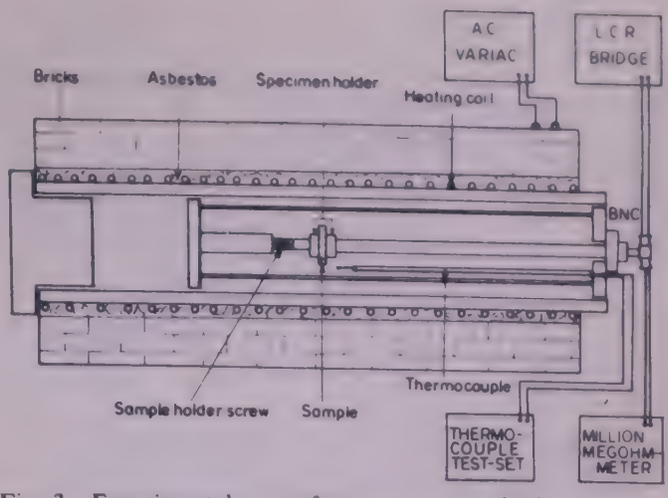

Fig. 3—Experimental set-up for measurements in the temperature range from room temperature to 400 C

Measurements above room temperature—The variations of different electrical and electromechanical parameters with temperature above room temperature were measured by the set-up shown in Fig. 3. The sample was placed in a specimen holder in which a thermocouple was also attached in such a way that the thermocouple was near to the sample. The sample holder was kept inside a wire-wound tubular muffle furnace in such a way that the sample's position was in the middle of the furnace to ensure uniform temperature all over the sample. The temperature was recorded by measuring the e.m.f. of the thermocouple with the help of thermocouple test-set (Fig. 3). The heating rate of about 2°C/min was maintained and the temperatures were kept constant for about 15 min before each observation at a particular temperature. In the overlapping temperature range, i.e. from room temperature to 100°C, the two experimental set-ups (Figs 2 and 3) were so chosen that uniformity of the working thermal conditions in both the cases could be established beyond doubt.

3 Results and Conclusions

The compositions for NPLZT-5, NPLZT-5A, NPLZT-5B and NPLZT-5H$_1$ are donor-doped lead zirconate titanate materials close to the morphotropic phase boundary with suitable additives to alter the temperature and frequency characteristics of dielectric and piezoelectric properties. These modifications make

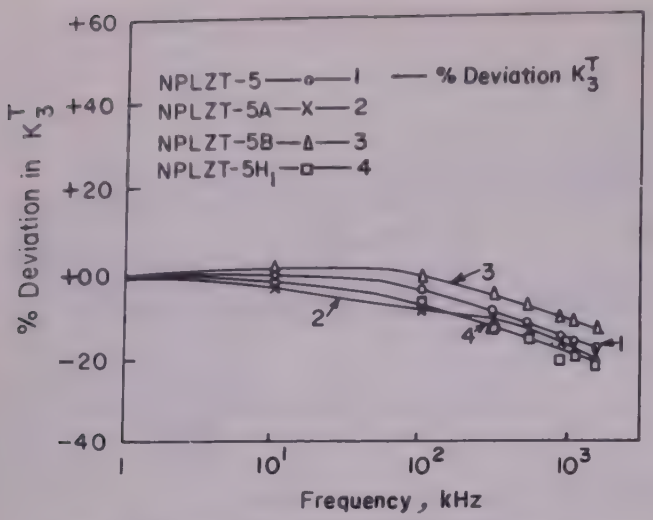

Fig. 4—Dielectric constant (K_3^T) versus frequency

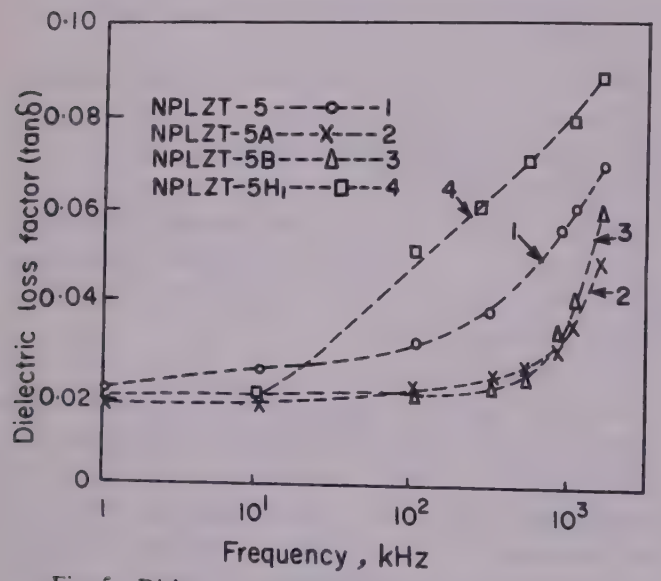

Fig. 5—Dielectric loss factor (tan δ) versus frequency

them suitable for applications in various low power ultrasonic and piezoelectric devices. The frequency and temperature dependence of K_3^T and tan δ and temperature dependence of electromechanical parameters, namely k_p, N_{3t}, Q_m and ρ_{el} for these materials are described in the following sections.

3.1 Frequency Dependence

The variations of per cent deviation in K_3^T and tan δ with frequency are depicted in Figs 4 and 5 respectively. It is seen from Fig. 4 that, for all the materials, below 200 kHz there is not much variation in K_3^T in comparison to 1 kHz values. Beyond 200 kHz there is slight decrease in K_3^T and this decrease is maximum for NPLZT-5H$_1$. The dielectric loss increases with increase of frequency for all the materials, which is in accordance with the behaviour of soft materials[11], i.e. donor-doped piezoelectric materials (Fig. 5).

It can be seen from Figs 4 and 5 that there is comparatively large variation in both K_3^T and tan δ for

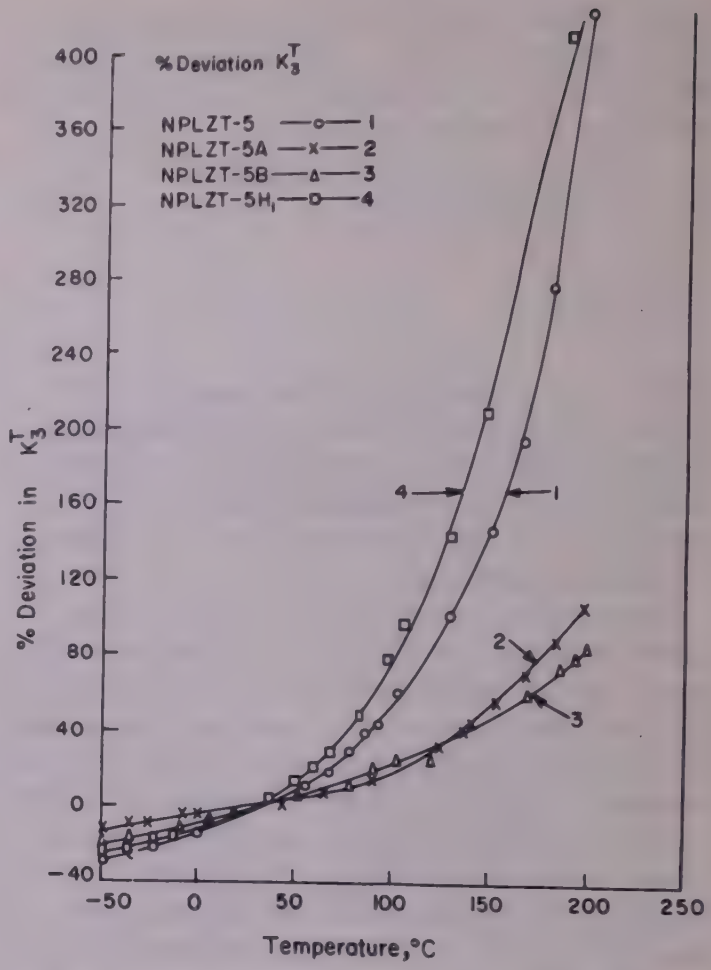

Fig. 6—Dielectric constant (K_3^T) versus temperature

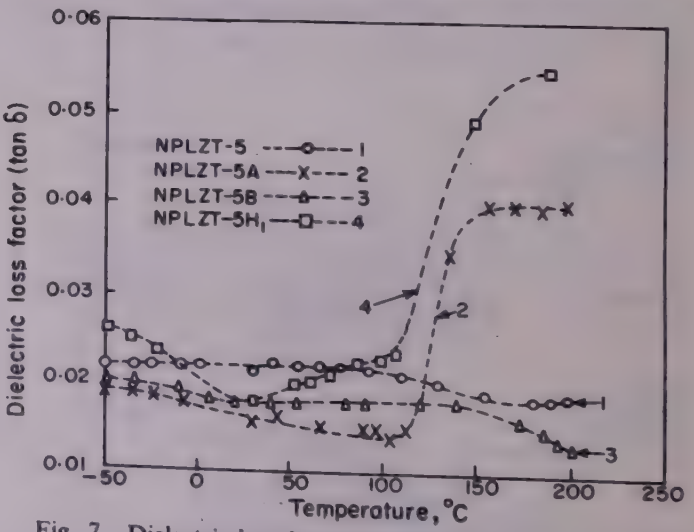

Fig. 7—Dielectric loss factor (tan δ) versus temperature

NPLZT-5H$_1$ compared to other materials. In view of lower variation of tan δ with frequency for NPLZT-5A, it may suitably be used for fabricating high frequency transducers where low loss factor is one of the requirements.

3.2 Temperature Dependence

The variations of K_3^T and tan δ with temperature are depicted in Figs 6 and 7 respectively. Fig. 6 shows that there is a relatively large variation in K_3^T for NPLZT-5H$_1$ which is due to its having lower Curie temperature compared to the other three materials

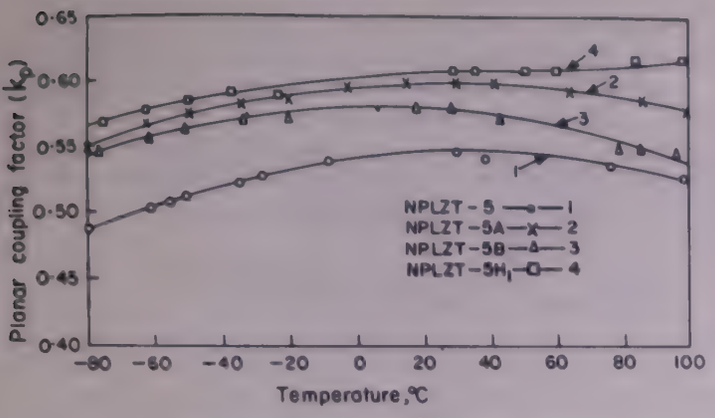

Fig. 8—Planar coupling factor (k_p) versus temperature

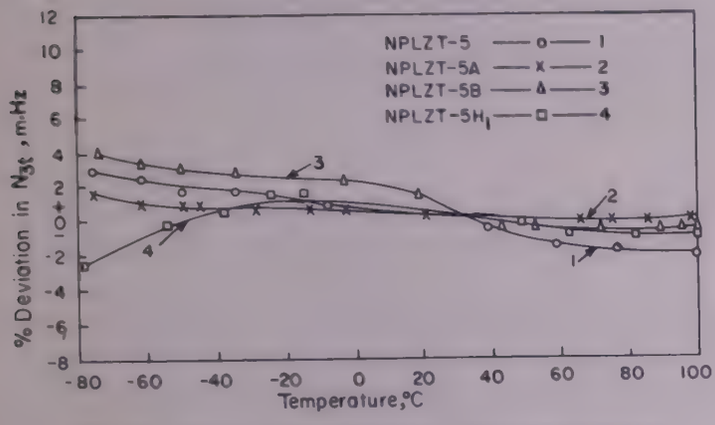

Fig. 9—Frequency constant (N_{3t}) versus temperature

studied. The deviation in K_3^T is least for NPLZT-5B. Fig. 7 shows that there is no appreciable change in tan δ for NPLZT-5B over the entire temperature range studied.

The planar coupling factor (k_p) measurements over the temperature range from −80 to 100°C (Fig. 8) show a similar variation for almost all the materials. The decreasing trend of k_p below room temperature has been observed for all the compositions.

There is relatively large variation in frequency constant (N_{3t}) on the lower side of the temperature (−80°C) compared to the higher side (+100°C) (Fig. 9). The deviation in N_{3t} over the entire temperature range is comparatively lower for NPLZT-5A, which makes it suitable for applications where relatively low variation in N_{3t} with temperature along with high electromechanical coupling coefficient is required. Further, NPLZT-5B would be a better material for applications involving relatively higher temperatures, as the variations of K_3^T, tan δ and other piezoelectric parameters with temperature (Figs 6-9) are comparatively lower than those with other materials studied. Similarly, for applications below room temperature, NPLZT-5A may be preferred. NPLZT-5 and NPLZT-5H$_1$ should be used preferably below 80°C because of relatively higher variations of dielectric and piezoelectric properties above 80°C.

It is seen that the per cent deviation in Q_m with temperature, as depicted in Fig. 10, is relatively less

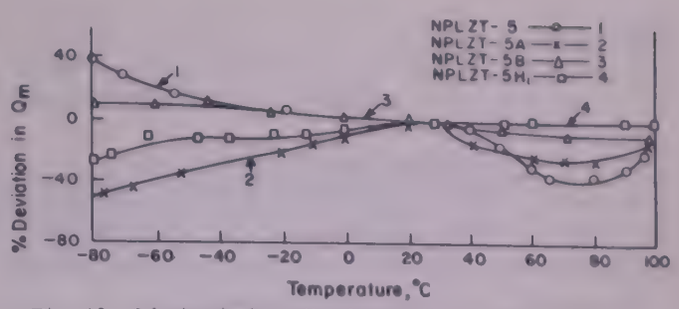

Fig. 10—Mechanical quality factor (Q_m) versus temperature

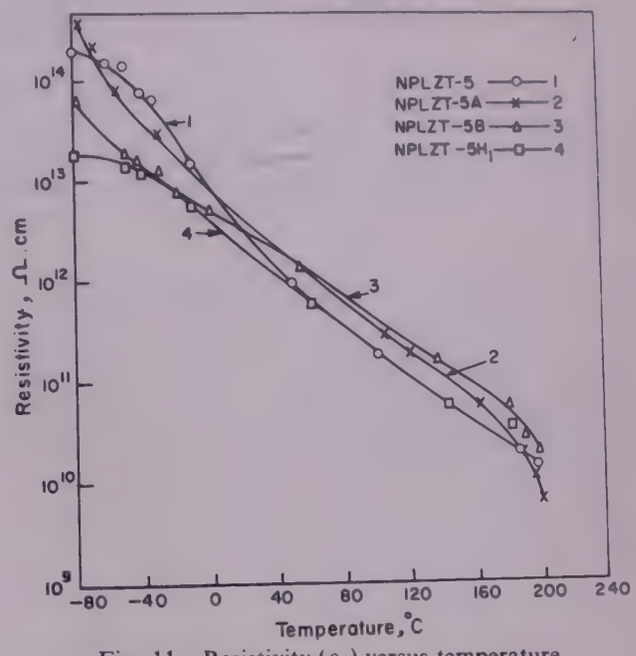

Fig. 11—Resistivity (ρ_{el}) versus temperature

above room temperature. This variation is almost similar to the variation in N_{3t} (Fig. 9).

The resistivity (ρ_{el}) for all the materials studied decreases with increase in temperature (Fig. 11). There is relatively sharp decrease in ρ_{el} for NPLZT-5A compared to NPLZT-5B and NPLZT-5H$_1$. The decrease in ρ_{el} with temperature is common to all these piezoelectric materials but it is higher enough for effective poling at elevated temperatures. The curves of Fig. 11 thus provide information about the optimum temperatures for effective poling, as at higher temperatures the poling may not be adequate because of appreciable drop in ρ_{el}.

NPLZT-5B featuring low value of Q_m along with better temperature characteristics is ideally suited for low power applications, such as probes for flaw detectors, thickness gauges, accelerometers, etc. Further, the decrease in Q_m with increase in temperature in the case of NPLZT-5B (Fig. 10) makes it a favoured transducer material, requiring relatively low Q_m at higher temperatures.

Acknowledgement

The authors wish to thank Dr A P Mitra, Director, National Physical Laboratory, New Delhi, for his permission for publishing the present work.

References

1 Sugden J A, Ferroelectric Ceramic Materials, US Pat., 3,068,177 (to British Crystal Co Ltd, Hythe, Southampton, England) 11 December 1962.

2 Kulcsar F, *J Am Ceram Soc (USA)*, **42** (1959) 343.

3 Weston T B, Webster A H & McNamara V M, *J Am Ceram Soc (USA)*, **52** (1962) 253.

4 Uchida H & Heeda T, *Jpn J Appl Phys (Japan)*, **6** (1967) 1292.

5 Thomann H, *Ferroelectrics (GB)*, **4** (1972) 141.

6 Kulcsar F, *J Am Ceram Soc (USA)*, **48** (1965) 54.

7 Andreeva V I & Domenko D S, *Inorg Mater (USA)*, **12** (1976) 805.

8 Bindal V N, Singh J, Soni N C & Narayana Swami N, *J Pure & Appl Ultrason (India)*, **1** (1979) 98.

9 Bindal V N & Singh J, *Ferroelectrics (GB)*, **41** (1982) 179.

10 IRE Standards on piezoelectric crystals: Measurements on piezoelectric ceramics, *Proc Inst Radio Eng (Australia)*, **49** (1961) 1161.

11 Barchaim N, Brunstein M, Grunberg J & Seidman A, *Ferroelectrics (GB)*, **6** (1974) 299.

Indian Journal of Pure & Applied Physics
Vol. 21, October 1983, pp. 579-581

Isentropic Compressibilities from Ultrasonic Studies on Binary Mixtures of di-*n*-Butylamine with *n*-Alcohols

M RAMAMURTHY, G S SASTRY & P R NAIDU
Department of Chemistry, College of Engineering, Sri Venkateswara University, Tirupati 517502

Received 13 *September* 1982; *revised received* 15 *January* 1983

Isentropic compressibilities for binary mixtures of di-*n*-butylamine with 1-butanol, 1-pentanol, 1-hexanol and 1-heptanol were computed from precession sound speed and density data. The sound speed and density data were also used to calculate intermolecular free-lengths of Jacobson for individual components and the binary mixtures. Both isentropic compressibility and intermolecular free-length exhibit negative deviation from ideality over the entire range of composition. The negative deviations suggest that there exists strong H-bond interaction between unlike molecules in the mixtures.

1 Introduction

Isentropic compressibilities and deviations in isentropic compressibility for binary mixtures of *n*-butylamine with 1-propanol, 1-butanol, 1-pentanol and 1-hexanol have been reported by Krishnaiah and Naidu[1]. Deviations in isentropic compressibility for the four mixtures were negative over the whole range of composition. The results were used to point out that strong H-bond interaction leads to decrease in intermolecular free-lengths between the molecules in the mixture.

Introduction of an additional butyl group in the aminofunction may modify the degree of interaction between unlike molecules and hence the intermolecular free-lengths. This will, in turn, influence the deviations in isentropic compressibility. With a view to studying this influence, new compressibility data and intermolecular free-lengths for mixtures of di-*n*-butylamine with the four alcohols were computed at 303.15 K from precession sound speed and density data, and the results are presented in this paper.

2 Experimental Details

Di-*n*-butylamine was dried over potassium hydroxide for 3 days, refluxed for 2 hr and fractionally distilled. 1-Butanol, 1-pentanol, 1-hexanol and 1-heptanol were purified by methods described in the literature[2]. The purity of the samples was checked by comparing the experimental densities with those reported in the literature[3]. The data are given in Table 1.

Isentropic compressibilities (K_s) were computed from densities (ρ) and sound velocities (u) determined at 303.15 K using the relation

$$K_s = u^{-2}\rho^{-1} \qquad \ldots (1)$$

where u is the ultrasonic sound velocity and ρ the density. Sound velocity was measured with a variable-path, single-crystal ultrasonic interferometer at a frequency of 2 MHz. Water was circulated at 303.15 ± 0.01 K from a thermostatically controlled bath into a jacket around the measuring space of the interferometer cell to maintain the experimental liquid at a constant temperature during the experiment. The values obtained were accurate to $\pm 0.15\%$. Density data were computed from experimental excess volumes reported elsewhere[4] using the relation:

$$\rho = \frac{x_1 M_1 + x_2 M_2}{V + V^E} \qquad \ldots (2)$$

where x_1, x_2 and M_1, M_2 stand for the mole fractions and molecular weights of amine and alcohol respectively. V and V^E are the molar and excess volumes respectively. The density values obtained were accurate to $\pm 5 \times 10^{-5}$ gcm^{-3}. The values of K_s calculated from Eq. (1) were accurate to ± 2 TPa^{-1}.

The deviations in isentropic compressibility (ΔK_s) were computed employing the equation

$$\Delta K_s = K_s - \varphi_1 K_{s,1} - \varphi_2 K_{s,2} \qquad \ldots (3)$$

where K_s, $K_{s,1}$ and $K_{s,2}$ are the isentropic compressibilities of the mixture and pure components and φ_1, φ_2 are the volume fractions of amine and alcohols. Isentropic compressibility for an ideal mixture was assumed to be additive with respect to volume fraction.

Table 1—Density of the Pure Component Liquids

Component liquid	T(K)	Density, gcm^{-3}	
		Present work	Literature
Di-*n*-butylamine	303.15	0.75519	—
1-Butanol	303.15	0.80202	0.80206
1-Pentanol	303.15	0.80769	0.80764
1-Hexanol	303.15	0.81209	0.81201
1-Heptanol	303.15	0.81571	—

Intermolecular free-lengths were calculated for pure components and mixtures using the equation:

$$L_f = \frac{K}{u_{ex}\rho_{ex}^{1/2}} \quad \ldots (4)$$

Intermolecular free-lengths for ideal mixtures were calculated using the relation:

$$L_{f_1}x_1 + L_{f_2}x_2 = L_{f_{ideal}} \quad \ldots (5)$$

Intermolecular free-lengths for ideal mixtures were assumed to be additive in terms of mole fractions. Excess intermolecular free-lengths for the four mixtures were calculated using the relation:

$$L_f^E = L_{f_{real}} - L_{f_{ideal}} \quad \ldots (6)$$

The value of K reported in literature[5,6] was taken for the calculation of intermolecular free-lengths.

3 Results and Discussion

Isentropic compressibilities and deviations in isentropic compressibility are given in columns 4 and 5 of Table 2. The results are also presented graphically along with those reported by Krishnaiah and Naidu. Excess intermolecular free-lengths (L_f^E) are given in column 6 of Table 2.

Deviation in isentropic compressibility (ΔK_s) for the four mixtures is negative over the entire range of composition. The negative values suggest that sound waves cover longer distances due to decrease in intermolecular free lengths. Excess intermolecular free-lengths (L_f^E), which are negative, justify this contention. The decrease in intermolecular free-lengths may be ascribed to dominant nature of H-bond interaction between unlike molecules. Further, the curves in Fig. 1 show that deviations in isentropic compressibility for the 4 mixtures are less negative than those represented by Krishnaiah and Naidu. This observation shows that the second butyl group in di-*n*-butylamine influences intermolecular free lengths and hence isentropic compressibility by contributing to new geometric factors.

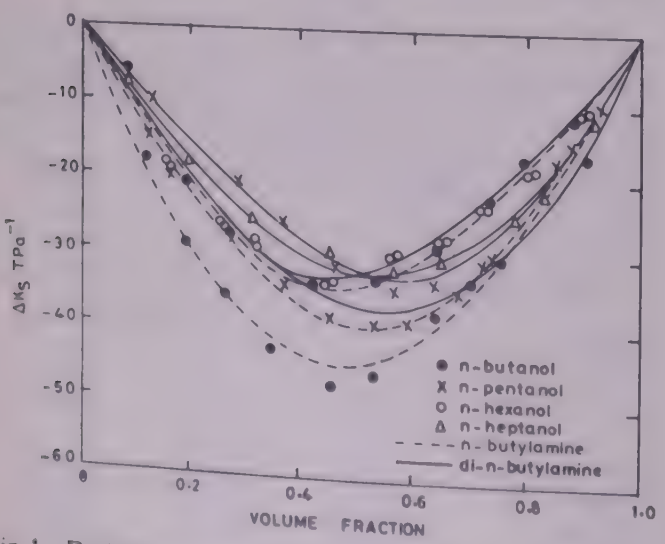

Fig. 1—Deviation in isentropic compressibilities (ΔK_s) with change in volume fraction of butylamine in binary mixture

Table 2—Experimental Isentropic Compressibility Values for the Four Binary Mixtures at 303.15 K

φ	ρ gcm^{-3}	u ms^{-1}	K_s TPa^{-1}	ΔK_s TPa^{-1}	L_f^E
System I: $\varphi[(CH_2)_3]_2NH + (1-\varphi)C_4H_9OH$					
0.00000	0.80202	1228	826	0	0.0000
0.19887	0.79707	1240	815	−21	−0.0073
0.29734	0.79409	1244	813	−28	−0.0098
0.40123	0.79053	1248	812	−34	−0.0121
0.57764	0.78331	1248	819	−37	−0.0126
0.070016	0.77617	1246	829	−33	−0.0112
0.74784	0.77352	1244	835	−30	−0.0102
0.78554	0.77109	1242	843	−27	−0.0071
0.84185	0.76713	1240	850	−22	−0.0075
0.90749	0.76227	1236	858	−16	−0.0050
1.00000	0.75519	1228	878	0	0.0000
System II: $\varphi[(CH_2)_3]_2NH + (1-\varphi)C_6H_{13}OH$					
0.00000	0.81209	1282	749	0	0.0000
0.15558	0.80614	1286	750	−19	−0.0067
0.25683	0.80199	1284	756	−26	−0.0094
0.31916	0.79930	1282	761	−29	−0.0104
0.46399	0.79215	1276	775	−33	−0.0115
0.55557	0.78716	1268	790	−30	−0.0103
0.65611	0.78100	1260	806	−27	−0.0091
0.72841	0.77617	1254	819	−23	−0.0078
0.82244	0.76940	1246	837	−18	−0.0060
0.91045	0.76255	1238	855	−11	−0.0008
1.00000	0.75519	1228	878	0	0.0000
System III: $\varphi[(CH_2)_3]_2NH + (1-\varphi)C_5H_{11}OH$					
0.00000	0.80769	1254	787	0	0.0000
0.12958	0.80334	1256	791	− 8	−0.0035
0.28467	0.79760	1258	794	−21	−0.0072
0.36650	0.79430	1258	798	−26	−0.0086
0.46326	0.78993	1260	799	−32	−0.0109
0.57445	0.78438	1246	810	−34	−0.0061
0.64285	0.78040	1256	817	−33	−0.0114
0.79152	0.77145	1250	834	−24	−0.0100
0.86479	0.76562	1240	852	−17	−0.0054
0.92236	0.76126	1234	862	−10	−0.0028
1.00000	0.75519	1228	878	0	0.0000
System IV: $\varphi[(CH_2)_3]_2NH + (1-\varphi)C_7H_{15}OH$					
0.00000	0.81571	1310	713	0	0.0000
0.07299	0.81348	1308	718	− 7	−0.0027
0.19399	0.80868	1304	727	−18	−0.0065
0.30624	0.80333	1298	738	−25	−0.0087
0.44751	0.79555	1288	757	−29	−0.0100
0.56324	0.78812	1280	774	−31	−0.0107
0.65220	0.78225	1272	790	−30	−0.0102
0.78117	0.77282	1258	817	−24	−0.0080
0.83360	0.76881	1252	829	−21	−0.0068
0.92059	0.76181	1240	853	−11	−0.0037
0.00000	0.75519	1228	878	0	0.0000

Table 3—Values of the Constants b_0, b_1, b_2 and $\sigma(\Delta K_s)$ at 303.15 K

(Values are in TPa^{-1})

System	b_0	b_1	b_2	$\sigma(\Delta K_s)$
I	−142.14430	−28.04724	−23.87823	1
II	−122.35822	7.53293	−29.70496	1
III	−133.51197	−52.35616	41.02965	1
IV	−132.32882	−30.66145	15.10023	2

The values of ΔK_s may be expressed by an empirical equation of the form

$$\Delta K_s/TPa^{-1} = \varphi_1\varphi_2[b_0 + b_1(\varphi_1 - \varphi_2) + b_2(\varphi_1 - \varphi_2)^2] \quad \ldots (7)$$

where b_0, b_1 and b_2 and adjustable parameters (Table 3). The values of the parameters were obtained by the method of least squares and they are represented in Table 3 along with the standard deviation $\sigma(\Delta K_s)$.

References

1 Krishnaiah A & Naidu P R, *Acta Chim Acad Sci (Hungary)*, **104**(3) (1980) 295.

2 Riddick J A & Bunger W B, *Organic solvents* (Wiley-Interscience, New York), 1970.

3 Timmermans J, *Physico-chemical constants of pure organic compounds* (Elsevier, New York), 1950.

4 Sastry G S, Ramamurthy M & Naidu P R, *Acta Chim Acad Sci (Hungary)*, 1983, in press.

5 Jacobson B, *J Chem Phys (USA)*, **20** (1952) 927.

6 Jacobson B, *Acta Chem Scand (Denmark)*, **6** (1952) 1485.

Indian Journal of Pure & Applied Physics
Vol. 21, October 1983, pp. 582-586

Radiation Damage in Some Synthetic High Polymers

M RAMAKRISHNA MURTHY* & S RADHAKRISHNA
Department of Physics, Indian Institute of Technology, Madras 600036

Received 17 *September* 1982; *revised received* 20 *December* 1982

Reaction damage in some synthetic high polymers such as polymethyl methacrylate (PMMA), polystyrene (PS), polyacrylonitrile (PAN), and poly cellulose acetate (PCA), has been studied using the experimental techniques such as thermoluminescence (TL), electron spin resonance (ESR) and optical absorption. Previous independent experimental results have remained uncoordinated and sometimes even mutually contradicting damage products have been identified.

1 Introduction

The study of radiation damage in polymers is of considerable interest because of the wide range of physical properties exhibited under different conditions. The general effects of ionizing radiations on the polymers have been studied[1-7]; the consequent effects on the physical and chemical properties, are as indicated in Fig. 1. Ultraviolet rays affect only the surface properties while the high energy radiations such as X-rays, γ-rays or electrons bring about both physical and chemical changes which, in turn, are dependent on whether the irradiation has been done in oxygen atmosphere. Depending on the radiation dose, temperature and other conditions, the polymer may either cross-link or degrade, or both may occur and one may be more predominant over the other. These affect the mechanical, electrical and optical properties depending on the nature of the radiation damage products. Several ESR studies, as reviewed by Campbell[8], to identify the damage products were unsuccessful due to the simultaneous existence of various damage products leading to overlapping spectra. Considering the thermal stabilities of various damage products it was thought that thermoluminescence (TL) experiments yield unambiguous identification of damage products. Such investigations have already been reported by the authors on PMMA[9] and PS[10]. The present study is aimed at identification of radiation damage products by a correlated study of TL, electron spin resonance (ESR) and optical absorption on certain X-irradiated polymers.

2 Experimental Details

Transparent samples of PMMA, PS, PAN and PCA are obtained commercially in the form of 5 mm × 5 mm × 2 mm sheets. The samples are irradiated on a Phillips X-ray Unit, operating at 30 kV and 20 mA. The radiation dose is determined by the time of irradiation.

TL is recorded by means of a UV-sensitive photomultiplier (RCA-931A) which is placed in front of the window of a specially designed cryostat. The output of the photomultiplier is recorded by means of a SERVOGAR double channel recorder. Heating rate of 20°/min is maintained during the TL experiments.

ESR spectra are recorded by a Varian E-4 spectrometer. Optical absorption spectra are recorded by a Cary-14 spectrophotometer.

3 Results and Discussion

Polymethyl methacrylate (PMMA)—Fig. 2 shows the TL spectra of X-irradiated PMMA. Curves 1, 2 and 3 show the spectra obtained in samples irradiated for 10 min, 15 min and 2 hr respectively. Two glow peaks are obtained in all the cases, one at 136 K and the other

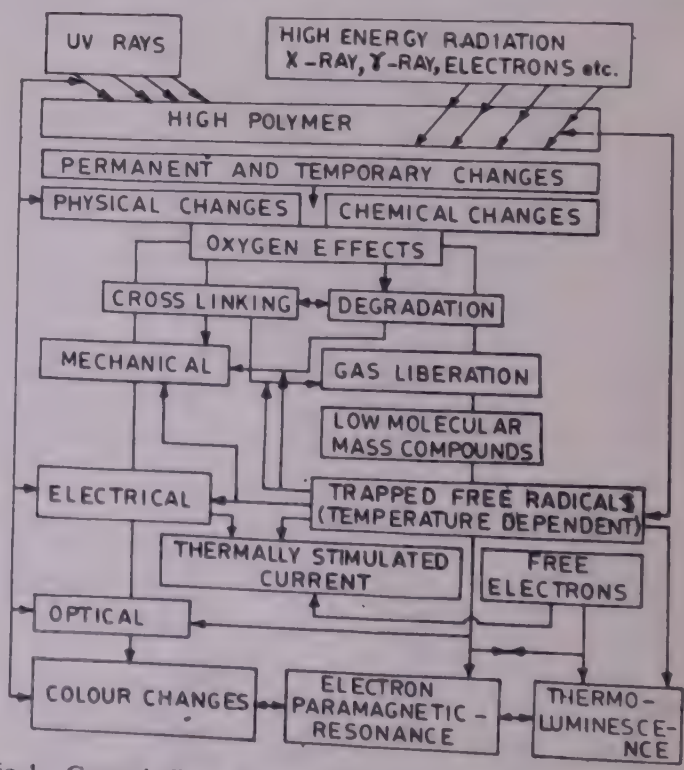

Fig. 1—General effects of ionizing radiations on polymers [Arrows indicate the occurrence of various phenomena arising from the formation of damage products and the techniques that can be employed]

*Present address: Department of Physics, Kakatiya University, Warangal 506009

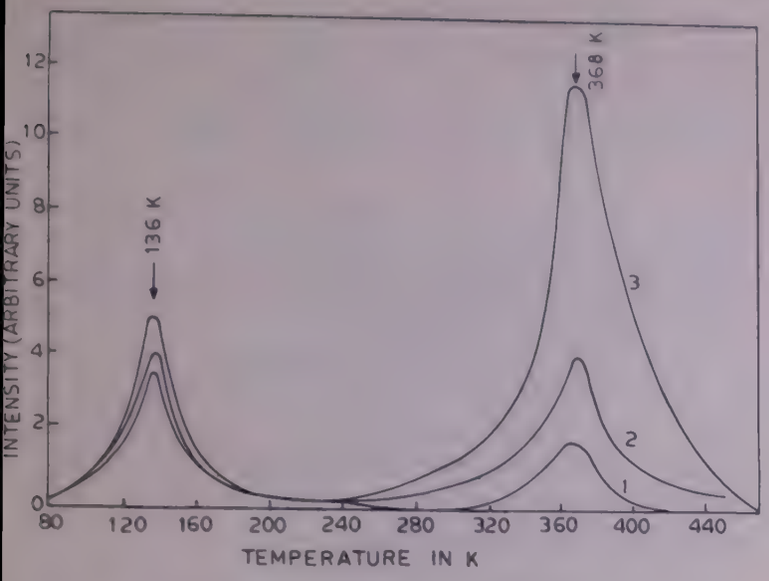

Fig. 2—Thermoluminescence spectra of polymethyl methacrylate)

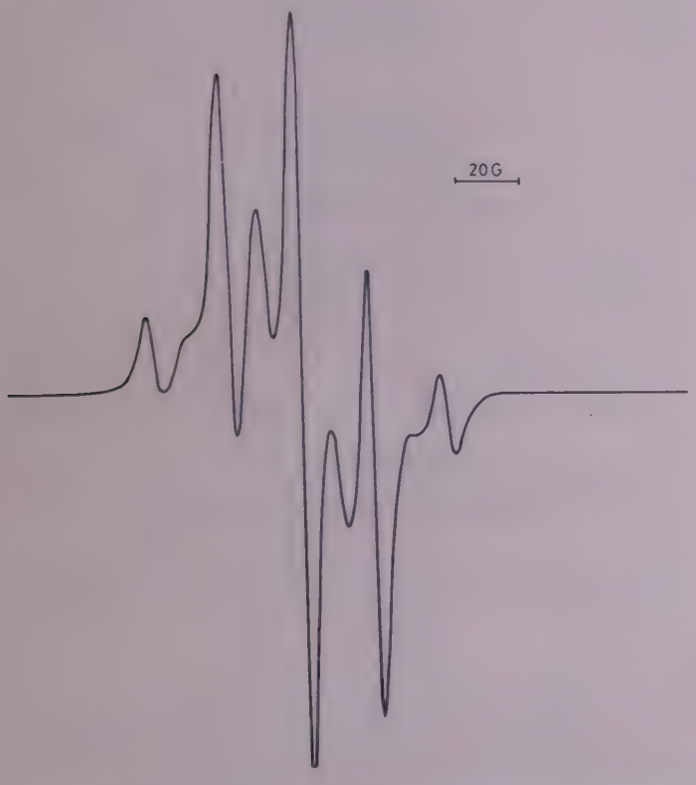

Fig. 3—Electron spin resonance spectrum of X-irradiated PMMA

at 368 K. It can also be observed that for higher doses, the species which is less thermally stable increases at a slower rate than the other.

Fig. 3 shows a typical ESR spectrum of irradiated PMMA, which is similar to that reported earlier[11]. The radiation damage product at room temperature in PMMA has been identified as the free radical[8]

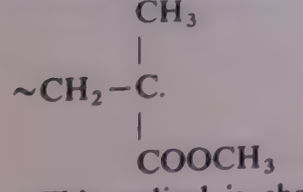

This radical is characterized by a nine-line ESR spectrum. There has been considerable controversy with regard to the origin of this spectrum. It was at first thought to be due to two different radicals, one giving rise to a five-line ESR pattern and the other to a four-line pattern. The primary evidence in favour of this hypothesis is that the intensity ratio of these two sets of lines changes with temperature. However, it was shown that there is a minor but stable radical which remains constant on heat treatment[12].

Fig. 4 shows the optical absorption spectra of PMMA samples. Curve 1 shows the spectrum of an unirradiated sample. Curves 2, 3 and 4 show the spectra of samples irradiated for 10 min, 1 hr and 5 hr respectively. A new band appears at 410 nm in addition to a rapidly rising UV absorption. The band at 410 nm is found to increase in intensity with radiation dose and decrease in intensity for samples irradiated and heated to above room temperature and no band is observed when heated to about 370 K.

When the irradiated samples are heated to 390 K, i.e. in the course of the appearance of the 368 K TL glow peak, the optical absorption band at 410 nm and the ESR lines disappear. This indicates that the species responsible for the 410 nm band and for the reported ESR lines and the TL glow at 368 K is the same. The TL glow peak at 136 K is attributed to the electrons or holes trapped at trace impurity sites in the matrix.

The relative change in intensities of the TL glow peaks at 136 and 368 K (Fig. 2) for the same dose of irradiation confirms the above conclusions.

Polystyrene (PS)—Fig. 5 shows the TL spectra of PS samples. Curves 1,2,3,4 and 5 show the spectra for the samples irradiated in air for 5 hr, 3 hr, 2 hr and in vacuum for 1 hr and 30 min respectively. For samples irradiated in air, three glow peaks at 160 K, 220 K, and 378 K are observed and in vacuum the 160 K peak is not observed. The intensity of the glow peaks increases with the radiation dose.

Fig. 6 shows a typical ESR spectrum for samples irradiated at room temperature. A poorly resolved 1:2:1 triplet similar to that reported earlier[13–16] is

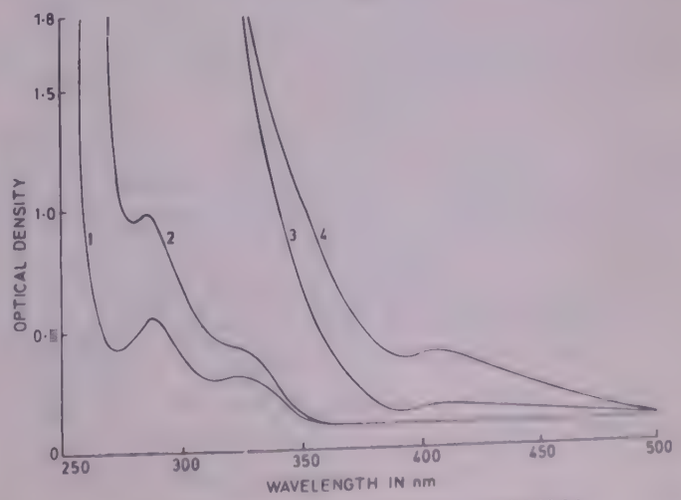

Fig. 4—Optical absorption spectra of PMMA

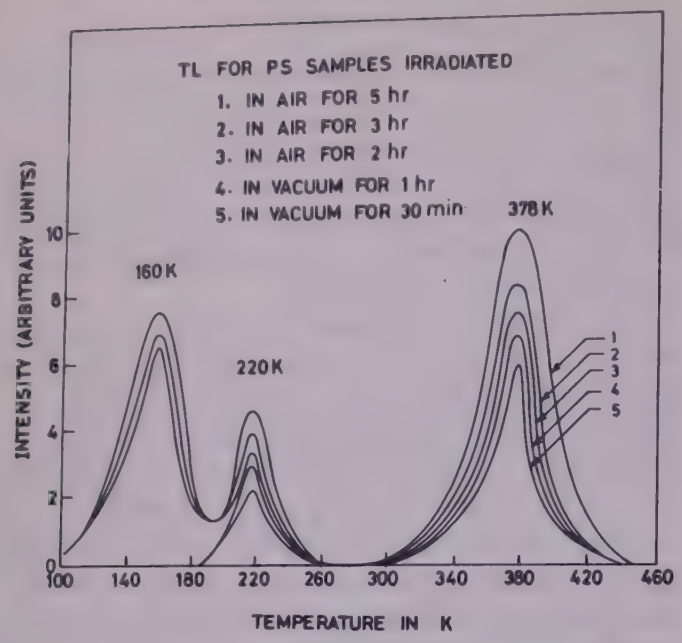
TL FOR PS SAMPLES IRRADIATED
1. IN AIR FOR 5 hr
2. IN AIR FOR 3 hr
3. IN AIR FOR 2 hr
4. IN VACUUM FOR 1 hr
5. IN VACUUM FOR 30 min
160 K
220 K
378 K
INTENSITY (ARBITRARY UNITS)
TEMPERATURE IN K

Fig. 5—Thermoluminescence spectra of polystyrene

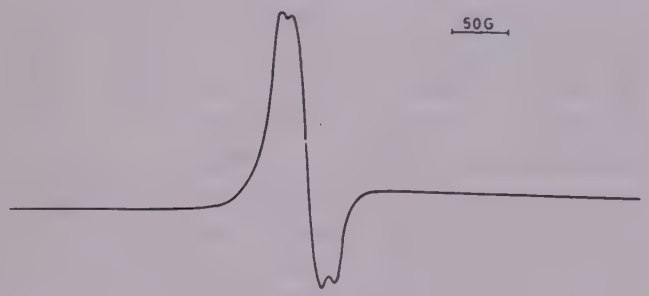

Fig. 6—Electron spin resonance spectrum of irradiated polystyrene

obtained which is attributed to the presence of various free radicals at different temperatures. The radiation damage products at LNT[16] are identified as cyclohexadienyl radicals formed by transfer of a hydrogen atom from the main chain to the phenyl ring, in the *meta* position, in addition to the chain radical $-CH_2-C(C_6H_5)-CH_2-$, which is thermally more stable.

The decay of the cyclohexadienyl radical on heating to room temperature is probably associated with the appearance of the TL glow peak with a maximum at 220 K (Fig. 5). The glow peak with maximum at 378 K may be attributed to the decay of the chain radical $-CH_2-C(C_6H_5)-CH_2-$.

The glow curve at 160 K, which is not observed for samples irradiated in vacuum, is similar to that obtained by Tomita[17] and is attributed to be due to the peroxy radicals formed at the ends of the chains on irradiation in air. Carbonyl groups are considered to be the more probable luminescence centres. Spectral studies may yield more information about these carbonyl groups, in which case the vibrational stretching frequencies of the carbonyl groups must coincide with the spectrum and frequency interval of the TL peak.

Polyacrylonitrile (PAN)—Fig. 7 shows the TL spectra of irradiated PAN. A glow peak has been observed with maximum at 362 K. No glow peak has been observed in the low temperature range.

Fig. 8 shows the ESR spectra of PAN samples irradiated and heated to various temperatures. As the temperature is increased from 273 K, the hyperfine structure gradually disappeared at about 373 K. The hyperfine structure may be constructed by assuming the interaction of the unpaired electron with one α proton and two equivalent β protons in such a radical, as reported by Hasegewa and Shimazu[19], i.e. $-CH_2-CH(CN)-CH-CH(CN)-CH_2-$. Thus this radical decays at about 373 K.

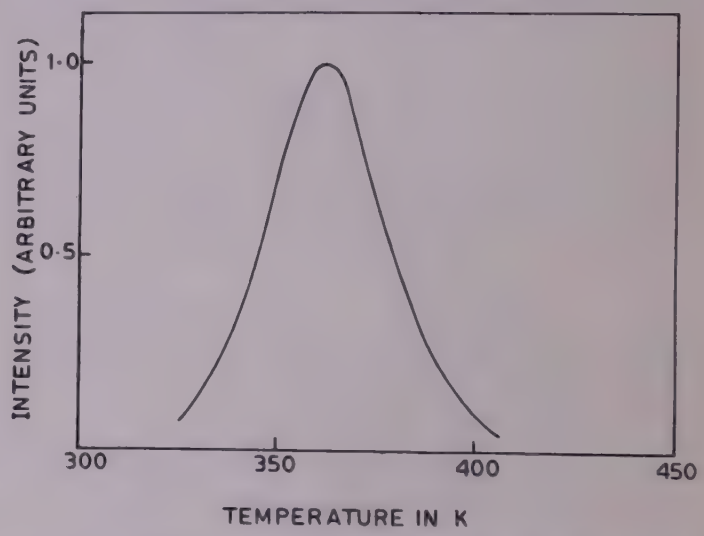

Fig. 7—Thermoluminescence spectrum of polyacrylonitrile

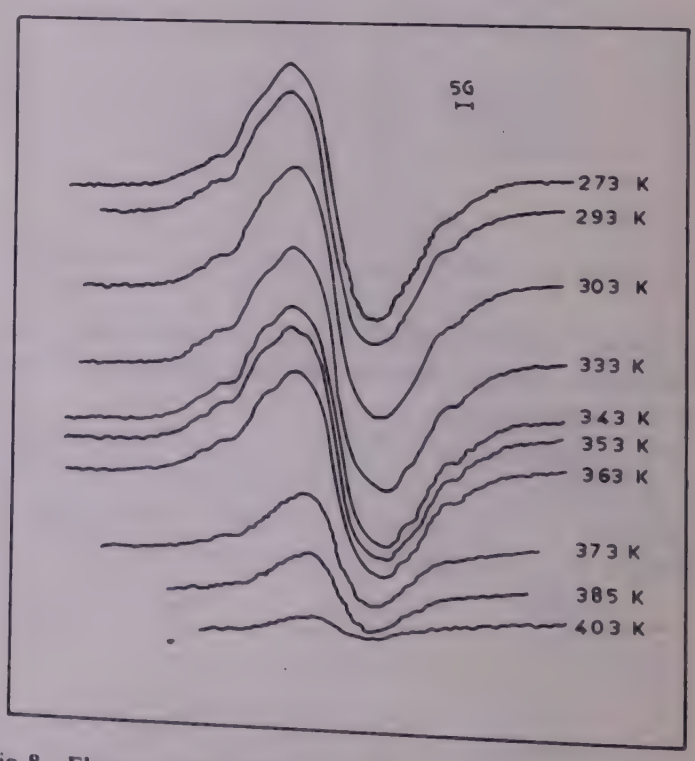

Fig. 8—Electron spin resonance spectrum of PAN at various temperatures

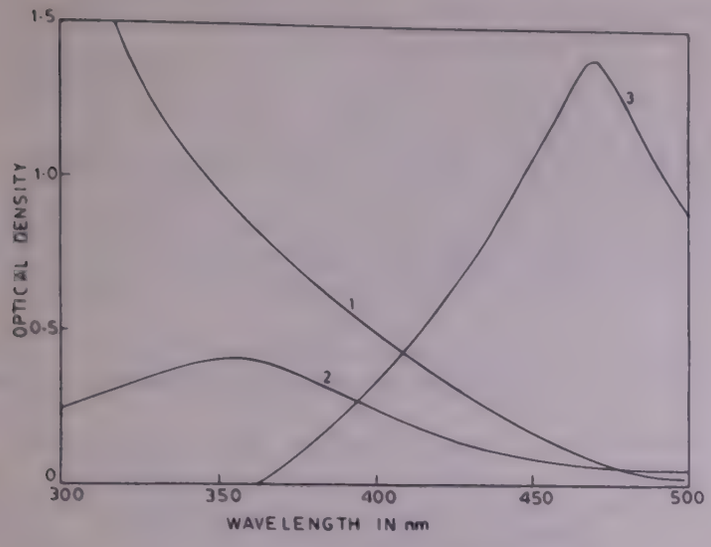

Fig. 9—Optical absorption spectra of PAN

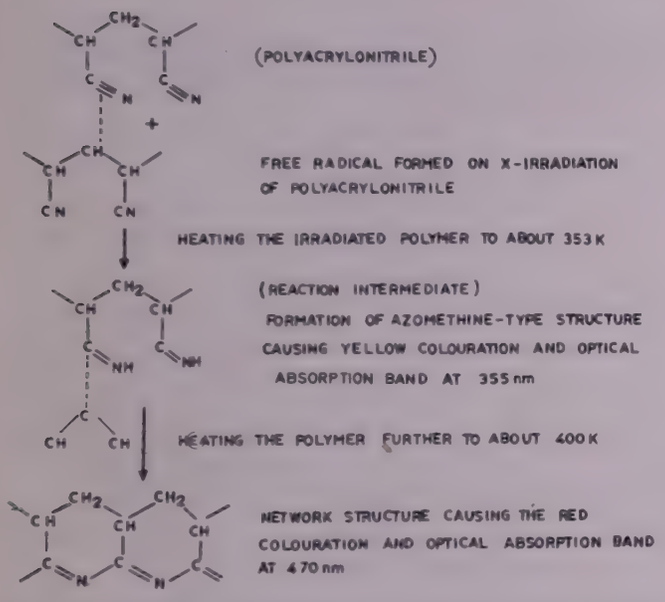
(POLYACRYLONITRILE)
FREE RADICAL FORMED ON X-IRRADIATION OF POLYACRYLONITRILE
HEATING THE IRRADIATED POLYMER TO ABOUT 353 K
(REACTION INTERMEDIATE)
FORMATION OF AZOMETHINE-TYPE STRUCTURE CAUSING YELLOW COLOURATION AND OPTICAL ABSORPTION BAND AT 355 nm
HEATING THE POLYMER FURTHER TO ABOUT 400 K
NETWORK STRUCTURE CAUSING THE RED COLOURATION AND OPTICAL ABSORPTION BAND AT 470 nm

Fig. 10—Mechanism of formation of network structures in PAN

Fig. 9 shows the optical absorption spectra of PAN. Curve 1 shows the spectrum for unirradiated PAN and recorded at RT. Curves 2 and 3 show the spectra for the samples irradiated at RT and heated to 353 K and 403 K respectively. For samples heated to 353 K the optical band is observed at 355 nm, while for that heated to 403 K the band shifted to 470 nm. PAN is colourless to begin with, but when heated to about 373 K, it develops a yellow colour and shows an optical adsorption band at 355 nm. This is identical to the situation obtained when the irradiated samples are heated to about 353 K. Thus the process of colour change, brought about by heating, seems to be hastened by the process of radiation damage. These colour changes are best observed by partially irradiating a sample and the entire sample warmed up. Thus the radical formed on irradiation accelerates the change in colour to yellow. Thermal colouration of PAN was shown by Grassie and Hay[20] to be due to the linking up of adjacent nitrile groups to form conjugated carbon-nitrogen sequences. A mechanism of self-initiation for thermal colouration of PAN has been proposed in which CH groups participate.

The $-CH$ group reacts readily with the unsaturated CN group. The hydrogen atom migrates to the nitrogen and carbon of the nitrile group. Thus the formation of azomethine-type intermolecular cross-link occurs. Thus the free radical decays by initiating and accelerating the formation of network structures and, on further heating, this structure transforms into the structure proposed by Grassie and Hay[20], as shown in Fig. 10.

The simultaneous observance of: (i) a change in the optical density, (ii) the decay of the free radical as observed by ESR and (iii) the appearance of the TL glow peak at 362 K indicates that the species responsible for all the three phenomena is the same.

Polycellulose acetate (*PCA*)—Fig. 11 shows the TL spectra of irradiated PCA. Curves 1, 2 and 3 show the spectra for the samples irradiated in air for 30 min, 1 hr and 2 hr respectively as reported earlier[21]. Five glow peaks have been observed in all the cases, at 136 K, 161 K, 192 K, 340 K and 391 K. The intensity of the glow peaks increase with radiation dose. The glow peaks at 136 K and 161 K are not observed for the samples irradiated in vacuum.

Several ESR experiments have been reported[22-24] on irradiated PCA and the interpretation of these spectra is very much complicated by the fact that very poorly resolved spectra are obtained even for samples which are γ-irradiated. The spectra are unsymmetrical and are considered to be due to the existence of several free radicals.

The glow peaks at 136 K and 161 K are attributed to be due to the detrapping of electrons which are trapped by carbonyl groups formed during the irradiations in air. The glow peak at 192 K may be due to the electrons

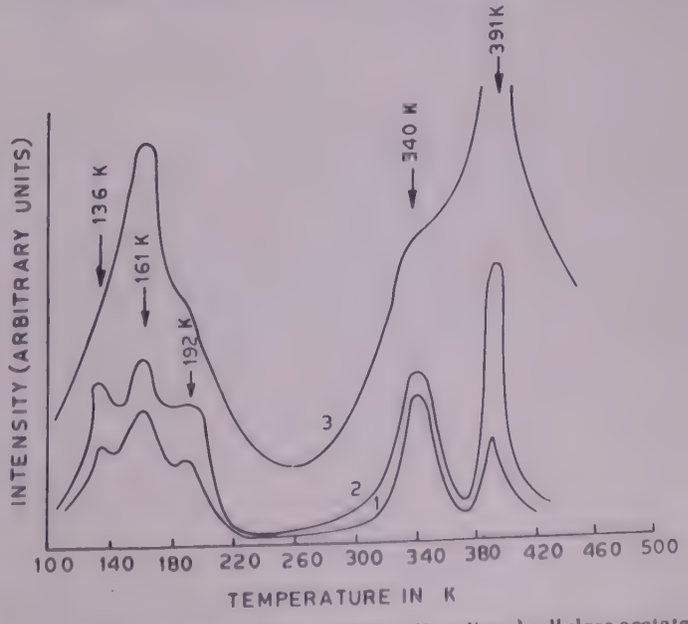

Fig. 11—Thermoluminescence spectra of irradiated cellulose acetate

and or holes/free radicals trapped in molecular chain folds.

Spectral analysis of the glow peaks may yield more information regarding the nature of luminescent centres responsible for the TL glow peaks and the nature of the other radiation damage products.

References

1 Fowler J F, *Proc R Soc London Ser A* (*GB*), **236** (1956) 464.

2 Chapiro A, *J Polym Sci* (*USA*), **34** (1959) 481.

3 Chapiro A, *Radiation chemistry of polymeric systems* (Interscience-John Wiley, New York) 1962.

4 Hedvig P, *J Polym Sci Pt A2* (*USA*), **2** (1964) 407.

5 Stephenson C V, Moses R C & Wilcox W S, *J Polym Sci* (*USA*), **55** (1961) 451.

6 Kusomoto N, Haga Y & Motozoto Y, *Polymer* (*GB*), **16** (1975) 229.

7 Nikitina T S, Zhuravskya E V & Kuzminsky A S, *Effects of ionizing radiations on high polymers* (Gordon & Breach, New York) 1963.

8 Campbell D, *J Polym Sci Macromol Rev* (*USA*), **4** (1970) 91.

9 Radhakrishna S & Ramakrishna Murthy M, *J Polym Sci Polym Phys Ed* (*USA*), **15** (1977) 987.

10 Radhakrishna S & Ramakrishna Murthy M, *J Polym Sci Polym Phys Ed* (*USA*), **15** (1977) 1261.

11 Iwasaki M & Sakai Y, *J Polym Sci A1* (*USA*), **76** (1969) 1937.

12 Michel R E, Chapman F W & Mao T J, *J Polym Sci A1* (*USA*), **5** (1967) 677.

13 Abraham R J & Whiffen D M, *Trans Faraday Soc* (*GB*), **54** (1958) 1291.

14 Ohnishi S, Tanei & Nitta I, *J Chem Phys* (*USA*), **37** (1962) 2402.

15 Tideman G T & Ingalls R B, *J Phys Chem* (*USA*), **71** (1967) 3092.

16 Socs F & Plack J, *J Polym Sci Polym Phys Ed* (*USA*), **13** (1975) 1789.

17 Tomita A, *J Phys Soc Jpn* (*Japan*), **28** (1970) 731.

18 Ramakrishna Murthy M & Radhakrishna S, *Pramana* (*India*), **20** (1983) 85.

19 Hasegewa S & Shimazu T, *Jpn J Appl Phys* (*Japan*), **9** (1970) 958.

20 Grassie N & Hay J N, *J Polym Sci* (*USA*), **56** (1962) 189.

21 Ramakrishna Murthy M, *Proc Conf on Nuclear Physics and Solid State Physics*, (Bhabha Atomic Research Centre, Bombay), **23C** (1980) 379.

22 Arthur J C, Hinojosa O & Tripp Y W, *J Appl Polym Sci* (*USA*), **13** (1969) 1497.

23 Florin R E & Wall C A, *J Polym Sci Pt A1* (*USA*), **1** (1963) 1163.

24 Baugh P J, Hinojosa O & Arthur J C (Jr), *J Appl Polym Sci* (*USA*), **11** (1967) 1139.

Indian Journal of Pure & Applied Physics
Vol. 21, October 1983, pp. 587-591

Parallel Plate Interferometer for the Precise Measurement of Radius of Curvature of a Test Plate & Focal Length of a Lens-System

M V R K MURTY† & R P SHUKLA
Spectroscopy Division, Bhabha Atomic Research Centre,
Bombay 400 085

Received 21 *September* 1982; *revised received* 8 *December* 1982

Measurement of radius of curvature of a test plate by using the parallel plate interferometer is described. The parallel plate interferometer has also been used for locating the cardinal points of an optical lens-system.

1 Introduction

The conventional method for measuring the radius of curvature of a test plate is with a microscope[1]. The precision of measurement depends on how accurately one can focus the reticle on the surface. The depth of focus of the microscope must be very small. However, it is not possible to measure the surface accuracy by this method. The surface measuring interferometer was devised by Munnerlyn[2]. This interferometer is a modification of Twyman-Green interferometer. The Twyman-Green interferometer is affected by vibrations. The parallel plate interferometer[3] was utilized for the measurement of large radius of curvature by Riley and Gusinow[4]. A method for measuring the short and medium radius of curvature as well as the surface accuracy by using the parallel plate interferometer is described in this paper. The interferometer is found to be stable. The same interferometer can also be used for locating the cardinal points of an optical system.

2 Theory

The interferometer devised by Murty[3] is shown schematically in Fig. 1. A laser beam is focussed by means of a microscope objective at the focus of a well-corrected collimating lens. A wedged plate is placed in the path of the collimated beam such that the apex of the wedge is in the horizontal plane. The beam is reflected partly from the front surface and partly from the second surface of the plate and two sheared wavefronts are obtained. The interference pattern is obtained in the common overlapping area. The collimating lens is adjusted to obtain the horizontal straight fringes. For measuring the radius of curvature of the test plate, a focussing lens is placed in the path of a transmitted beam. The surface of test plate is brought to the focus of the lens. The reflected wave is again collimated by the lens and interference is observed due to the sheared wavefronts. The position of the test plate is adjusted very accurately until horizontal straight fringes are obtained. The position of the test plate is noted. The test plate is then moved towards the right in order to focus the laser beam at its centre of curvature. When the focus of the beam and the centre of curvature of the test plate coincides, the horizontal straight fringes are observed. Even slight error in the setting makes the fringes inclined which can be easily detected against a cross wire. The second position of the test plate is noted. The displacement of the test plate between these two positions gives the radius of curvature. The surface accuracy of the test plate can be measured by analysing the shearing interferogram. The procedure for calculating the shape of the wavefront from the shearing pattern is given in Refs 5-10. However, the qualitative estimation of the surface accuracy of the test plate can be done by observing the deviation of the fringes from the ideal linear pattern.

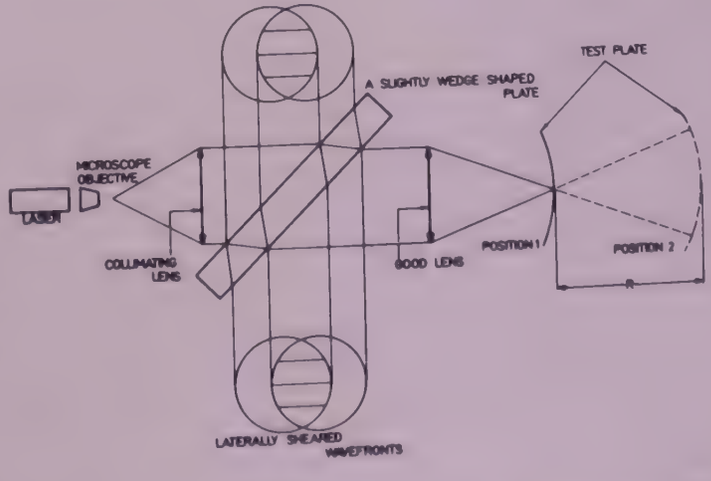

Fig. 1—Schematic diagram of a parallel plate interferometer for measuring the radius of curvature of a concave spherical surface

†Presently with Centro De Investigaciones En Optica, AC, Apartado Postal 948, LEON, GTO, Mexico

Fig. 2 shows the corresponding arrangement for convex surfaces. Since the distance is measured by taking the difference between the two positions, the accuracy in the measurement is high. Fig. 3 shows the lateral shearing interferogram obtained for a concave mirror. The fringes are horizontal at the focus. They are inclined on either side of the focus. The inclination of the fringes indicates the defocussing error. A slight error in detecting this inclination of the fringes introduces the defocussing error which determines the limit on the precision achieved in the measurement. Several observations show that the uncertainty in setting the fringes parallel to the horizontal direction is about 1° which amounts to a precision of a few microns in the radius of curvature measurements depending on the diameter and the focal length of the focussing lens. The limited accuracy of the parallel plate interformeter is described in the appendix of the paper.

3 Method of Finding the Orientation of the Fringes Obtained With a Well Collimated Beam

It is necessary to know the orientation of the straight fringes obtained with a well collimated beam. If the shear is in the horizontal direction and the apex of the wedge is horizontal, then the fringes obtained for a well collimated beam are horizontal, slight decollimation makes the fringes inclined to the horizontal direction.

Fig. 4 shows the schematic diagram for setting the apex of the wedge in the horizontal direction. A thin beam splitter is inserted between the microscope objective and the collimating lens in order to convert the shearing interferometer into a Fizeau interferometer. The slightly decollimated beam is incident normally on the wedged plate. The Fizeau fringes are seen on the screen. A horizontal wire placed between beam splitter and the screen serves as a reference line for setting the fringes. The wedged plate is rotated in its own plane until the Fizeau fringes are set parallel to the reference wire. This sets the apex of the wedge in the horizontal direction. The beam splitter is now removed from the path of the beam and the wedged plate is used as a shearing interferometer.

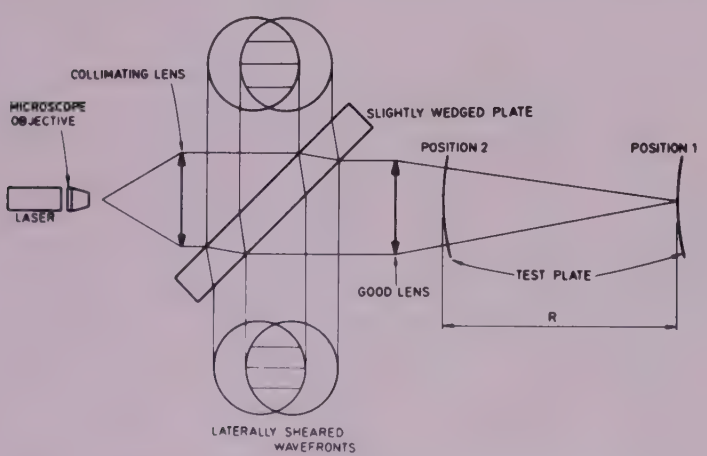

Fig. 2—Schematic diagram of a parallel plate interferometer for measuring the radius of curvature of convex surface

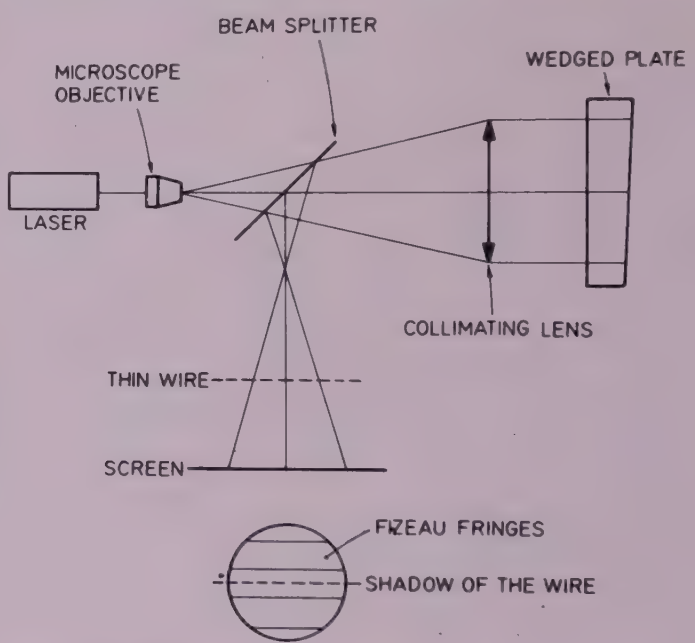

Fig. 4—Schematic arrangement of Fizeau interferometer for setting the apex of the wedged plate in the horizontal direction

Fig. 3 Interferogram obtained for a concave mirror of radius of curvature 50 mm in the set-up shown in Fig. 1. [(a) Inside the focus, (b) at the focus and (c) outside the focus. Small amount of defocussing is indicated by the inclination of the fringes. Optical elements used are: lenses of aperture 40 mm and focal length 250 mm, wedged plate of angle 16.4 sec of an arc and thickness 41.31 mm, refractive index of the wedged plate 1.51. Shear $S = 7.6$ mm for angle of incidence of 8°5'.]

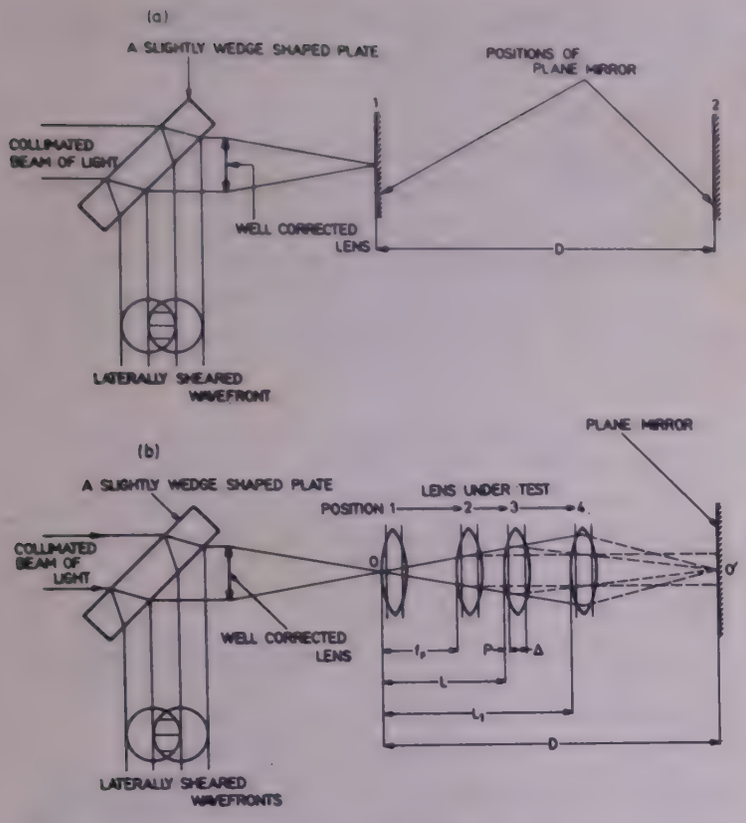

Fig. 5—Schematic diagram showing a parallel plate interferometer in two steps (a) and (b) for location of the cardinal points of lens system.

Inclined fringes indicate the decollimation of the beam. Exact collimation is obtained by setting the fringes parallel to the horizontal reference line with the proper focussing of the microscope objective in relation to the collimating lens.

4 Location of the Cardinal Points of a Lens System

It is necessary to locate exactly the cardinal points of a lens-system to characterize the paraxial properties of the lens. The focal points and principal points are known as the cardinal points. For a system with the same optical medium (usually air) in image space as in object space, the nodal points coincide with the principal points. Several methods for measuring the focal length of an optical system were described in Ref. 11. The parallel plate interferometer can also be used for the location of cardinal points very precisely. Figs. 5(a) and 5(b) show the schematic arrangement for the determination of effective focal length (efl) and front focal length (ffl). The first step is to bring the plane mirror at the focus O by setting the fringes horizontal and noting down the position of the mirror. The mirror is now displaced to a convenient position depending on the focal length of the lens under test. The position O′ of the mirror is noted. The difference between these two positions gives a value of D. The second step is to place the lens under test at the focus O and the position is noted. The lens is now moved to a position 2 so that the focus of the beam coincides with the focal point of the lens. The distance between the position 1 and the position 2 gives the front focal length. Third step is to move the lens to a position 3 such that the image of the point O is focused on the plane mirror at O′. The distance between the position 3 and the position 1 is denoted by L. Last step is to move the lens to a position 4 such that the points O and O′ are again conjugate points. The distance between the position 4 and the position 1 is denoted by L_1. The cardinal points can be located by solving the following equation:

$$P^2 + 2f_F P + f_F(L_1 + L) - LL_1 = 0 \quad \ldots (1)$$

where P is the distance of the first principal point from the front surface and f_F the front focal length.

From Eq. (1), we have

$$P = -f_F \pm \{f_F^2 + LL_1 - f_F(L + L_1)\}^{1/2} \quad \ldots (2)$$

The distance between the principal points is given by

$$\Delta = D - (L_1 + L + 2P) \quad \ldots (3)$$

The effective focal length of the lens is then calculated from the following equation:

$$\text{efl} = f_F + P = \{(L - f_F)(L_1 - f_F)\}^{1/2} \quad \ldots (4)$$

The distance P is considered to be positive when the principal point lies on the right hand side of the front surface. When the distance P is negative, front focal length is greater than the effective focal length. By measuring the distances L, L_1 and f_F the position of the cardinal points can be computed from Eqs (2) to (4). The method described here is applicable only for positive (i.e. converging) lenses.

5 Experimental Details and Results

We have used the telescope doublets of focal length 250 mm and aperture 50 mm as collimating and focussing lenses. A wedged plate of angle 4 sec and thickness of about 25 mm was used as a shearing element. The angle of incidence was kept about 45°. The test plate was mounted on the carriage of the comparator which can yield a precision of 1 μm. It is advantageous to coat the test plate with aluminium for achieving the fringes of brighter illumination. Even uncoated surface provides the fringes of sufficient visual illumination when a He-Ne laser giving the power output of 2.5 mW is used for the work. Several observations were taken for the measurement of radius of curvature of the test plate and we found the radius of curvature to be 50.265 mm $\pm$ 6 μm.

Using the same set-up and the procedure described above we have measured the efl, back focal length (bfl) and ffl of an achromatic doublet of aperture 10 mm and we found that efl = 50.2 $\pm$ 0.2 mm, bfl = 50.10 mm $\pm$ 30 μm and ffl = 46.850 $\pm$ 12 μm. We define here ffl as

the distance between the focal point and the plane surface of the doublet. In this case, the plane surface of the doublet is facing towards the point source placed at the focal point, and therefore, the spherical aberration is minimal. We achieve a better degree of precision in the measurement of ffl due to the presence of very small amount of spherical aberration. When the strongly curved surface is placed towards the point source in order to measure the bfl, larger amount of spherical aberration is introduced. This reduces the setting accuracy. In the measurement of other parameters such as L and L_1, the setting accuracy is also decreased due to the presence of a comparatively larger amount of spherical aberration which ultimately introduces a comparatively larger amount of error in the computation of efl. We have computed the efl from one set of measured parameters ffl, L and L_1 and also from the other set of measured parameters bfl, L and L_1. We have noticed that the computed value for efl from the parameters ffl, L and L_1, is a little greater than the value computed from the other set of parameters. This may be due to the different amounts of errors in the setting accuracy.

It may be mentioned here that when the outer surfaces of the lens-system are coated with an anti-reflection coating, it is difficult to get shearing interference pattern of sufficient visual illumination with a low power laser due to the poor reflectivity of the coated surface. However, the fringes may be obtained due to the residual reflectivity of the anti-reflecting coated surface if high power laser is used.

6 Conclusions

It is possible to measure the radius of curvature of a test surface and the ffl of a lens-system with an accuracy of a few microns using the parallel plate or slightly wedged plate interferometer. It is also possible to measure the efl of a lens system but the accuracy of the measurement is reduced to some extent due to the presence of spherical aberration.

Acknowledgement

The authors are indebted to Shri S L N G Krishnamachari, Head, Spectroscopy Division, for his suggestions and encouragement throughout the course of this work.

References

1 Johnson B K, *Optics and optical instruments* (Dover Publications, New York), 1960, 179.
2 Munnerlyn C R, *Opt Eng (USA)*, **11** (1972) 38.
3 Murty M V R K, *Appl Opt (USA)*, **3** (1964) 531.
4 Riley M E & Gusinow M A, *Appl Opt (USA)*, **16** (1977) 2753.
5 Murty M V R K & Malacara-Hernandez D, *Jpn J Appl Phys (Japan)*, **4** (1965) 106.
6 Dutton D, Cornejo A & Latta M, *Appl Opt (USA)*, **7** (1968) 125.
7 Saunders J B, *J Res Natl Bur Stand Sect B (USA)*, **65** (1961) 239.
8 Nyssonen D & Jerke J M, *Appl Opt (USA)*, **12** (1973) 2061.
9 Rimmer M P, *Appl Opt (USA)*, **13** (1974) 623.
10 Rimmer M P & Wyant J C, *Appl Opt (USA)*, **14** (1975) 142.
11 Johnson BK, *Optics and optical instruments* (Dover Publications, New York), 1960, Ch 11, p. 21.

Appendix

Setting Accuracy

The limiting accuracy in the measurement of radius of curvature is determined by the accuracy with which the fringes can be set parallel to the direction of shear when the optical system is being set up for achieving a high degree of beam collimation using a wedged plate. In the case when a parallel plate is used for achieving a high degree of collimation, the limiting accuracy is determined by the ability to set the fringe-free field.

Let us first consider the parallel plate which is being used for checking the collimation of the laser beam. For achieving a perfect collimation, the fringe of infinite width should be set. But because of the limited aperture of the optical system it is just possible to differentiate between the fringe of infinite width and the fringe of width equal to the overlapping aperture of the sheared wavefronts. This limits the setting accuracy of the interferometer. In order to derive the expression for the shift of focus due to this uncertainty in setting, we displace the point source from the actual focal point of the collimating lens of aperture D by an amount δl as shown in Fig. A1. The emerging wavefront has a radius of curvature given by

$$r = \frac{Sd}{\lambda} \qquad \ldots (A1)$$

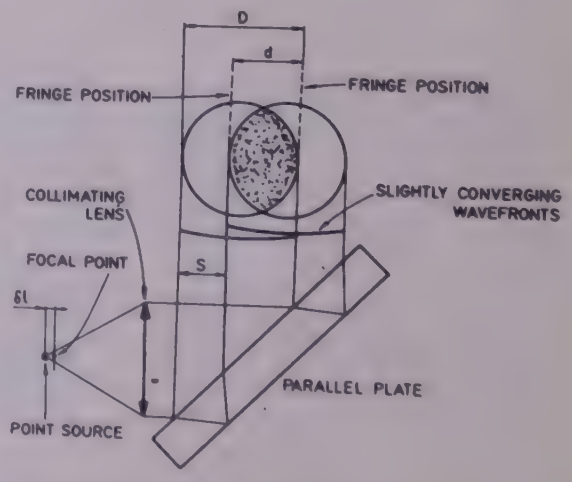

Fig. A1—Schematic diagram showing the parallel plate interferometer [The point source is slightly defocussed with reference to the focal point of the collimating lens.]

where d = fringe spacing, λ = wavelength and S = lateral shear given by

$$S = \frac{t \sin 2i}{\sqrt{(N^2 - \sin^2 i)}}$$

where t = plate thickness, N = refractive index of glass, and i = angle of incidence.

Taking fringe spacing $d = (D - S)$ = length of the overlapping region, we have

$$r = \frac{S(D-S)}{\lambda} \qquad \text{... (A2)}$$

Using thin lens formula for converging lens we write

$$\frac{1}{f + \delta l} \pm \frac{1}{r} = \frac{1}{f} \qquad \text{... (A3)}$$

where f = focal length of the collimating lens and the plus sign is used for converging focus and the negative sign for diverging focus.

From Eqs (A2) and (A3), we get shift of focus as

$$\delta l = \frac{f^2}{r} = \frac{f^2}{S(D-S)} \qquad \text{... (A4)}$$

By choosing shear S such that $(D - S) = S$, we have $\delta l_{\min} = 4\lambda f^{*2}$ as the limiting accuracy

where $f^* = \frac{f}{D} = f$−number of the optical system.

For a typical example, we get $\delta l_{\min} = 2.5\ \mu$m for $f^* = 1$ and $\lambda = 0.6328\ \mu$m.

In the case of a wedge shaped plate, the radius of curvature of the emerging wavefront is given by:

$$r = \frac{SD}{\lambda \sin \varphi} \qquad \text{... (A5)}$$

where φ = angle of rotation of the fringes with respect to the direction of shear as shown in Fig. A2.

In order to set a limit on the accuracy, we assume that the minimum angle of rotation ($\varphi_{\min}$) which can be detected is given by

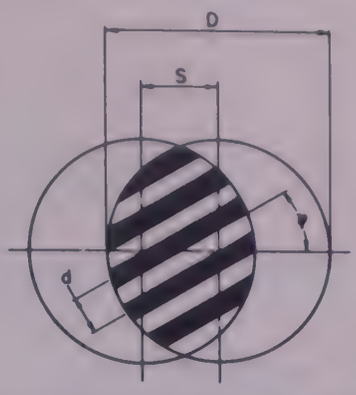

Fig. A2—Schematic representation of interference pattern resulting from a wedged plate interferometer. The tilt of the fringes with respect to the direction of shear shows the decollimation of the beam.

$$\varphi_{\min} \approx \frac{\delta d}{(D-S)} \qquad \text{... (A6)}$$

where δd = uncertainty in the measurement of fringe spacing. Hence under this assumption we get shift of focus as

$$\delta l = \frac{f^2 \lambda \delta d}{Sd(D-S)} \qquad \text{... (A7)}$$

For a proper choice of shear such that $D - S = S$, we have the limiting accuracy in the measurement as

$$\delta l = 4\lambda f^{*2} \left(\frac{\delta d}{d}\right) \qquad \text{... (A8)}$$

For $\cos^2$-type of fringes $\frac{\delta d}{d} \approx \frac{1}{10}$ and we get

$$\delta l \approx 0.4\lambda f^{*2} \qquad \text{... (A9)}$$

For a typical example, $\delta l = 0.25\ \mu$m for $f^* = 1$ taking $\lambda = 0.6328\ \mu$m.

We conclude that the setting accuracy achieved in the wedged plate interferometer is higher than the setting accuracy achieved in the parallel plate interferometer.

Indian Journal of Pure & Applied Physics
Vol. 21, October 1983, pp. 592-594

Design of Dipping Refractometer with Indian Optical Glasses

B N GUPTA & A K GARG

Instrument Design Development Centre, Indian Institute of Technology, New Delhi 110016

Received 10 *August* 1982; *revised received* 17 *August* 1983

Design of a highly sensitive dipping or immersion refractometer with Indian optical glasses utilizing the critical angle principle is presented. This refractometer is capable of measuring the refractive index up to 2×10^{-5} units of refractive index. The accuracy of measurement is found to be increased by choosing a prism of the material whose refractive index is slightly more than the highest value of the refractive index to be measured. To increase the accuracy further, the total range of refractive indices to be measured has been sub-divided and a different prism with different material and angles has been used for each subrange. The calculated tolerance of prism angles is found to be ~ 10 sec. It is suggested that to economize the manufacturing cost, instead of making the prism of required high angular tolerance to suit a particular scale, the scale should be calibrated for each set of prisms.

1 Introduction

Refractometry is one of the old branches of optics. Now in the twentieth century refractometry has reached industrial maturity, first in production control laboratories and more recently in the plant itself, with fully automatic refractometers being used as discriminators in control loop systems. Measurement of refractive index is important in the optical industry to check the suitability of materials intended for components of lenses etc. It can be used for identification (gems, stones etc.) and as a method of analysis (e.g. to control a component in a gaseous mixture). The ordinary direct methods of measuring the refractive indices of glass specimens cannot be applied when one wishes to determine the refractive properties of a specimen of glass which is unpolished or is in the form of a lens or is very small. In such cases the unusual method[1] adopted for measuring the refractive index for any given wavelength is to immerse the specimen in a transparent liquid having approximately the same refractive index, and to vary the concentration of the liquid until the refractive indices of liquid and specimen for that wavelength are the same. In such situations dipping refractometer may be used to measure the refractive index of the liquid, and thereby of the solid specimen. In the present paper, the design of a highly sensitive immersion refractometer is discussed, which is an important tool in various quality control, clinical and research laboratories.

2 Description

The immersion refractometer is a narrow-range, high-accuracy instrument for the refractometry of liquids available in fairly large quantities. The measured values of refractive indices are reliable to a few units in the fifth decimal place because a particular prism is being used only for a narrow range. A set of seven prisms has been made experimentally to cover the fairly large range in which the refractive indices of most of the liquids fall.

The optical layout of the immersion refractometer is shown in Fig. 1. The rays of light emerging from a prism in contact with a substance may be formed into a well defined shadow edge. The instrument can be provided with an evenly divided, arbitrary scale, capable of accurate subdivision, and calibration tables expressing the scale reading in terms of refractive index. The use of an arbitrary scale also permits the attachment of different prisms, each with its individual table, covering different ranges of the refractive index.

3 Theory

The instrument employs the critical angle effect marked by a demarcation line between light and dark portions of the telescope field as shown in Fig. 2(a).

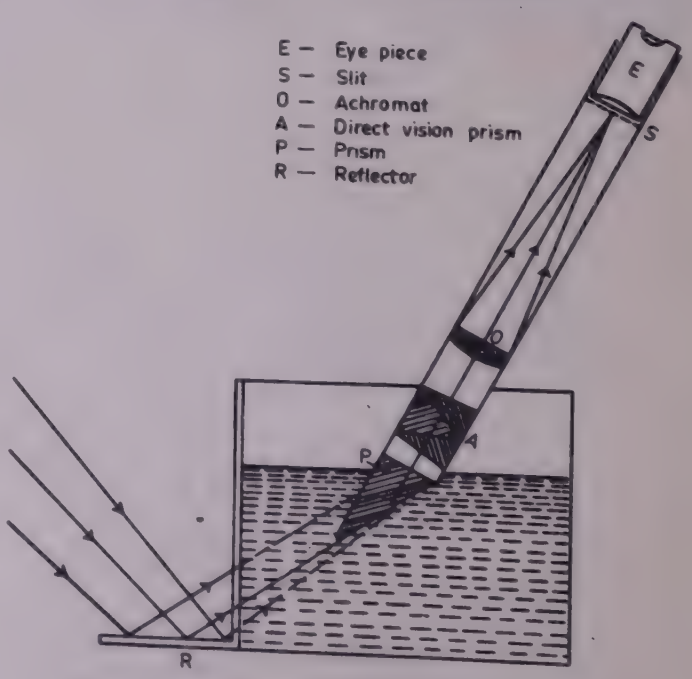

Fig. 1—Optical system of immersion refractometer

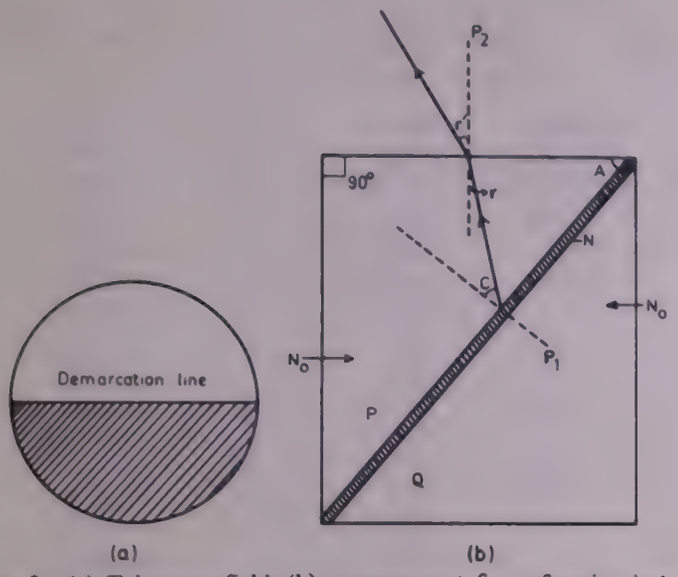

Fig. 2—(a) Telescope field; (b) arrangement for refractive index measurement

The means by which this effect is produced is discussed in many good textbooks[2-5] on optics. Fig. 2(b) shows the arrangement employed for the measurement of the refractive index of a liquid. A ray of light striking P at grazing incidence emerges at an angle r' and the usual demarcation line is viewed by means of the telescope. If N is the refractive index of the liquid, then it can be shown that

$$N = N_0 \sin [A - \sin^{-1} (\sin r'/N_0)] \quad \ldots (1)$$

where N_0 is the refractive index of the prism material, r' the angle of emergence, and A the angle of the particular prism such that r' is zero for mean refractive index to be measured by that particular prism.

Using Eq. (1), we can find refractive indices of the liquids by measuring the position of demarcation lines on the graticule in the focal plane of the objective for fixed values of N_0 and A. The position of demarcation line on the graticule is related with the emergence angle. While designing the prisms, care has been taken such that the emergent ray for the mean value of refractive indices to be measured by that prism emerges at 90° to the last surface of the prism (as shown in Fig. 1). The material of each prism is selected from the CGCRI glasses. The refractive index of each prism material is taken slightly more than the maximum value of the refractive index to be measured with the help of that prism.

4 Changing of Prisms

The prisms can easily be interchanged by removing the screws holding the flange of the nose-piece to the end of the telescope barrel. After interchanging the prism the standardization of the instrument must be done against a substance of known refractive index. The refractive indices of the prism material and angles of the prism are given in Table 1.

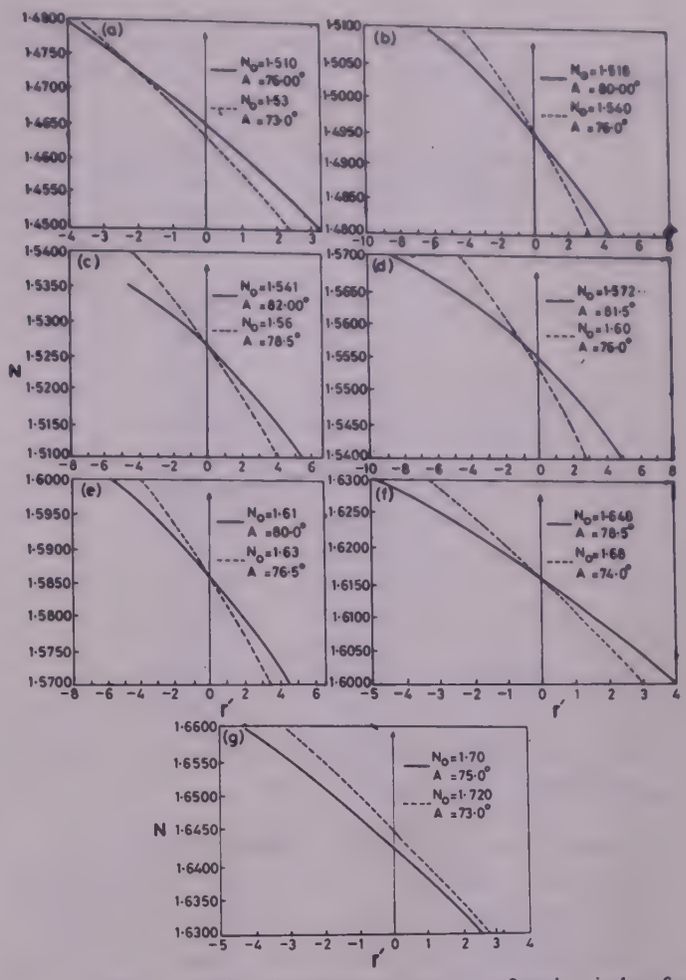

Fig. 3—Plot of angle of emergence versus refractive index for various values of N_0 and A

Table 1—Refractive Indices of Prism Material to be Used for Different Ranges of Index Measurement along with Angle of Prism

Refractive index ranges	Refractive index of prism material	Angle of the prism (deg)
1.450-1.480	1.510	76.0
1.480-1.510	1.518	80.0
1.510-1.540	1.541	82.0
1.540-1.570	1.572	81.5
1.570-1.600	1.610	80.0
1.600-1.630	1.648	78.5
1.630-1.660	1.700	75.0

5 Temperature Control

The importance of temperature cannot be overstressed on an instrument of this nature. If the refractometer is being used on comparative readings, it is important that all samples should be at the same temperature, and not necessarily at the standard temperature of 20°C, for which the tables are corrected. For most purposes it is sufficient to control temperature to ±0.1°C. For repetitive sampling at controlled temperature, it is recommended that the composite unit comprising thermostatic bath, lid with built-in source and beaker tray be used. The bath cover

Table 2—Total Angle of Emergence for Prisms of Different Refractive Indices Suitable for Measurement of Refractive Indices in Different Ranges

Range of refractive index	Refractive indices of the prism material N	Total angle of emergence (deg)
1.450-1.480	1.510	7.19595
	1.530	5.99970
1.480-1.510	1.518	10.57438
	1.540	7.16627
1.510-1.540	1.541	14.57983
	1.560	8.36417
1.540-1.570	1.572	13.67924
	1.600	7.40509
1.570-1.600	1.610	10.32346
	1.630	7.47296
1.600-1.630	1.648	8.87885
	1.680	6.28124
1.630-1.660	1.700	6.87794
	1.720	5.91412

carries the temperature controller and circulator, together with a strip light.

6 Determination of Refractive Index of Solids

The solids which can be polished are applied in the same manner as the test piece using a contact liquid. A surface of a solid sample must be prepared, polished as flat as possible and placed on the prism surface, with the help of the contact liquid. Monobromonaphthalene whose refractive index is 1.65 is generally used as contact liquid. The refractive index of the contact liquid must be higher than that of the solid to be measured. If the solid has an index higher than 1.65, methylene iodide can be employed as a contact liquid in place of monobromonaphthalene which can only be used up to this limit.

7 Results and Discussion

With the help of Eq. (1) we have calculated the angles of emergence for different values of refractive indices. Figs 3 [(a)-(g)] present the variation in angle of emergence with refractive index for seven different ranges of refractive index. Each plot shows the variation in angles of emergence for two prisms of different materials. It is clear from the plots that for a particular range, the angle of emergence is more for prisms having a material of lower refractive index. This fact is further supported by the data given in Table 2, which presents the total angle of emergence for each range and for different prism materials.

Table 3 shows the values of angles of emergence for two different prism angles of the same material. It also gives the difference in angle of emergence for the 5 $\times 10^{-4}$ units change in refractive index. This instrument is accurate up to 2×10^{-5} units of refractive index. So after calculating error in the angle of

Table 3—Values of Angles of Emergence for Two Different Angles of Prism of the Same Material

Refractive index of the material	Angle of prism (deg)	Refractive index of the prism	Angle of emergence (deg)
1.4500	76.0	1.510	3.37690
	76.5		4.13279
1.4505	76.0	1.510	3.27412
	76.5		4.02997
1.4800	80.0	1.518	4.37138
	80.5		5.13186
1.4805	80.0	1.518	4.24200
	80.5		5.00239
1.5100	82.0	1.541	5.46567
	82.5		6.23849
1.5105	82.0	1.541	5.32104
	82.5		6.09374
1.5400	81.5	1.572	4.89544
	82.0		5.68352
1.5405	81.5	1.572	4.75201
	82.0		5.53997
1.5700	80.0	1.610	4.55846
	80.5		5.36531
1.5705	80.0	1.610	4.42860
	80.5		5.23534
1.6000	78.5	1.648	3.94580
	79.0		4.77129
1.6005	78.5	1.648	3.82591
	79.0		4.65132

emergence, which can be tolerated for an accuracy of 2×10^{-5} units in refractive index, the tolerance error in prism angles can be calculated which is found to be ~ 10 sec.

It is therefore suggested that the material of the prism chosen should have a refractive index only slightly more than the highest value of the refractive index to be measured, because, in that case angle of emergence will be more and hence also the accuracy in measurement. For effecting a reduction in the cost of manufacturing the prism, it is suggested to calibrate the scale for each set of prisms rather than making the prism of required high angular tolerances to suit a particular scale.

Acknowledgement

The authors are thankful to Prof. R.S. Sirohi, Indian Institute of Technology, Madras for his helpful discussions and suggestions.

References

1 Glazebrook R, *Dictionary of applied physics*, Vol. IV (MacMillan Co., London) 1950.

2 Born M & Wolf E, *Principles of optics* (Pergamon Press, London) 1970.

3 Longhurst R S, *Geometrical and physical optics* (Longmans, London) 1967.

4 Kingslake R, *Applied optics and optical engineering*, Vol. IV (Academic Press, New York) 1967.

5 Smith C J, *A degree physics* (Edward Arnold Ltd., London) 1960.

Indian Journal of Pure & Applied Physics
Vol. 21, October 1983, pp. 595-598

Thermal Emission Spectrum of NiCl Molecule in Violet Region

R GOPAL* & M M JOSHI
Saha Spectroscopy Laboratory, Physics Department, University of Allahabad, Allahabad 211 002

Received 30 *November* 1981; *revised received* 1 *June* 1983

Thermal emission spectrum of NiCl molecule in the region λ4230-3990 Å has revealed the existence of 52 double headed and 14 single headed bands. Single headed bands have been attributed to system $K \rightarrow X$ while double headed bands have been classified into two systems $J \rightarrow X$ and $L \rightarrow X$. Self-reversal phenomenon observed in some of the bands indicates that the lower state involved in these transitions is the ground state of NiCl with the separation 484 cm^{-1} associated with its components. The vibrational constants for 12 electronic states so far studied in thermal emission have also been summarized.

1 Introduction

Several workers[1-5] have investigated the spectrum of diatomic nickel chloride molecule by using various discharge techniques. Recently some[6-8] have reported 9 systems belonging to NiCl in the thermal emission spectrum (5555-4230 Å) emanating from the nickel chloride heated in the Saha furnance. The thermal excitation technique produced the spectrum which was almost free from the numerous atomic lines whose presence otherwise makes the vibrational analysis quite difficult. The present paper reports our findings regarding the thermal emission spectrum attributed to NiCl in the violet region.

2 Experimental Procedure

A small quantity of anhydrous nickel chloride of high purity mixed with spec-pure nickel powder was vaporized to a temperature of about 2400°C in the graphite tube of the high temperature vacuum furnace of this laboratory. Well-defined red-degraded bands lying in the region λ4230-3990 Å were photographed on Ilford R-40 panchromatic plates using a Hilger E-492 spectrograph in 5 min. Measurements were made on CZ Abbe comparator with a least count of 0.0001 mm.

3 Results and Discussion

Thermal emission spectrum of NiCl in the region λ4230-3990 Å has revealed the existence of 52 double headed and 14 single headed red-degraded bands. Single headed bands have been assigned to system $K \rightarrow X$ while the double headed bands have been classified into six sub-systems, viz. $J_1 \rightarrow X_2$, $J_1 \rightarrow X_1$, $J_2 \rightarrow X_1$, $L_1 \rightarrow X_2$, $L_2 \rightarrow X_2$ and $L_1 \rightarrow X_1$. All the 23 bandheads attributed to systems A_1, A_2 and A_3 by Reddy and Rao[2] have been satisfactorily re-assigned in the present analysis. In system $J \rightarrow X$, Q heads are found to be stronger than the R heads, while it is just the reverse for the system $L \rightarrow X$.

Self-reversal phenomenon has been observed in (0,0) and (1,1) bands of sub-systems $J_1 \rightarrow X_1$, $K \rightarrow X_1$ and $L_1 \rightarrow X_1$ and in (0,0), (1,1) and (2,2) bands of sub-systems $J_2 \rightarrow X_1$, $L_1 \rightarrow X_2$ and $L_2 \rightarrow X_2$, as well. Fig. 1 clearly depicts the systems $L \rightarrow X$, $K \rightarrow X$, $J \rightarrow X$ and $I \rightarrow X$ (previously reported as system $B \rightarrow X$ by one of the authors[7]).

Table 1 presents the vibrational constants determined by the authors for the sub-systems under reference. In Tables 2 and 3, the bandhead data, visual estimates of intensities along with their quantum assignments are given.

The vibrational constants for the lower state obtained in present case are the same as reported by us[6-8] for the lower state involved in various band systems as well as those reported by other previous workers[2-4] for the lower states involved in a few of the systems studied by them. The presence of two pairs of band sub-systems $J_1 \rightarrow X_1$ and $J_1 \rightarrow X_2$, and $L_1 \rightarrow X_1$ and $L_1 \rightarrow X_2$ indicates that an interval of about 484 cm^{-1} is associated with the lower state involved in these systems, as has already been reported for systems

Table 1—Vibrational Constants for Various Band Sub-systems of NiCl Molecule

	$\nu_{0,0}$ cm^{-1}	ω_e'	$\omega_e'x_e'$	ω_e''	$\omega_e''x_e''$	No of Bands
$J_1 \rightarrow X_2$	23733 *R* 23728 *Q*	412.6	2.30	434.0	1.80	5
$J_1 \rightarrow X_1$	24216 *R* 24209 *Q*	412.0	2.50	427.0	1.90	9
$J_2 \rightarrow X_1$	24417 *R* 24412 *Q*	398.0	1.75	427.0	1.90	10
$K \rightarrow X_1$	24495	409.0	1.75	427.0	1.90	14
$L_1 \rightarrow X_2$	24131 *R* 24126 *Q*	413.0	2.20	433.4	1.90	3
$L_2 \rightarrow X_2$	24333 *R* 24329 *Q*	408.0	2.00	434.0	1.80	14
$L_1 \rightarrow X_1$	24615 *R* 24609 *Q*	412.0	2.40	427.0	1.90	11

*Present address: Physics Department, Janta College, Bakewar, Etawah 206 124

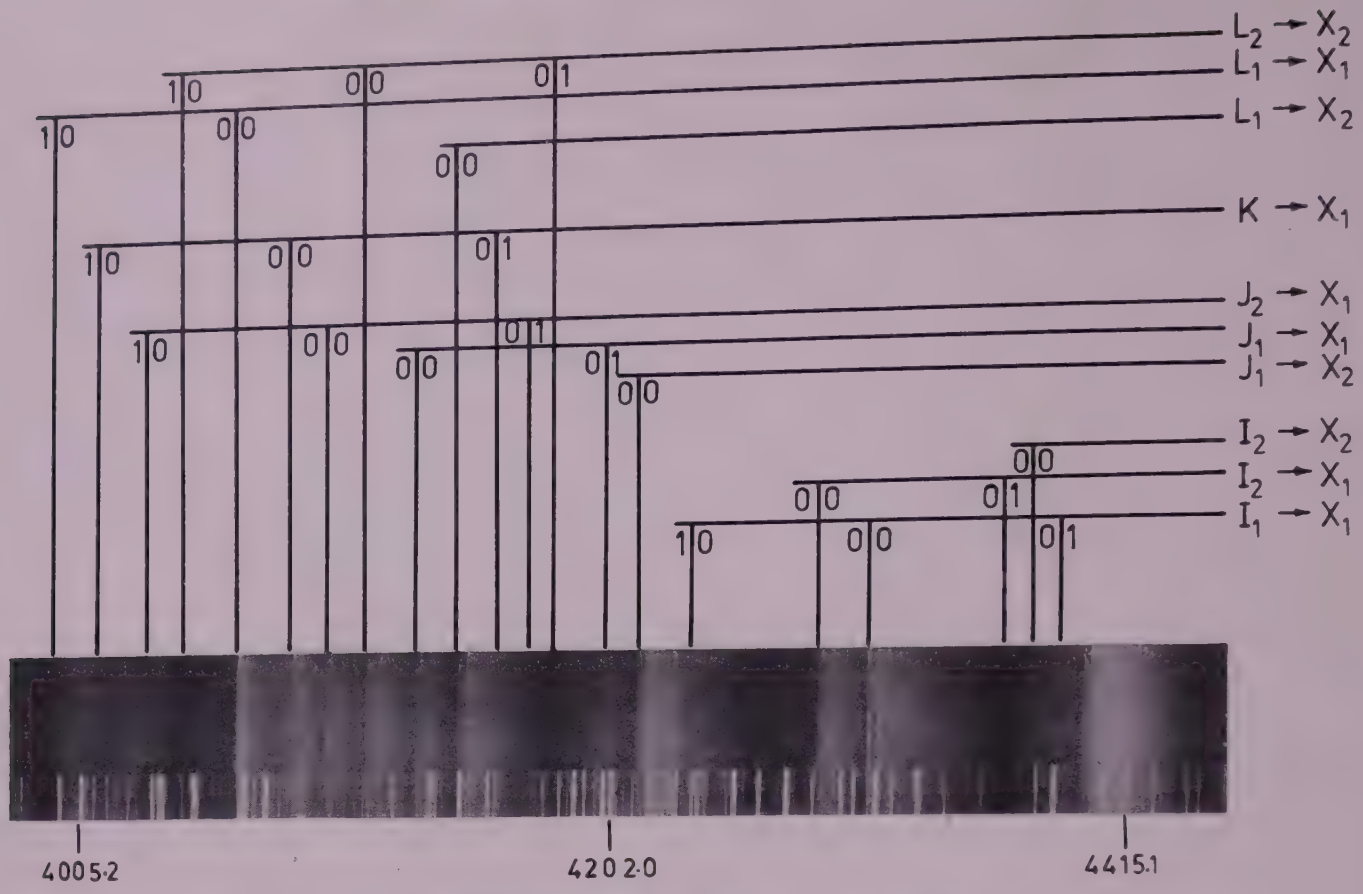

Fig. 1—Band systems of NiCl molecule in thermal emission

$C \rightarrow X$, $D \rightarrow X$ and $I \rightarrow X$. Since in thermal emission, the chances of observing transitions involving the ground state are higher, it is reasonable to assume that the lower state involved in these systems is the ground state with an interval of 484 cm^{-1} associated with its components.

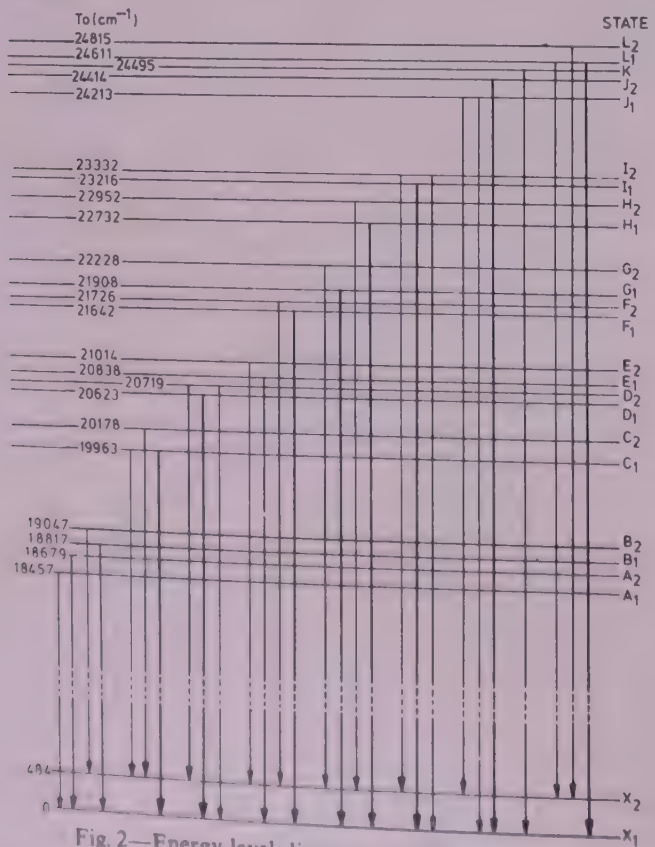

Fig. 2—Energy level diagram of NiCl molecule

It is noteworthy that the self-reversal phenomenon has been observed in few bands attributed to $\Delta v = 0$ sequence of the sub-systems $L_1 \rightarrow X_1$, $L_2 \rightarrow X_2$, $L_1 \rightarrow X_2$, $J_2 \rightarrow X_1$, $J_1 \rightarrow X_1$ and $K \rightarrow X_1$. Hence all these sub-systems must arise from the ground state. This then, confirms that the lower state involved in all these transitions is the ground state. As already stated, the separation 484 cm^{-1} has been found to be associated with the lower state components of the $L \rightarrow X$ transition. Hence one can safely conclude that the lower state involved in all these transitions is the ground state of NiCl and a separation of 484 cm^{-1} is associated with the components of the ground state.

The ground state of the NiCl molecule has been found to be a $^2\Delta$ by Rao and Rao[4] as well as by the present authors[6,7] and thus the probable transitions responsible for NiCl spectra are $^2\Phi - {}^2\Delta$, $^2\Delta - {}^2\Delta$ and $^2\Pi - {}^2\Delta$. In a $^2\Pi - {}^2\Delta$ transition, the Q heads are expected to be stronger than the R heads which is found in the $J \rightarrow X$ system. The R heads have been found to be stronger than the Q heads in the system $L \rightarrow X$ which is expected in $^2\Phi - {}^2\Delta$ transition. However, the rotational analysis is needed to fully justify these transitions.

A tentative energy level diagram representing the transitions of various band systems[6-8] is presented in Fig. 2. The ground state in the energy level scheme is denoted by X_1 or X_2 while the excited states are denoted by $A, B, C, D, E, F, G, H, I, J, K$ and L in order of increasing energy while relative intensity of band

Table 2—Bandhead Data of $J \rightarrow X$ and $K \rightarrow X$ Systems of NiCl

ν_{vac} cm^{-1}	Int.	(v', v'')	ν_{vac} cm^{-1}	Int.	(v', v'')
	$J_1 \rightarrow X_2$			$J_1 \rightarrow X_2$	
23733	5	0,0 R^+	24200	3	1,1 R^+
23728	6	0,0 Q	24193	4	1,1 Q
23712	4	1,1 R^+	24182	2	2,2 R
23706	5	1,1 Q	24176	3	2,2 Q
23688	3	2,2 R	24164	1	3,3 R
23683	4	2,2 Q	24157	2	3,3 Q
23664	2	3,3 R	24142	1	4,4 R
23658	2	3,3 Q	24135	1	4,4 Q
23639	1	4,4 R	23793	2	0,1 R
23634	1	4,4 Q	23786	3	0,1 Q
	$J_2 \rightarrow X_1$		23781	2	1,2 R
24811	2	1,0 R	23773	3	1,2 Q
24806	4	1,0 Q	23767	1	2,3 R
24780	1	2,1 R	23760	2	2,3 Q
24774	3	2,1 Q	23752	1	3,4 R
24746	1	3,2 R	23745	1	3,4 Q
24742	2	3,2 Q			
24417	5	0,0 R^+		$K \rightarrow X_1$	
24412	7	0,0 Q^+	24901	2	1,0
24388	3	1,1 R^+	24879	2	2,1
24383	5	1,1 Q^+	24857	2	3,2
24360	2	2,2 R^+	24837	1	4,3
24354	4	2,2 Q^+	24495	5	0,0$^+$
23994	2	0,1 R	24478	4	1,1$^+$
23988	3	0,1 Q	24460	3	2,2
23969	1	1,2 R	24441	2	3,3
23964	2	1,2 Q	24426	1	4,4
23944	1	2,3 R	24073	2	0,1
23939	2	2,3 Q	24059	2	1,2
23919	1	3,4 R	24045	2	2,3
23915	2	3,4 Q	24032	1	3,4
	$J_1 \rightarrow X_1$		24018	1	4,5
24216	4	0,0 R			
24209	5	0,0 Q			

$^+$Bands reported by Reddy and Rao[2]

Table 3—Bandhead Data of $L \rightarrow X$ System of NiCl Molecule

ν_{vac} cm^{-1}	Int.	(v', v'')	ν_{vac} cm^{-1}	Int.	(v', v'')
	$L_1 \rightarrow X_1$			$L_1 \rightarrow X_1$	
25022	4	1,0 R		$L_2 \rightarrow X_2$	
25016	3	1,0 Q^+	24738	4	1,0 R
25001	3	2,1 R	24733	3	1,0 Q
24993	2	2,1 Q^+	24708	3	2,1 R
24976	3	3,2 R	24702	2	2,1 Q
24970	2	3,2 Q^+	24676	2	3,2 R
24955	2	4,3 R	24670	1	3,2 Q
24947	1	4,3 Q	24643	1	4,3 R
24928	1	5,4 R	24638	1	4,3 Q
24922	1	5,4 Q	24333	6	0,0 R^+
24615	7	0,0 R^+	24329	5	0,0 Q^+
24609	5	0,0 Q^+	24306	5	1,1 R^+
24598	5	1,1 R^+	24301	4	1,1 Q
24592	3	1,1 Q^+	24279	3	2,2 R
24580	3	2,2 R^+	24275	2	2,2 Q
24573	2	2,2 Q	24251	2	3,3 R
24563	3	3,3 R	24247	1	3,3 Q
24557	2	3,3 Q	23902	4	0,1 R
24542	2	4,4 R	23898	3	0,1 Q
24535	1	4,4 Q	23879	3	1,2 R
24522	2	5,5 R	23875	2	1,2 Q
24513	1	5,5 Q	23855	3	2,3 R
	$L_1 \rightarrow X_2$		23850	2	2,3 Q^+
24131	5	0,0 R^+	23831	2	3,4 R
24126	4	0,0 Q	23827	1	3,4 Q
24112	4	1,1 R^+	23806	2	4,5 R
24105	3	1,1 Q	23801	1	4,5 Q
24090	3	2,2 R	23781	1	5,6 R
24085	2	2,2 Q	23777	1	5,6 Q

$^+$Bands reported by Reddy and Rao[2]

Table 4—Vibrational Constants for Various Electronic States of NiCl Molecule

State	T_o, cm^{-1}	ω_e	$\omega_e x_e$
L	24815	408.0	2.00
	24611	412.5	2.30
K	24495	410.0	2.00
J	24414	398.0	1.75
	24213	412.3	2.40
I	23332	400.4	2.05
	23216	407.5	2.75
H	22952	409.8	1.80
	22732	406.0	1.75
G	22228	405.0	1.50
	21908	412.5	2.25
F	21726	417.2	1.50
	21642	412.0	2.50
E	21014	413.5	2.25
	20838	412.0	2.25
D	20719	406.7	2.40
	20623	411.0	2.00
C	20178	414.0	2.10
	19963	404.8	2.00
B	19047	403.5	1.25
	18817	413.6	1.80
A	18679	407.7	1.60
	18457	410.0	1.50
X_2	484	433.9	1.80
X_1	0	427.0	1.90

Ground state is involved in all the observed transitions and all the bands are degraded to red.

systems in the transitions is shown by differing thickness of the lines representing transition. Table 4 lists the vibrational constants for various electronic states so far studied in thermal emission of NiCl molecule.

An estimate of dissociation energy D_e has been made by using the expression $D_e = \omega^2/4\,\omega_e x_e$. The dissociation energy obtained for ground state of NiCl is 25045 cm^{-1} while for NiH it is 2097 cm^{-1} (Andersen *et al.*[9]). This shows that the chloride of the nickel should be more stable than the hydride.

Acknowledgement

The authors are thankful to Prof Vachaspati, Heat, Physics Department, for his encouragement. One of the authors (RG) is grateful to Prof D K Rai, Physics Department, Banaras Hindu University, Varanasi, for many helpful suggestions.

References

1 Krishnamurty V G, *Indian J Phys*, **26** (1952) 207.
2 Reddy S P & Rao P T, *Proc Phys Soc London (GB)*, **75** (1960) 275.
3 Rao S V K, Reddy S P & Rao P T, *Z Phys (Germany)*, **166** (1962) 261.
4 Rao N V K & Rao P T, *Curr Sci (India)*, **38** (1969) 589.
5 Darji A B & Shah N R, *Indian J Pure & Appl Phys*, **18** (1980) 802.
6 Gopal R & Joshi M M, *Indian J Phys B*, **55** (1981) 368.
7 Gopal R, *Curr Sci (India)*, **50** (1981) 854.
8 Gopal R & Joshi M M, *Indian J Pure & Appl Phys*, **20** (1982) 280.
9 Andersen E, Lagerqvist A, Neuhaus H & Aslund N, *Proc Phys Soc London (GB)*, **82** (1963) 637.

NOTES

Indian Journal of Pure & Applied Physics
Vol. 21, October 1983, pp. 599-601

Switching in Single Crystals of the (Mo/W)Se_2 System

M K AGARWAL, P D PATEL & O VIJAYAN
Department of Physics, Sardar Patel University, Vallabh Vidyanagar 388 120

Received 3 *September* 1982; *accepted* 14 *March* 1983

The phenomenon of electrical threshold switching has been observed in single-crystal solid-solutions in the series $Mo_xW_{1-x}Se_2$ ($0 \leqslant x \leqslant 1$). The current-voltage characteristics show current-controlled negative resistance regions. A linear variation of the holding voltage with crystal composition has been obtained. The results are discussed on the basis of the existing models of switching.

The phenomenon of electrical threshold switching was first described by Ovshinsky[1]. Although initially observed in thin films of amorphous or glassy materials, of late, there has been an explosion in literature on the phenomenon observed in organic compounds[2,3], semi-insulating materials[4], single crystals[5] and thin films[6-8]. More and more new materials are being discovered to show this interesting property. This note describes electrical threshold switching observed across the layers in the layer crystals in the series $Mo_xW_{1-x}Se_2$ ($0 \leqslant x \leqslant 1$). The end compounds of the series, viz. WSe_2 and $MoSe_2$ have been widely studied for their interesting electrical[9,10] and optical[9,11,12] properties. The crystals used in the present study were found to be 2H polytypes[13] and were *p*-type semiconductors.

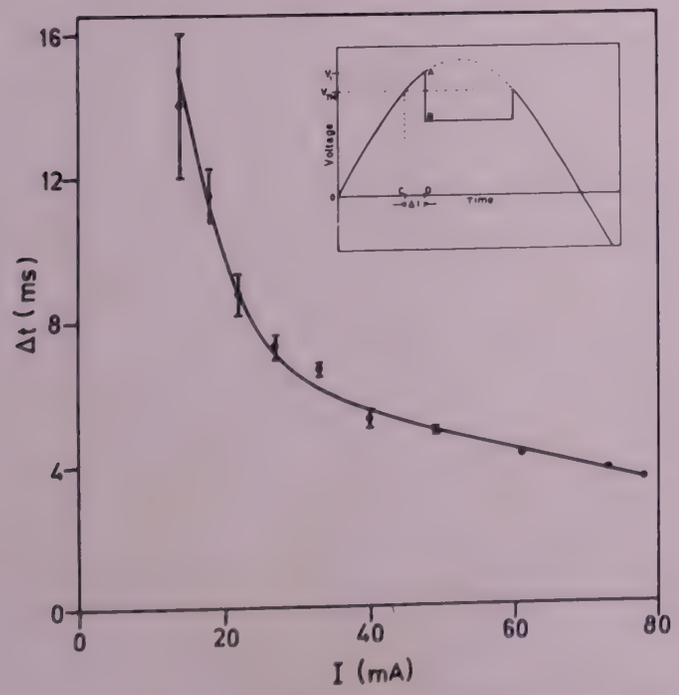

Fig. 1—Plot of delay time as a function of the device current (Inset shows details of measuring delay time.)

Contacts were provided across the layers by a stainless steel jig with a contact area of about 0.016 cm^2. The measurements were done with sinusoidal ac and the current-voltage characteristic (CVC) was obtained on the CRO screen. Fig. 1 (inset) shows the details of the measurement; when the alternating voltage reaches the threshold value V_{TH} the unit does not switch immediately but switches after reaching a value V_1. Thus the time elapsed between the application of the threshold voltage and the onset of switching corresponds to the delay time Δt and can be measured from the CRO trace as CD, on the time axis. Just near the threshold voltage there is considerable statistical variation of the delay time. This can be observed as the random shifting of the line AB towards left and right and can be measured.

Fig. 2 shows the ac trace of the device operating in the bipolar mode in which switching occurs for either polarity of the applied voltage. The dc characteristics are shown in Fig. 3. The figure shows the ON and OFF regimes and the current-controlled negative resistance (CCNR). The delay time as a function of the device current is plotted in Fig. 1. The vertical bars represent the upper and lower limits observed for the delay time.

The holding voltage (V_H) which represents the minimum voltage that is required for the device to remain in the ON state has been determined by extrapolating the linear portion of the ON-state in the CVC to the voltage axis (Fig. 3). Fig. 4 shows the variation of V_H with crystal composition.

The crystals used were having thicknesses ranging from 0.001 to 0.02 cm. As the measurement of the crystal thickness at the point of contact was not possible, the thickness dependence of V_{TH} could not be investigated. However, different crystals of the same composition having different thicknesses gave nearly the same value of V_{TH} suggesting a negligible or no dependence of V_{TH} on thickness. Only slight reduction (<0.2 V) of V_{TH} was observed upon heating the crystal

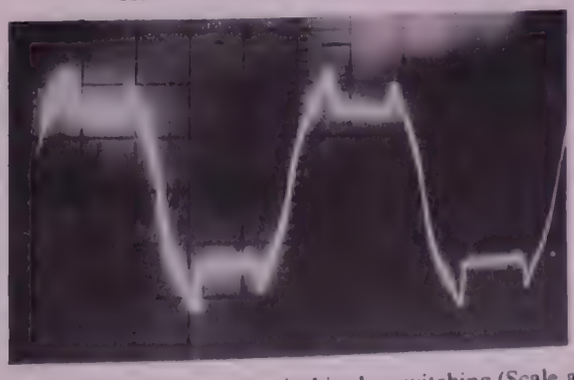

Fig. 2—ac Trace of the device in bipolar switching (Scale along: X-axis, 5 ms/div; Y-axis, 5 V/div; $x = 0.2$)

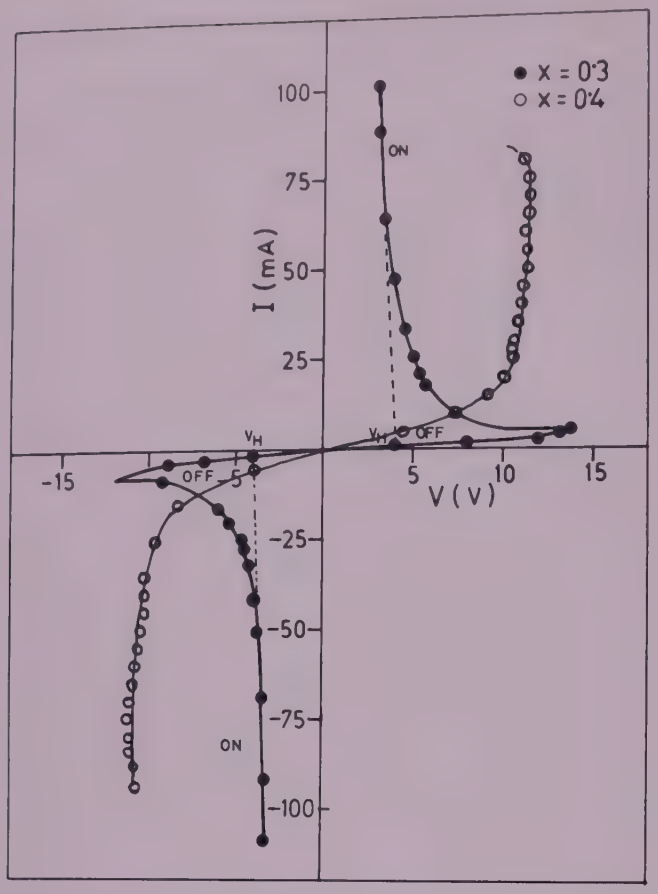

Fig. 3—Current-voltage characteristics for two crystal compositions

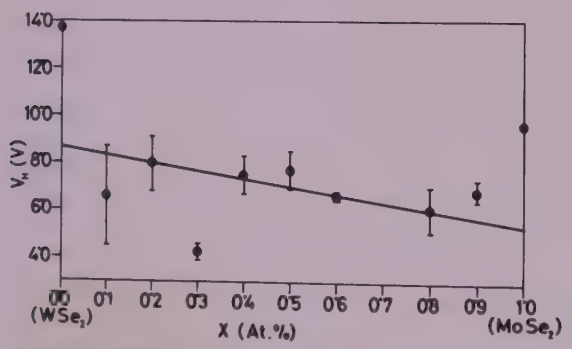

Fig. 4—Plot of V_H versus crystal composition

to red heat by a flame. Lowering of V_{TH} was found upon illuminating the crystal with a laser of moderate intensity and the effect of the intensity and wavelength of the incident radiation of the lowering of V_{TH} is under study.

Gattef and Dimitriev[14] observed monopolar and bipolar switching in vanadium-telluride glasses. The phenomenon has been explained as due to a reversible formation and decay of crystalline nuclei. Such a theory is not applicable to crystalline materials. Chopra[15] obtained similar results as in the present study for oxide of Nb, Ti and Ta. The nonlinear part of the CVC in his case gave a relation similar to the space charge limited current in a trap-filled insulator [i.e. $I \approx V^n \times (\text{thickness})^3$]. The present study shows an exponential increase of current with voltage, near V_{TH}.

Delay time in most of the cases reported for other materials is of the order of 10 μs. But Brodovoi *et al.*[16] observed delay time from 10^{-6} to 10^{-8} s in ZeSe-Cu ceramics. Only a few samples in the present study showed long delay times (Fig. 1). Such samples often showed some sort of 'forming' effects prior to switching indicating high level of defects in the structure. Otherwise all the samples showed fast response; the fact, that only a small change in V_{TH} is observed with temperature, suggests that ionic motion does not play any role in the process[15].

The models used to explain switching phenomena fall basically into two classes, viz. thermal and electronic. In thermal models a hot or molten filament having a width of a few microns forms in the material, between the electrodes, through which the current is channelled[17,18]. According to thermal theories one must find a negative slope for the ON-state in the CVC[17]. This has been observed in the present study (Fig. 3). But this need not necessarily mean that the mechanism is of thermal origin. Microscopic examination of the cleaved surfaces of crystals showing switching did not reveal any filament. When the device was operated at high currents ($\sim$150 mA) for some time the voltage across the device shifted into a highly conducting state indicating that some permanent change of structure has occurred. A microscopic examination of the cleaved surfaces of such crystals also did not show any change. Moreover, if a molten channel is formed across the layers, that should be indicated in the measured resistivity across the layers. But the resistivity across the layers did not vary much and hence a structural change with the formation of a molten channel seems unlikely.

Only electronic theories could be used to interpret the present results. According to electronic theories, the holding voltages should be of the order of the energy band gap of the material[17]. However, much higher values have been obtained in the present study. Mott[18] explains the occurrence of the high holding voltage as due to deep traps far away from the potential barriers formed at the contacts. Manfredotti *et al.*[19] obtained CVC controlled by deep hole traps in layered crystals of GaSe in which the traps are believed to be formed by dislocations or stacking faults. Such a case is evidently applicable to the layered crystals such as those considered here.

The authors are grateful to Dr G K Shivakumar for useful discussions. The authors wish to thank Mr R M Joshi for his assistance in preparing the manuscript. One of the authors (OV) wishes to thank the University Grants Commission, New Delhi for financial assistance.

References

1 Ovshinsky S R, *Phys Rev Lett (USA)*, **21** (1968) 1450.
2 Schmidt P E, Mena J G & Callaroti R C, *Thin Solid Films (Switzerland)*, **55** (1978) 9.

3 Segui Y, Bui Ai & Carchano H, *J Appl Phys* (*USA*), **47** (1976) 140.
4 Hrivnak L, *Phys Status Solidi a* (*Germany*), **37** (1976) K1.
5 Takahashi T & Yamada O, *J Appl Phys* (*USA*), **48** (1977) 1258.
6 Bernede J C, *Phys Status Solidi a* (*Germany*), **57** (1980) K101.
7 Bernede J C, *Phys Status Solidi a* (*Germany*), **65** (1981) 97.
8 Bernede J C, *Thin Solid Films* (*Switzerland*), **81** (1981) 155.
9 Wilson J A & Yofee A D, *Adv Phys* (*GB*), **18** (1969) 193.
10 Brixner L H & Teufer G, *Inorg Chem* (*USA*), **2** (1963) 992.
11 Beal A R & Hughes H P, *J Phys C* (*GB*), **12** (1979) 881.
12 Beal A R, Liang W Y & Hughes H P, *J Phys C* (*GB*), **12** (1976) 2449.
13 Agarwal M K & Wani P A, *Mater Res Bull* (*USA*), **14** (1979) 825.
14 Gattef E & Dimitriev Y, *Philos Mag B* (*GB*), **40** (1979) 233.
15 Chopra K L, *J Appl Phys* (*USA*), **36** (1965) 184.
16 Brodovoi V A, Devikot N Z, Kayak B R *et al.*, *Phys Status Solidi* (*Germany*), **37** (1976) 363.
17 Adler D, Henisch H K & Mott N F, *Rev Mod Phys* (*USA*), **50** (1978) 209.
18 Mott N F, *Philos Mag* (*GB*), **24** (1971) 911.
19 Manfredotti C, Murri R & Rizo A, *Phys Rev B* (*USA*), **10** (1974) 3387.

Indian Journal of Pure & Applied Physics
Vol. 21, October 1983, pp. 602-603

Behaviour of Nitrogen in $GaAs_{1-x}P_x$ ($x \geq 0.86$)

M MOUNIR* & N NORTDINOV†
Department of Physics, Faculty of Science
Cairo University, Cairo, Egypt

Received 6 July 1982; revised received 28 February 1983

This study on the behaviour of nitrogen in $GaAs_{1-x}P_x$ samples (grown from the vapour by epitaxial deposition on GaP substrates) showed: (i) the present theoretical treatments, with the assumption that the spectral maxima are not functions of N_2 concentration, are no more valid (ii) the decay time decreases and the luminescent intensity increases with N_2 concentration. The line broadening, the decay and the recombination times are discussed in view of the classical Chevallier model.

The $GaAs_{1-x}P_x$ crystals famous for their visible luminescence are of practical interest in the fabrication of the light emitting devices. The influence of nitrogen on the luminescent properties of $GaAs_{1-x}P_x$ has been investigated by many workers[1-4]. We report here our investigations on the $GaAs_{1-x}P_x$ samples grown by vapour phase epitaxy on GaP substrates at 800°C. For the indirect alloy composition $x \geq 0.86$, the properties of 3 specimens, grown with different concentrations of nitrogen with film thickness 30-100 μ are given in Table 1. The determination of the composition of $GaAs_{1-x}P_x$ solid solutions was described by Mounir *et al.*

Our measurements were carried out at two rates of excitation differing by more than four orders of magnitude, which we shall call low ($\omega_1 \approx 0.4$ W/cm^2) and high ($\omega_2 \approx 2 \times 10^4$ W/cm^2). At low excitation rates we used an LPM-11 model of an He-Cd laser ($\lambda = 441.6$ nm) operating continuously; at high rates we employed an LGI-21 model of a pulsed N_2 laser ($\lambda = 337.1$ nm, pulse duration 10 nsec, repetition frequency 80 Hz). In the case of cw He-Cd laser we recorded the luminescence spectra by the photon counting method and spectroscopic method for pulsed N_2 laser. We employed a high-luminosity grating monochromator of the MDR-1 type with a typical spectral resolution of 0.1 nm. Samples were bonded to a heat sink in an optical cryostat.

Fig. 1 shows the photoluminescence spectra of $GaAs_{1-x}P_x$:N samples with different concentrations of nitrogen at 60 K and $x \geq 0.86$. At $x \geq 0.86$ the luminescence consisted of broad lines with maxima at 574 and 568 nm. An increase in the nitrogen concentration shifted these maxima towards higher wavelength (lower energies) by 1-6 MeV. This was greater than the total error associated with the determination of x and $\hbar\omega$. At 300K also we obtained the same results. Controlled experiments were carried out on 3 samples and in these experiments the near surface of a sample was specially blackened: the results showed that the shift of the maxima resulting from an increase in self-absorption associated with the increase in N_N, was five times less than the observed effect. These qualitative results are important in the interpretation of the recombination mechanism.

Table 1—Properties of $GaAs_{1-x}P_x$:N Samples

$GaAs_{1-x}P_x$:N	$x+\sigma_x$	$n \times 10^{17}$ cm^{-3}	$N_N \times 10^{18}$ cm^{-3}
R-14-1	0.860+0.001	1.6	1.4
R-14-2	0.856+0.001	1.8	1.9
R-14-3	0.856+0.001	2.8	3.5

n, the concentration of free carriers; N, the concentration of nitrogen; σ_x, the error in x; x, the mole fraction of phosphor.

Fig. 2 shows the decay of the integrated intensity after the laser pulse, for alloys with different concentrations of nitrogen. The integrated intensity of

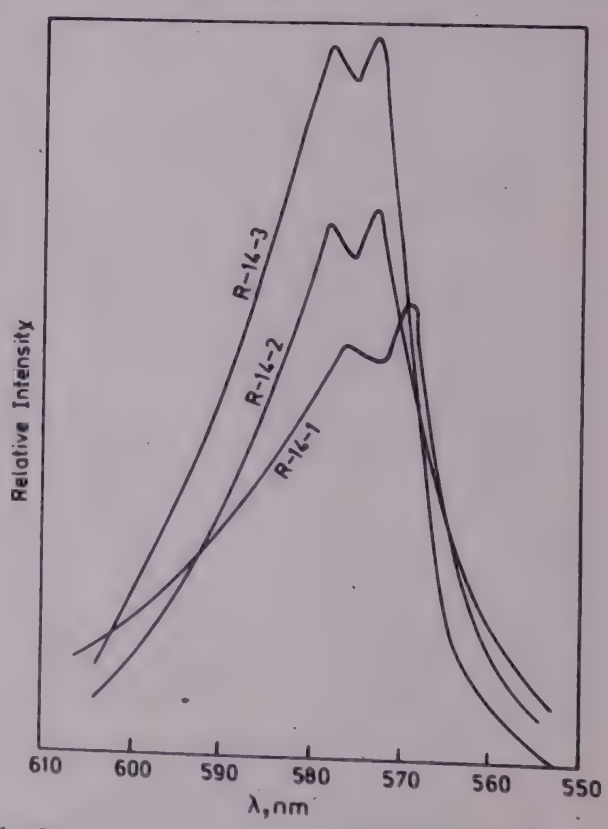

Fig. 1— Photoluminescence spectra of $GaAs_{1-x}P_x$:N($x \geq 0.86$) with different concentrations of nitrogen at 60 K

*Present address: Department of Physics, Faculty of Education, University of Baghdad, Elwazyria, Iraq.
†Department of Semiconductors, Faculty of Physics, Moscow University, Moscow.

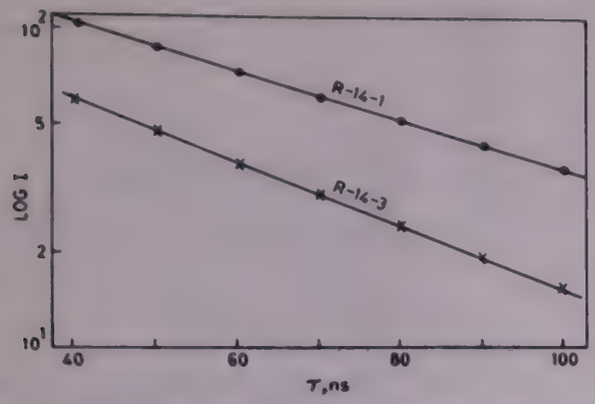

Fig. 2—The decay time of the integrated intensity at 60 K, after the laser pulse for alloys of different concentrations of nitrogen [$GaAs_{1-x}P_x$:N ($x \sim 0.86$); He-Cd laser, 0.4 W/cm^2]

photoluminescence spectra was calculated from the time-resolved spectra. Fig. 2 shows that the decay time of luminescence spectra at 60 K decreases as the concentration of nitrogen traps increases.

From our present study on $GaAs_{1-x}P_x$ as stated above we conclude the following:

(i) The theoretical treatment based on the assumptions that the maxima of line spectra are not functions of nitrogen concentration is not sound and hence must be revised.

(ii) The fluctuations due to statistical disorder in the As-P sublattice in the immediate vicinity of the NN pairs should result in stronger line broadening as in Fig. 2.

The decay time of luminescence for $GaAs_{1-x}P_x$:N with different N_2 concentrations was not reported earlier and needs further study. The classical model which is studied by Chevallier confirms our results shown in Fig. 2. In this case the decay time τ is equal to the exciton recombination time, i.e. the decay time mechanism is not due to the non-radiative centres.

The authors are grateful to A E Yunovich for valuable discussions.

References

1 Mounir M, Nortdinov N, Stegmann R & Yunovich A E, *Sov Phys Semicond (USA)*, **15** (1981) 721.

2 Mounir M, Nortdinov N, Stegmann R & Yunovich A E, *Fiz Tekh Poluprovodn (USSR)*, **15** (1981) 1249.

3 Roessler D M & Swets D E, *J Appl Phys (USA)*, **49** (1978) 804.

4 Mariette H & Chevallier J, *Solid State Commun (USA)*, **29** (1979) 263.

5 Chevallier J & Mariette H, *J Appl Phys Lett (USA)*, **28** (1976) 375.

6 Kleiman G G, *Phys Rev B (USA)*, **15** (1977) 802.

7 Pikhtin A N, *Fiz Tekh Poluprovodn (USSR)*, **11** (1977) 425.

Indian Journal of Pure & Applied Physics
Vol. 21, October 1983, p. 604

Unit Cell and Space Group Determination of Sesebrinol ($C_{20}H_{26}O_6$)

S D SHARMA & K N GOSWAMI
Physics Department, Jammu University, Jammu

Received 9 *January* 1981; *revised received* 14 *January* 1983

The unit cell and space group of sesebrinol have been determined by X-ray diffraction method. The photographic method of collection of data has been supplemented by diffractometer method. The compound is monoclinic with space group $p2$, having two molecules per unit cell.

Sesebrinol (m.p., 114°C), a new coumarin, has been isolated by Raman Kumar *et al.* from the roots of *Sesel sibiricum* Benth, an odorous herb growing in Jammu and Kashmir State at the altitude of 2500-3500 m. It has been assigned the chemical structure, 7-methoxy-8-(3-methyl-2, 3-dihydroxy butyl)-5-(3-methyl but-2-enlexy) coumarin on the basis of its chemical data.

The chemical structure assigned to the compound is shown in Fig. 1.

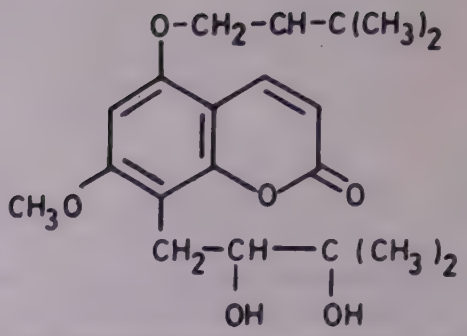

Fig. 1—Chemical structure of sesebrinol

Sesebrinol crystallizes into transparent needles, prismatic in shape with one end tapering. The microscopic examination revealed that most of the crystals are having voids and inclusions in their middle along the needle axis. By examining under polarized light some were found to be single crystals devoid of defects. A well defined needle of a single crystal (1.5 mm × 1.2 mm × 0.2 mm) was chosen for its X-ray study using the Weissenberg method. The crystal specimen was mounted on the goniometer head with its needle axis (c) as the axis of rotation. Oscillation, rotation and Weissenberg photographs did not reveal any symmetry. Zero-level Weissenberg photograph revealed extinctions along $0k0$ for k odd, indicating the presence of a screw axis along b direction. Higher level Weissenberg photographs did not reveal any extinction.

The lattice is thus primitive (P) and so the space group can either be $P2_1$ or $P2_1/m$. From density considerations the number of molecules per unit cell have been found to be 2. This indicates that the possible space group is $P2_1$ and not $P2_1/m$ as the latter demands 4 molecules per unit cell. This is further supported by the fact that the compound sesebrinol being optically active excludes the possibility of the presence of mirror planes in its space group. Hence the space group is taken as $P2_1$.

Table 1—Crystallographic Data of Sesebrinol

Molecular formula	: $C_{20}H_{26}O_6$
Molecular weight	: 362
Crystal system	: Monoclinic
Space group	: $P2_1$
Cell parameters	: $a = 11.38$ Å; $b = 15.33$ Å; $c = 5.33$ Å
Number of molecules per unit cell	: 2
Observed density (d_o)	= 1.29 g cm^{-3}
Calculated density (d_c)	= 1.27 g cm^{-3}

Lattice parameters were initially determined from the rotation and zero-level Weissenberg photographs. The intensity data were collected along c-axis by using multiple film technique. As much difficulty was encountered in mounting the crystal along its unique axis b, intensity data are finally collected on CAD-4 automatic diffractometer at the Regional Sophisticated Instrumentation Centre, Indian Institute of Technology, Madras, from another crystal of suitable size. The cell parameters obtained from the diffractometer output agreed closely with the parameters obtained from the photographic method.

The density of the crystal was determined by flotation method using the homogeneous mixture of peteroleum ether and water. The measurements using specific gravity bottle were made on an electric balance.

The calculated density of the compound, assuming 2 molecules per unit cell, agreed closely with the observed density. The crystallographic data of the compound are summarized in Table 1.

The crystal structure determination of the compound is under progress using direct methods.

The authors wish to record their sincere thanks to Dr S K Banerjee, Regional Research Laboratory, Jammu, for supplying them the compound.

References

1 Raman Kumar, Banerjee S K & Atal C K, *Phytochemistry (USA)*, 19 (1980) 281.

Indian Journal of Pure & Applied Physics
Vol. 21, October 1983, pp. 605-608

Calculations of Geometry & Molecular Properties by Semiempirical Molecular Orbital Method (SINDO)

C P D DWIVEDI

Department of Physics, University of Gorakhpur, Gorakhpur 273001

Received 23 *October* 1982; *revised received* 18 *March* 1983

Geometry, binding energy, force constants, ionization potential, dipole moment, net charges and bond orders for 18 triatomic molecules have been calculated using semiempirical molecular orbital method SINDO (symmetrically orthogonalized intermediate neglect of differential overlap). Results obtained have been compared with the experimental and the *ab initio* results.

Calculations of geometry and other molecular properties have been one of the main objectives of quantum chemistry. In *ab initio* calculations, use has been made of the treatment introduced by Roothaan[1] and Hall[2] independently. If sufficiently large and well chosen basis set is used, the results can approach the theoretical Hartree-Fock limit set by the orbital approximation. The main problem in *ab initio* calculations is that there are large number of difficult integrals over the basis functions that are required. Approximate molecular orbital theories have been developed[3,4] which are by nature semiempirical in that one no longer attempts to derive molecular properties directly from the principles of quantum mechanics but rather seeks to interpret correlations within the experimental data. In this direction a new approach has been made for the calculation of geometry, energy and some other molecular properties like dipole moment, binding energy and ionization potential. This method was developed by Jug[5] and is known as SINDO (symmetrically orthogonalized intermediate neglect of differential overlap). The SINDO scheme is a modified INDO procedure in which parameter formulae are developed on symmetrically-orthogonalized basis set. Calculations by this method on diatomic molecules have been found to be very satisfactory[6]. In this note, we have extended these calculations to triatomic molecules and compared the results with those of experimental and *ab initio* calculations. For the details of this method, the reader is referred to Refs 5 and 6.

Method—Lowdin[7] has shown that any set of linearly independent orbitals ϕ may be orthogonalized by the transformation:

$$\hat{\phi} = \phi S^{-\frac{1}{2}}$$

$S^{-\frac{1}{2}}$ is defined such that $S^{-\frac{1}{2}}S^{-\frac{1}{2}} = S^{-1}$ where S^{-1} is the inverse of the overlap matrix. The set $\hat{\phi}$ has the same symmetry properties as ϕ and is as close to ϕ as possible in the least square fit. It has been shown that greater justification of zero differential overlap (ZDO) approximation can be obtained by using symmetrically orthogonalized basis set. As a matter of fact, the conditions imposed by the ZDO approximation are in fact extremely small.

In the present work, molecular geometries are defined in terms of bond lengths and bond angles. The equilibrium geometry was determined by minimizing energy with respect to these coordinates. The geometry optimization was carried out by an approach based on the well known Newton-Raphson method. In this method, the function of the energy with respect to the coordinates is analytically differentiated with respect to each coordinate. Second derivatives are then taken with respect to each coordinate. It is then desired to move the atoms to points where all the first partial derivatives are simultaneously zero. This can be accomplished by solution of $3N-6$ simultaneous equations. One does not usually reach the energy minimum on the first try and the process is repeated with the improved coordinates as many times as required. The two strong points in favour of this method are that: (i) analytical differentiation is much faster than numerical differentiation, and (ii) the atoms can be moved in one iteration to an approximation of the energy minimum geometry, which is a much greater improvement over the trial geometry than can be obtained by the steepest descent method. A practical disadvantage of this method is that one must calculate sufficient elements to fill out $(3N-6)\times(3N-6)$ matrix which then must be diagonalized.

Variable method used here generates improved geometries X^{n+1} from the old geometries X^n by using the recursion where g^n is the energy gradient and A denotes the matrix of second partial derivatives of energy:

$$X^{n+1} = X^n - (A^n)^{-1} g^n$$

$$A_{ij} = \frac{\partial^2 E_{\text{mol}}}{\partial X_i \partial X_j}$$

First derivatives can be calculated either analytically using the Hellmann-Feynman theorem and neglecting the variation of LCAO coefficients in the vicinity of stationary points, or numerically. The second derivatives can be obtained only numerically because the variation of the LCAO coefficients cannot be neglected.

Table 1 — Triatomic Molecular Properties

Molecule	Method	Geometry			Binding energy	Force constant, a.u.			Ionization potential	Dipole moment	Net charges, a.u.			Bond order		
		R_1 Å	R_2 Å	θ deg.	Hartree	f_{11}	f_{22}	f_{33}	Hartree	Debye	X_1	X_2	X_3	P_{12}	P_{23}	P_{13}
HBeH	This work	1.434	1.434	180.0	0.1863	1.095	1.095	0.000	0.503	0.000	−0.772	1.459	−0.772	0.961	0.962	−0.150
	ab inito	1.343[11]	1.343	180.0					0.437[11]							
	Exptl	1.343[10]	1.343	180.0												
HBH	This work	1.292	1.292	130.0	0.2638	1.578	1.578	0.000	0.419	0.24	−0.105	1.210	−0.105	0.959	0.959	−0.138
	ab initio	1.182[12]	1.182	128.4						0.44[12]						
	Exptl	1.180[10]	1.180	136.6												
HCH T	This work	1.156	1.56	140.0	0.3473	2.460		0.000	0.496	0.57	−0.092	0.046	0.965	0.965	0.965	−0.165
	ab initio	1.116[13]	1.116	129.0		0.719[13]	0.118	0.877		0.79[13]						
	Exptl	1.094[10]	1.094	141.4												
HCH S	This work	1.189	1.189	107.7	0.3057	2.291		0.000	0.468	2.02	−0.001	0.001	0.001	0.997	0.997	−0.072
	ab inito	1.169[13]	1.169	90.0		0.736[13]	0.094	0.866		0.89[30]						
	Exptl	1.024[10]	1.024	103.3												
HNH	This work	1.064	1.064	118.0	0.4424	3.607	3.607	0.000	0.546	2.08	−0.117	−0.235	−0.117	0.986	0.986	−0.102
	ab initio	1.019[14]	1.019	105.4						1.77[31]						
	Exptl	1.024[10]	1.024	103.3	0.2803[15]											
HOH	This work	1.006	1.006	120.2	0.4633	4.357	4.357	0.000	0.574	2.05	−0.388	0.194	0.194	0.974	0.974	−0.113
	ab initio	1.000[16]	1.000	110.0	0.30[16]				0.432[17]	1.71[16,18]						
	Exptl	0.960[10]	0.960	104.5	0.3532[15]					1.844[22]						
HFH	This work	1.085	1.085	180.0	0.2225	0.482	0.482	0.000	0.367	0.00	0.064	−0.128	0.064	0.702	0.702	0.183
	ab initio															
	Exptl	0.920[10]	0.920	—												
OOO	This work	1:238	1.238	121.8	0.2461	5.302	5.302	0.000	0.548	0.84	−0.145	−0.291	−0.145	1.759	1.759	−0.603
	ab initio	1.322[19]	1.322	—						0.484[20]						
	Exptl	1.278[10]	1.278	116.8					0.470[29]	0.53[20]						
OCO	This work	1.336	1.336	180.0	0.2439	2.694			0.562	0.00	0.546	−0.273	−0.273	2.147	2.147	−0.891
	ab initio	1.250[2]	1.250	180.0												
	Exptl	1.162[10]	1.162	180.0	0.6013[28]					0.00[22]						

(*Contd.*)

Table 1—Triatomic Molecular Properties—(*Contd.*)

Molecule	Method	Geometry			Binding energy	Force constant, a.u.			Ionization potential	Dipole moment	Net charges, a.u.			Bond order		
		R_1 Å	R_2 Å	θ deg.	Hartree	f_{11}	f_{22}	f_{33}	Hartree	Debye	X_1	X_2	X_3	P_{12}	P_{23}	P_{13}
FCF	This work	1.429	1.429	101.1	0.1725	2.932	2.932	0.000	0.589	1.48	−0.296	0.592	−0.296	1.648	1.648	−0.890
	ab initio	1.330[23]	1.330	105.8					0.475[15]	0.321[15]						
	Exptl	—	—	108.0[10]	0.3984[2]				0.433[15]	0.46[15]						
FOF	This work	1.271	1.271	103.7	0.2026	6.338	6.338	0.000	0.637	0.41	−0.101	0.202	−0.101	1.174	1.174	−0.058
	ab initio	1.410[15]	1.410	103.3					0.581[15]	0.295[24]						
	Exptl	1.396[25]	1.396	103.8	0.1431[28]				0.503[15]	0.297[24]						
HCN	This work	1.160	1.248	180.0	0.4185	2.385	7.443	0.000	0.506	2.24	0.089	0.119	−0.137	0.960	2.817	−0.279
	ab initio	1.058[26]	1.157	—					0.581[26]	3.36[26]						
	Exptl	—	—	—	0.4972[26]				0.507[26]	2.98[26]						
HNO	This work	1.085	1.242	114.1	0.3968	3.186	7.612	0.000	0.468	1.931	+0.066	+0.064	−0.132	0.972	2.185	−0.228
	ab initio	1.038[27]	1.321	110.4												
	Exptl	1.063[10]	1.213	108.6												
OBO	This work	1.476	1.476	180.0	0.2053	1.192	1.192	0.000	0.6079	0.00	−0.238	0.476	−0.238	2.119	2.119	—
	ab initio	—	—	—												
	Exptl	1.250[10]	1.250	180.0												
ONO	This work	1.247	1.247	133.8	0.3777	5.535	5.535	0.000	0.513	0.722	−0.212	0.424	−0.212	2.002	2.002	—
	ab initio	—	—	—												
	Exptl	1.200[10]	1.200	132.0												
FNF	This work	1.318	1.318	98.6	0.2507	5.857	5.857	0.002	0.591	0.85	−0.184	0.368	−0.184	1.428	1.428	—
	ab initio	1.370[15]	1.370	104.0					0.567[15]	0.564[15]						
	Exptl	1.350[10]	1.350	104.2	0.2242[28]				0.422[15]							
CCH^+	This work	1.296	1.328	60.8	0.072	3.500	1.321	0.000	0.386	—	—	—	—	—	—	—
CCH^-	This work	1.336	1.224	180.0	0.3488	3.980	1.661	0.000	0.032	2.486	—	—	—	—	—	—

1 Hartree = −27.21 eV

X_1, X_2 and X_3 are net charges on atoms 1, 2 and 3 respectively.

P_{12}, P_{23} and P_{13} are bond orders between atoms 1 and 2, 2 and 3 and 1 and 3, respectively.

Superscripts indicate references and they are given in the table at only one place for one set of results in order to avoid repetition. T and S stand for singlet and triplet respectively (see CH_2 molecule).

In these calculations only the valence shell electrons are considered explicitly, the inner shell electrons being treated as part of the core. However, it is found that the true total energy of the molecule obtained from the calculation using a basis set expansion over the valence shell as well as the inner shell atomic orbitals, has the molecular part mainly reflected in the valence electron energy. Therefore, it is still meaningful to use this energy in predicting geometries and energetic features of the molecules.

The calculated binding energy, E_b, for equilibrium geometry of a molecule is obtained as the difference between the energy of the molecule and that of its constituent atoms. Koopman's theorem[8] has been used for calculating ionization potential. Bond order calculation is based on a new concept introduced by Jug[9]. It is based on diagonalization of two-center parts of the density matrix. It is shown here that the bond order between two atoms can be obtained as a sum of eigenvalues of a resulting eigenvalue equation. This method contains Coulson-electron bond order as a special case, but differs from Mulliken's method in various aspects. Net charge on an atom is the difference of number of valence electrons and electron density.

Results and discussion—Bond lengths and bond angles, binding energy, force constants, ionization potential, dipole moment, net charges and bond order for a series of 18 triatomic molecules are listed in Table 1. The results of the present work are compared with those of the experimental and *ab initio* calculations as far as they are available. Agreements are within the same order of magnitudes as in the case of diatomic molecules[6]. Bond lengths are expressed in angstroms and bond angles in degrees. Binding energy, force constants and ionization potential are expressed in atomic units. Atomic unit of energy (Hartree) is equal to -27.21 eV. Negative signs of binding energy and ionization potential have been omitted as is very often the case. Numbering of the atoms is from left to right, viz. in HBeH molecule Be is numbered second, hydrogen atom on the left is numbered first and that on the right third.

We find that binding energies, bond distances, bond angles, ionization potentials and dipole moments from the present calculations are in fairly good agreement with the experimental and the *ab initio* results. CCH^+ and CCH^- are merely conceived systems. No *ab initio* results are available for them. However, the binding energy of CCH^- is found to be of the order which indicates that it can be a stable system. Binding energy of CCH^+ is very small which shows that it cannot be a stable system. As expected, ionization potential of CCH^- is very small compared to that of CCH^+.

These calculations were done on CDC-7600 computer at Hannover University, West Germany. The author is grateful to Hannover University for furnishing computer time. He is also grateful to Prof. K Jug of Hannover University for valuable suggestions and discussions during the course of this work.

References

1 Roothaan C C J, *Rev Mod Phys (USA)*, **32** (1960) 179.
2 Hall G G, *Proc R Soc London Ser A(GB)*, **205** (1951) 541.
3 Pople J A, Beveridge D L & Dobos P A, *J Chem Phys* (USA), **47** (1967) 2026.
4 Baird N C & Dewar M S J, *J Chem Phys (USA)*, **50** (1969) 1262.
5 Jug K, *Theor Chim Acta (Germany)*, **30** (1969) 231.
6 Coffey P & Jug K, *J Am Chem Soc (USA)*, **95** (1973) 7575.
7 Lowdin P O, *J Chem Phys (USA)*, **18** (1950) 365.
8 Koopman T, *Physica (Netherlands)*, **1** (1967) 39.
9 Jug K, *J Am Chem Soc (USA)*, **99** (1977) 7800.
10 Pople J A & Beveride D L, *Approximate molecular orbital theory* (McGraw-Hill, New York), 1970.
11 Peyerimhoff S D, Buenker R J & Allen C A, *J Chem Phys (USA)*, **45** (1966) 734.
12 Staemmler V & Jugen M, *Chem Phys Lett (Netherlands)*, **16** (1972) 187.
13 Foster J M & Boys S F, *Rev Mod Phys (USA)*, **32** (1960) 305.
14 Bender C F & Shaefer H F, *J Chem Phys (USA)*, **55** (1971) 4798.
15 Rothenberg S & Shaefer H F, *J Am Chem Soc (USA)*, **95** (1973) 2095.
16 Andriessen J, *Chem Phys Lett (Netherlands)*, **3** (1969) 257.
17 Preuss H & Jandschek R, *J Mol Struct (Netherlands)*, **3** (1969) 423.
18 Aung S, Pitzer R M and Chan S I, *J Chem Phys (USA)*, **49** (1968) 2071.
19 Peyerimhoff S D & Buenk R J, *J Chem Phys (USA)*, **47** (1967) 1953.
20 Petrorogolo C, Tomasi J & Scrouo E, *J Chem Phys (USA)*, **48** (1968) 407.
21 McLean A D, *J Chem Phys (USA)*, **38** (1963) 1347.
22 McClellan A L, *Tables of experimental dipole moments* (W H Freeman & Co, San Fransisco, USA), 1963.
23 Sachs L M, Gellar M & Kaufman J J, *J Chem Phys (USA)*, **51** (1969) 2771.
24 Bonaccorst R, Petrongolo C, Scrocco E & Tomasi J, *J Chem Phys (USA)*, **48** (1968) 1497.
25 Buenker R J & Peyerimhoff S D, *J Chem Phys (USA)*, **45** (1966) 3682.
26 Pan D C & Allen C A, *J Chem Phys (USA)*, **46** (1967) 1979.
27 Sallotto A W & Buruelle L, *Chem Phys Lett (Netherlands)*, **3** (1969) 80.
28 Sanderson R T, *Chemical bonds and bond energy* (Academic Press, New York), 1971.
29 Herzberg G, *Electronic spectra of polyatomic molecules* (Van Nostrand-Reinhold Co, New York) 1966.
30 Del Bene J E, *Chem Phys Lett (Netherlands)*, **9** (1971) 68.
31 Del Bene J E, *J Chem Phys (USA)*, **54** (1971) 3487.

Indian Journal of Pure & Applied Physics
Vol. 21, October 1983, pp. 609-610

Rotational Collision Numbers for Carbon Dioxide

P C JAIN
National Physical Laboratory, New Delhi 110012

Received 26 *November* 1982; *revised received* 23 *April* 1983

Rotational collision numbers for carbon dioxide have been calculated in the temperature range 350-2000 K by employing the recent thermal conductivity data. The computed values do not agree with the experimental data available at lower temperatures, but are consistent with the values derived from the expression of Parker in the temperature range 1100-2000 K.

The efficiency of energy exchange involving rotational and translational degrees of freedom in a polyatomic gas is conveniently characterized in terms of a rotational collision number. This number is an important parameter in the theoretical expressions suggested for the estimation of thermal conductivity of polyatomic gases[1-4]. Reliable values of this number were established earlier for oxygen[5] and nitrogen[6] over wide temperature ranges. In the present work, the values for carbon dioxide have been determined in the temperature range 350-2000 K.

The experimental values of the rotational collision number, Z_{rot}, for carbon dioxide have been reported among others by Andersen and Hornig[7], Mason and Monchick[2], Mason[8], O'Neal and Brokaw[9], Holmes *et al.*[10], Malinauskas[11], Tip *et al.*[12], Healy and Storvick[13], and Annis and Malinauskas[14]. These values, plotted in Fig. 1, are available up to a maximum temperature of 676 K only. At higher temperatures, Z_{rot} values can be estimated, as was done

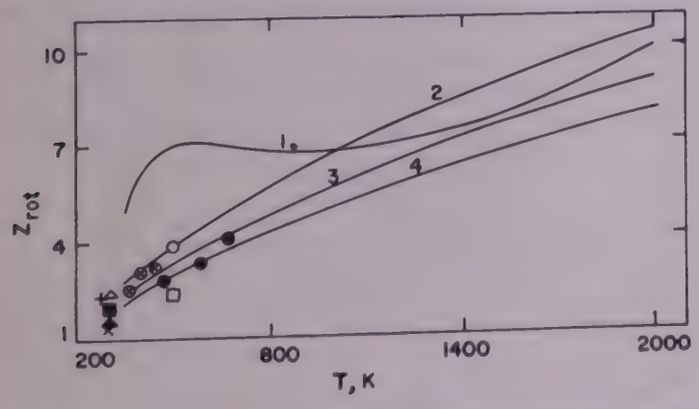

Fig. 1—Z_{rot} values of carbon dioxide as a function of temperature [Curves: 1, calculated from Eq. (1); 2, calculated from Eq. (2) and experimental value of Tip *et al.*[12]; 3, calculated from Eq. (2) and experimental value of Healy and Storvick[13]; and 4, calculated from Eq. (4) and experimental value of Annis and Malinauskas[14]; experimental data: ○, Tip *et al.*[12]; ●, Annis and Malinauskas[14]; □, Malinauskas[11]; ■, Mason and Monchick[2]; +, Mason[8]; ⊗, Healy and Storvick[13]; ×, Holmes *et al.*[10]; Δ, O'Neal and Brokaw[9]; and ▲, Andersen and Hornig[7]]

earlier in the case of nitrogen[6], by employing the thermal conductivity data, the kinetic theory expression for thermal conductivity (Hirschfelder *et al.*[15]) and the following expression due to Saxena *et al.*[3]

$$Z_{rot}=(C_v)_{int}\left[2.5-\frac{\rho D_{int}}{\mu}\right]\Big/\left[C_v(f_H-f)\right] \quad \ldots (1)$$

In Eq. (1), $(C_v)_{int}$ is the contribution of internal energy to constant volume molar specific heat C_v, ρ is the density and μ the viscosity of the gas. D_{int} is the internal energy diffusion coefficient and has been taken equal to the self-diffusion coefficient D. The dimensionless group of properties, $\rho D/\mu$, has been taken equal to $1.2A^*$, where A^* is the ratio of collision integrals. f_H is the Eucken correction factor due to Hirschfelder and f is the correction factor derived from the thermal conductivity expression[6].

The values of Z_{rot} computed from Eq. (1) by employing the thermal conductivity data of Chen *et al.*[16] in the temperature range 350-2000 K are shown by curve 1 of Fig. 1. For this calculation, the parameters of the m-6-8 potential suggested by Hanley and Klein[17] were used ($m=14$, $\gamma=1$, $\varepsilon/k=282$ K and $\sigma=0.368$ nm).

High temperature values of Z_{rot} can also be estimated with the help of the following expression due to Parker[18] as corrected by Brau and Jonkman[19]:

$$Z_{rot}=Z_{rot}^{\infty}\left[1+\frac{\pi^{3/2}}{2}\left(\frac{1}{T^*}\right)^{1/2}+\left(\frac{\pi^2}{4}+2\right)\times\left(\frac{1}{T^*}\right)+\pi^{3/2}\left(\frac{1}{T^*}\right)^{3/2}\right]^{-1} \quad \ldots (2)$$

where, T^* is the reduced temperature and Z_{rot}^{∞} is the limiting value of Z_{rot} at high temperatures. Z_{rot} values have been calculated in the temperature range 350-2000 K with the help of Eq. (2) by separately taking the experimental values of Tip *et al.*[12], Healy and Storvick[13] and Annis and Malinauskas[14]; the latter values are 3.9 at 500 K, 2.47 at 366 K and 2.8 at 475 K respectively. The computed Z_{rot} values are shown in Fig. 1 by curves 2, 3 and 4 respectively. The respective Z_{rot}^{∞} values were found to be 31.1, 26.3 and 23.4.

From Fig. 1, it is seen that the Z_{rot} values computed from Eq. (1) in the temperature range 1100-2000 K are lying almost mid-way between the values calculated from Eq. (2) by separately taking the data of Tip *et al.*[12] (curve 2) and Healy and Storvick[13] (curve 3), and are much larger than those calculated by taking the data of

Annis and Malinauskas[14] (curve 4). The average absolute deviations of the values represented by curves 2, 3 and 4 from those of curve 1 are 10.6, 9.2 and 21.5 per cent respectively in the temperature range 1100-2000 K. The agreement is poor in the temperature range 350-1100 K.

The Z_{rot} values calculated from Eq. (1) are not reliable in the temperature range 350-750 K because of poor agreement with the experimental data. However, in the temperature range 1100-2000 K, these can be taken as reliable because of their fairly good agreement with the values derived from Parker's expression [Eq. (2)], the general applicability of which for calculating the temperature-dependent Z_{rot} values of polyatomic gases has been tested by several workers (e.g. Mason and Monchick[2], Carnevale *et al.*[20]). The present study also brings out the necessity of generating experimental data on Z_{rot} at high temperatures.

The author is grateful to the Director, National Physical Laboratory, New Delhi, for permission to publish this paper.

References

1 Saxena S C & Chen S H P, *Mol Phys (GB)*, **29** (1975) 1507.
2 Mason E A & Monchick L, *J Chem Phys (USA)*, **36** (1962) 1622.
3 Saxena S C, Saksena M P & Gambhir R S, *Br J Appl Phys (GB)*, **15** (1964) 843.
4 Ahtye W F, *J Chem Phys (USA)*, **57** (1972) 5542.
5 Jain P C & Pandya T P, *Pramana (India)*, **11** (1978) 353.
6 Jain P C, *J Phys D (GB)*, **13** (1980) 25.
7 Andersen W H & Horning D F, *Mol Phys (GB)*, **2** (1959) 49.
8 Mason E A, *J Chem Phys (USA)*, **39** (1963) 522.
9 O'Neal C & Brokaw R S, *Phys Fluids (USA)*, **6** (1963) 1675.
10 Holmes R, Jones G R & Lawrence R, *J Chem Phys (USA)*, **41** (1964) 2955.
11 Malinauskas A P, *J Chem Phys (USA)*, **44** (1966) 1196.
12 Tip A, Los J & De Vries A E, *Physica (Netherlands)*, **35** (1967) 489.
13 Healy R N & Storvick T S, *J Chem Phys (USA)*, **50** (1969) 1419.
14 Annis B K & Malinauskas A P, *J Chem Phys (USA)*, **54** (1971) 4763.
15 Hirschfelder J O, Curtiss C F & Bird R B, *Molecular theory of gases and liquids* (Wiley, New York) 1967, p. 534.
16 Chen S H P, Jain P C & Saxena S C, *J Phys B (GB)*, **8** (1975) 1962.
17 Hanley H J M & Klein M, *J Phys Chem (USA)*, **76** (1972) 1743.
18 Parker J C, *Phys Fluids (USA)*, **2** (1959) 449.
19 Brau C A & Jonkman R M, *J Chem Phys (USA)*, **52** (1970) 477.
20 Carnevale E H, Carey C & Larsen G, *J Chem Phys (USA)*, **47** (1967) 2829.

Indian Journal of Pure & Applied Physics
Vol. 21, October 1983, pp. 611-612

Structural Studies on Some Organic Polar Compounds Using Microwave Absorption Technique and NMR

AMBESH SRIVASTAVA & N K MEHROTRA
Department of Physics, Lucknow University, Lucknow 226007

Received 11 *June* 1982; *revised received* 14 *March* 1983

The experimental values of dielectric relaxation time (τ) and NMR spin-lattice relaxation time (T_1) of some polar compounds have been correlated with the calculated values using various equations in the literature. The calculated values of T_1 and τ obtained using Murty's equation [*Indian J Phys*, **32** (1958) 580] are in better agreement with the experimental values. Therefore, it has been concluded that Murty's equation is a better representation for NMR and dielectric relaxation phenomenon.

The study and correlation of dielectric relaxation time (τ) and NMR spin-lattice relaxation time (T_1) has been a subject of interest for investigation of molecular structure of liquids for a long time.

Bloembergen *et al.*[1] derived an expression (BPP theory) for the magnetic relaxation in terms of correlation time which is closely related to Debye's theory[2] of dielectric dispersion in polar liquids. Many workers[3-6] calculated the values of T_1 from the BPP theory and found that the calculated values ranged from 1/2 to 1/10 of the experimental values. The possibility of narrowing the gap between the experimental and the calculated values stimulated the present work reported in this note.

The NMR spin-lattice relaxation of a single nuclear spin in a liquid is induced by the fluctuating local magnetic field of neighbouring spins. If the spin which induces the relaxation is attached to the same molecule as the relaxing spin, the fluctuating field is produced by the molecular reorientational motion. The contribution of this mechanism to the overall T_1 is denoted by $(T_1)_{rot}$ while the relaxation which occurs when the relaxing spin and spin which induces relaxation are attached to different molecules is denoted by $(T_1)_{trans}$. Bloembergen *et al.*[1] calculated the probability of transition induced as discussed in our earlier paper reported elsewhere[7].

We have now calculated correlation time using various equations reported in literature[2,8,9]. The dielectric relaxation times of the compounds investigated have been determined by the Higasi method[10] as discussed in a paper by Saxena and Saxena[11].

It is evident from Table 1 that τ of 1-3-5-trimethyl benzene is greater than that of other compounds,

Table 1—Values of τ at 20°C for the Compounds Studied

Compound	$\tau \times 10^{12}$, s			
	Exptl	Ref. 2	Ref. 8	Ref. 9
Trifluorotoluene	28.62	85.03	14.28	30.62
p-Fluorotoluene	26.56	76.58	13.02′	29.44
1,3,5-Trimethyl benzene	30.24	98.00	17.64	38.81
Isobutyl bromide	25.44	75.41	12.82	27.80

Table 2—Values of T_1 for the Compounds Studied

Compound	T_1, s			
	Exptl	Ref. 2	Ref. 8	Ref. 9
Trifluorotoluene	12.05*	6.68	14.88	11.25
p-Fluorotoluene	13.00*	6.20	15.82	12.43
1,3,5-Trimethyl benzene	10.50*	5.13	12.37	9.15
Isobutyl bromide	9.00†	6.61	13.91	6.69

*Ref. 13; †Ref. 12

which is in accordance with the larger size of the former molecule. Trifluorotoluene has higher value of τ than parafluorotoluene, which may be explained due to greater steric hindrance between the fluorine atoms in the former molecule. The lower value of relaxation time for isobutyl bromide may be explained on the basis of intramolecular rotation of one of the methyl groups. According to Powles and Luszezynski[12], proton magnetic resonance interaction in isobutyl bromide at low temperature is affected by two motions, resulting in the decrease of the observed relaxation time.

It is observed from Tables 1 and 2 that calculated values of τ and T_1 obtained using Debye equation are not in good agreement with the experimental values. Moniz[3] also agrees with this view that BPP treatment gives much smaller value of T_1 due to time dependence of rotational angular autocorrelation function of these molecules. They suggested that the time dependence is dominated by dynamical coherence rather than by frictional forces assumed in BPP theory.

When Wirtz and Spernol equation[8] is used, a better correlation is obtained. This is probably due to the introduction of microfriction factor in the equation.

However, the values of τ and T_1 calculated using Murty's equation are in quantitative agreement with the corresponding experimental values. Therefore, it is concluded that Murty's equation is a better substitute for the correlation time in BPP equation for T_1.

However, any discrepancy which still remains between the calculated and the experimental values of

T_1 can be explained as due to the fact that dielectric relaxation equations are valid for dilute solutions whereas T_1 has been determined in pure liquid state of these compounds.

The authors are deeply indebted to Prof. V D Gupta, Head, Physics Department, Lucknow University, Lucknow, for his interest and encouragement throughout the progress of the work.

References

1 Bloembergen N, Purcell E M & Pound R V, *Phys Rev (USA)*, **73** (1948) 673.
2 Debye P, *Polar molecules* (Blackie & Sons, London), 1929, 90.
3 Moniz W B, *J Chem Phys (USA)*, **38** (1963) 2418.
4 Nederbraght G W & Reitly C A, *J Chem Phys (USA)*, **24** (1956) 1100.
5 Gutowsky N S & Woessuer D E, *Phys Rev (USA)*, **104** (1956) 843.
6 Wilson C W & Pake G E, *J Chem Phys (USA)*, **27** (1957) 115.
7 Somevanshi S K S, Mitra S C & Mehrotra N K, *Indian J Phys*, **52** (1978) 1.
8 Wirtz K & Spernol A, *Z Naturforsch a (Germany)*, **8** (1953) 522.
9 Murty C R K, *Indian J Phys*, **32** (1958) 580.
10 Higasi K, *Bull Chem Soc Jpn (Japan)*, **39** (1966) 2157.
11 Saxena S K & Saxena M C, *Indian J Pure & Appl Phys*, **19** (1981) 550.
12 Powles J G & Luszezynski K, *Proc Phys Soc London (GB)*, **74** (1959) 408.
13 Powles J G & Green D K, *Proc Phys Soc London (GB)*, **85** (1965) 99.

Indian Journal of Pure & Applied Physics
Vol. 21, October 1983, pp. 613-614

Evaluation of Electron Temperature in Glow Discharge from Measurement of Diffusion Voltage

S N SEN, S K GHOSH & B GHOSH
Department of Physics, North Bengal University, Darjeeling 734430

Received 30 *September* 1982; *revised received* 11 *March* 1983

It is shown that the electron temperature in a cylindrical glow discharge column can be evaluated by measuring the radial diffusion voltage due to charge separation. The effect of a transverse magnetic field on electron temperature has also been investigated.

It is well known that in the positive column of a glow discharge due to different rates of diffusion of electrons and ions, an electric field develops as a result of charge separation and this field is effective in equalizing the diffusion rates and the phenomenon of ambipolar diffusion results. As the major part of diffusion is along the azimuthal direction, the field is radial. The radial field E_r is given by

$$E_r = -\frac{1}{n}\cdot\frac{dn}{dr}\cdot\frac{KT_e}{e} \qquad \ldots (1)$$

where n is the charged particle density and other symbols have their usual significance. Eq (1) shows that if T_e is constant then the radial electric field is a function of r. Since it is known that the field is varying, the equation cannot be used for the measurement of T_e. If however, the voltage V_R between the axis and some point at a distance r away is measured then,

$$V_R = \int E_r dr = -\int \frac{dn}{n}\cdot\frac{KT_e}{e}$$

In the case of a uniformly positive column of a glow discharge, the distribution is Besselian

$$n = n_0 J_0(2.405\, r/R)$$

where R is the radius of the discharge tube so that

$$\frac{KT_e}{e} = \frac{V_R}{\log J_0(2.405\, r/R)} \qquad \ldots (2)$$

It is thus evident that if V_R can be measured then the electron temperature can be obtained from Eq. (2).

The experimental assembly consists of a discharge tube of length 10 cm in which the ionized gas under investigation is produced, and the pressure is measured by an accurately calibrated Pirani gauge. Two cylindrical probes of length 1 cm and diameter 0.01 cm are placed parallel to one another, one along the axis $r = 0$ and the other at a distance $r = 0.9$ cm from the axis; the radius of the discharge tube being 1.6 cm.

The output voltage at the two probes is measured by a VTVM having an internal impedance of 100 MΩ. A filter circuit is provided at the output of the probes to prevent oscillations generated in the plasma from reaching the VTVM. The output voltage has been measured for different (E/P) values in air, where E is the axial filed, i.e. the voltage per cm length of the positive column and P is the pressure in Torr. The axial field E is determined by measuring the voltage between the two extra probes at a distance of 5 cm placed in the positive column. The variation of T_e with (E/P) has been presented in Fig. 1. The results are consistent with literature values (von-Engel[1]).

When a transverse magnetic field B is present, the plasma is compressed towards the wall and the radial distribution of charged particles changes. Sen and Gupta[2] have shown that, at a distance r from the axis, if n_B and n represent the electron densities in presence of and in absence of magnetic field respectively, then

$$n_B = n\exp(-aB)$$

$$\text{where} \qquad a = \frac{eE\,C_1^{1/2}\,r}{2KT_eP}$$

where the symbols have their usual significance and $C_1 = (e/m\,.\,L/v_r)^2$, L being the mean free path of the electron at a pressure of 1 Torr and v_r is the random velocity of the electron, so that C_1 is the square of mobility of the electron at 1 Torr. When $r = 0, a = 0, n_{0B} = n_0$, then as before, integrating we get,

$$\frac{KT_{eB}}{e} = \frac{V_{RB}}{\log[J_0(2.405\, r/R)\exp(-aB)]} \qquad \ldots (3)$$

The value of a has been calculated from the known values of T_e as obtained here and the calculated value of a is 0.0126.

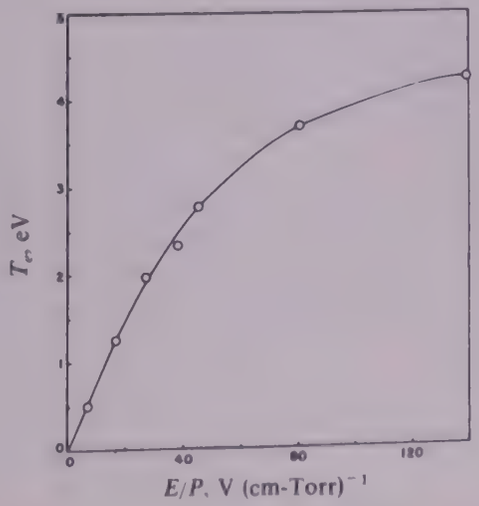

Fig. 1—Variation of T_e with E/P in air [$P = 1$ Torr]

Hence by placing the discharge tube in a transverse magnetic field, the electron temperature has been measured utilizing Eq. (3) for magnetic fields varying from 0 to 100 Gauss for a constant discharge current of 2.8 mA. It has been reported by Sadhya and Sen[3] that the theoretical experession:

$$\left[\frac{T_{eB}^2}{T_e^2} - 1\right] = C_1 \frac{B^2}{P^2} \qquad \ldots (4)$$

is valid for low values of magnetic field in case of hydrogen and helium. Table 1 shows the variation of $(T_{eB}^2/T_e^2 - 1)$ against B^2/P^2 in air. The agreement between theory and experiment is quite good for low values of magnetic field and the curve is a straight line from which the value of $C_1 = 1.67 \times 10^{-4}$. The quantity C_1 is the square of the mobility of the electron at 1 Torr and its calculated value is in agreement (at least in order of magnitude) with the value given by Brown[4] for the value of (E/P) reported here. This is a straightforward and simple method and the only quantity to be measured accurately is the voltage between the central probe $(r=0)$ and a parallel probe placed at a convenient distance. No further calculations are necessary and hence this method is more advantageous and accurate than the probe method. The error in the measurement of T_e is thus considerably minimized.

Further, the proposed method can be utilized for measurement of electron temperature in a magnetic field, specially for low values of (B/P). At high values of magnetic field Eq. (4) becomes invalid because the simplified assumptions of Beckman[5] from which the formula is derived no longer holds good.

Table 1—Variation of $(T_{eB}^2/T_e^2 - 1)$ With $(B^2/P^2) \times 10^{-3}$

$B^2/P^2 \times 10^{-3}$ G^2/Torr^2	$(T_{eB}^2/T_e^2 - 1)$
16	1.9
36	4.2
64	7.1
100	10.35
143.5	14.05

The purpose of this note is thus to show that the electron temperature in the positive column of a glow discharge can be calculated by measuring the radial dc voltage that develops between the probes due to the charge separation of electrons and ions subject to ambipolar diffusion, and the method of measurement can be extended in presence of magnetic field as well. The method is simple and straightforward and the possibility of error is minimized.

References

1 von-Engel A, *Ionised gases*, Second Edition (Oxford University Press, Oxford), 1965.

2 Sen S N & Gupta R N, *J Phys D (GB)*, **4** (1971) 510.

3 Sadhya S K & Sen S N, *J Phys D (GB)*, **13** (1980) 1275-1281.

4 Brown S C, *Basic data of plasma physics* (Technology Press, M.I.T. and John Wiley, New York), 1959.

5 Beckman L, *Proc Phys Soc London, (GB)*, **61** (1948) 515.

Indian Journal of Pure & Applied Physics
Vol. 21, October 1983, pp. 615-616

Excitation Energy-dependent Features in the *M*-X-ray-Emission Spectrum of Cerium

K S SRIVASTAVA, KIRTI SINHA,
A K SRIVASTAVA & M HUSAIN
Physics Department, Lucknow University,
Lucknow 226007

Received 8 *July* 1982; *revised received* 13 *June* 1983

An alternative explanation for the line-like structure, observed by Chamberlain *et al.* [*Phys Rev A* (*USA*). 9 (1974) 663] in the *M* series X-ray spectrum of Ce is given. Bohm and Pines theory of plasma oscillations in solids has been used to explain the variable energy positions of the resonant lines and the small structures on the low-energy side of the $M\alpha$ and $M\beta$ X-ray emission lines.

Attempts made by Liefeld *et al.*[1-3] to record the valence band $M\alpha$ and $M\beta$ X-ray emission lines of Ce were frustrated by the appearance, at less than threshold energy, of 'line-like structures', which masked the valence band lines. This line-like structure moves in energy position with the incident electron energy, resonates in intensity near the excitation energy of $M\alpha$ and $M\beta$ lines and leaves residual bumps on the low-energy side of these characteristic lines as the incident electron energy is increased well beyond the excitation energy of these lines. The energy difference between this stfucture and the corresponding incident electron energy is always about 5.0 $\pm$0.2 eV.

Considerable amount of experimental and theoretical work[1-9] has been done during the last few years to give possible explanations for the peculiar behaviour of these line-like structures. Lee and Pratt[6] have pointed out that to explain this line-like structure quantitatively, one should take into account the solid state and many-electron effects. Therefore, in the present note, we have tried to give an alternative explanation, using the Bohm and Pines theory of plasmon oscillations in solids.

Plasmon oscillations in solids theory—Chamberlain, Burr and Liefeld (CBL)[2] have regarded the solid state effects and characteristic electron energy losses to be of secondary importance. But, according to Lee and Pratt[6] and Kanski *et al.*[7-9], many-electron effects[10] should be included to account for the 4*f*-structures. Several workers[4,11] have observed the characteristic electron energy loss (CEEL) spectra in the bremsstrahlung isochromats and found that about 0.9 of the total cross-section for inelastic scattering is due to plasmon excitation and 0.1 accounts for other losses such as *K*- or *L*-shell excitations or bremsstrahlung, etc. This observation is in accord with Powell[12]. In the light of the above observations, characteristic electron energy losses cannot be overlooked.

On the basis of the Bohm and Pines theory[10], the '4*f*-structure' in the Ce emission spectrum is interpreted as the 'plasma loss peak' of the incident electron energy. Unfortunately, the experimental value of the plasmon energy of Ce is not known, but it can be calculated using the formula[13],

$$\hbar\omega_p = 28.8\sqrt{\frac{Z\sigma}{W}} \quad \text{(in eV)} \qquad \ldots (1)$$

where Z is the effective number of electrons taking part in the plasma oscillation, σ the specific gravity and W the molecular weight.

The outer configuration of ^{58}Ce is $4f^1 5d^1 6s^2$. The 4*f* levels are highly localized[14] and thus the 4*f* electron does not take part in the plasma oscillations. Also the two 6*s* electrons do not contribute because of the inert pair effect[15]. Hence for Ce, the effective value of Z is 1, $\sigma = 6.77$ and $W = 140.13$. Therefore, the value calculated from Eq. (1) is about 6.3 eV. This 6.3 eV loss can be correlated with the energy difference of 5.0 eV between the main line and the 4*f*-structure in the Ce isochromat of CBL[2]. Using plasma loss theory, the experimental curves of CBL[2] can be explained most successfully.

The incident electrons, while travelling through Ce, excite plasma oscillations which require an energy of about 6.3 eV. Thus we get a plasma loss peak on the low-energy side (5.0 eV) of the threshold energy. As the excitation energy increases, the intensity of this plasma loss peak also increases and it moves because it has to be always at an energy distance of about 6.3 eV from the threshold energy. When excitation energy is equal to the inner-shell ionization energy of M_V level (882.5 eV), the $M\alpha$ line is excited and the plasma loss peak is at $\simeq$876.5 eV.

After the $M\alpha$ line (882.5 eV) is excited, part of its radiated energy may also be used in exciting plasma oscillations, which gives a low-energy plasmon satellite peak at $\simeq$876.5 eV. Here the peaks of the plasma loss and the plasmon satellite overlap and we get an enormous increase in intensity. This explains the observed intensity resonance at 876.5 eV energy. As the excitation energy is further increased above 882.5 eV, the position of the plasma loss peaks shifts but the low-energy plasmon satellite peak has its position fixed with respect to that of the main $M\alpha$ line. Thus the small

structures observed by CBL[2] at high excitation energies can be considered as low energy plasmon satellites. Exactly the same phenomena will take place when the excitation energy approaches the inner-shell ionization energy of M_{IV} level (898.7 eV). The $M\beta$ line is emitted and the plasma loss peak will be $\simeq 892.4$ eV. When excitation energy is equal to 898.7 eV, the low-energy plasmon satellite is excited at about 892 eV and coincides with the plasma loss peak. This gives the second intensity resonance observed by CBL[2]. Also, when the excitation energy is greater than 898.7 eV, this low-energy plasmon satellite forms the second small structure on the low-energy side of the $M\beta$ line. Thus, this theory successfully explains why the small structures are found at two places.

The estimation of the relative intensity of the small-structures with respect to the main emission line also supports the view that the small structures are the low-energy plasmon satellites.

Recently, Langreth[16] and Srivastava *et al.*[13] have shown that the relative intensity of the plasmon satellite is given by

$$i = 0.166\, r_s \qquad \ldots (2)$$

where $$r_s = \left(\frac{47.11}{\hbar\omega_p}\right)^{2\,3} \qquad \ldots (3)$$

Using Eqs. (1)-(3), the relative intensity of the low-energy plasmon satellite has been calculated to be 0.63, which is in good agreement with the estimated value 0.6 from the experimental curve of CBL[2]. Thus the present assignment of the residual bumps as low-energy plasmon satellites is fairly good.

Thanks are due to Prof. B G Gokhale, Physics Department, Lucknow University, for helpful discussions, and to the UP State Council of Science and Technology, Lucknow, and the CSIR, New Delhi for financial assistance. The authors are also thankful to Dr J Kanski for sending us the preprints of his papers mentioned at Refs. 8 and 9.

References

1 Liefeld R J, Burr A F & Chamberlain M B, *Phys Rev A (USA)*, **9** (1974) 316.

2 Chamberlain M B, Burr A F & Liefeld R J, *Phys Rev A (USA)*, **9** (1974) 663.

3 Liefeld R J & Burr A F, *International conference on the physics of X-ray spectra* (National Bureau of Standards, Washington), 1976, 95.

4 Ulmer K, X-ray continua near the high frequency limit in *X-ray spectra and electronic structure of matter*, Vol. II (Kiev Institute of Physics of Metals, Kiev, USSR), 1969, 79.

5 Turtle R R & Liefeld R J, *Phys Rev B (USA)*, **7** (1973) 3411.

6 Lee C M & Pratt R H, *Phys Rev A (USA)*, **12** (1975) 707.

7 Kanski J & Nilson P O, *Phys Rev Lett (USA)*, **43** (1979) 1185.

8 Kanski J & Wendin G, *Phys Rev B (USA)*, in press.

9 Kanski J & Nilson P O, *J Phys F (GB)*, in press.

10 Bohm D & Pines D, *Phys Rev (USA)*, **92** (1953) 609.

11 Best P E & Chu C C, *International conference on the physics of X-ray spectra* (National Bureau of Standards, Washington), 1976, 98.

12 Powell C J, *Surf Sci (Netherlands)*, **44** (1974) 29.

13 Srivastava K S, Shrivastava R L, Harsh O K & Kumar V, *Phys Rev B (USA)*, **19** (1979) 4336.

14 Kanski J, Nilson P O & Curelaru I, *International conference on the physics of X-ray spectra* (National Bureau of Standards, Washington), 1976, 102.

15 Brown G I, *A new guide to modern valency theory* (English Language Book Society, London), 3rd Edn, 1975, 39.

16 Langreth D C, *Proceedings of the 24th Nobel symposium*, edited by B Lundquist and S Lundquist (Academic Press, New York), **24** (1973), 210; *Collective properties of physical systems* (Academic Press, New York), 1974.

Indian Journal of Pure & Applied Physics
Vol. 21, October 1983, pp. 617-618

New Spectrum of NiCl Molecule

P M SHAH, A B DARJI & N R SHAH
Physics Department, M S University of Baroda, Baroda 390 002

Received 10 *January* 1983

The spectrum of NiCl molecule has been excited in high frequency discharge and recorded, for the first time in the range 5700-5930 Å, using plane grating spectrograph at 3.43 Å/mm. Thirty-one bands have been analyzed to form five fragmentary systems and vibrational constants are reported.

The spectrum of NiCl molecule is known to be consisting of several fragmentary systems designed by various workers[1-9] as A_1, A_2, A_3, B_1, B_2, C, D, E_1 and E_2 starting from shorter wavelength side in the range 3900-8750 Å. In addition to this, Rao *et al.*[6] observed a few more band systems in the region 6350-8750 Å. They have designated them as F, G, H, I and J systems. Further, Rao and Rao[7] have reported four more systems I, II, III and IV in the region 4860-5490 Å. Darji and Shah[9] reported five systems in the ultraviolet region 3440-3950 Å comprising α, β, γ, δ, and A_0 systems. Gopal[10] has recently reported additional bands in B_1 and B_2 systems by exciting the molecule in thermal emission.

In continuation of their previous work on the spectrum of NiCl, the authors have observed new bands in the range 5700-5930 Å, and the results obtained from their vibrational analysis are reported here.

The spectrum of NiCl was excited in a high frequency discharge tube source as described in our previous paper[9]. It was recorded in the second order of a plane grating spectrograph at a reciprocal dispersion of 3.43 Å/mm. The spectrum in the region 5700-5930 Å reveals, for the first time, the presence of 31 single headed bands having abruptly varying intensity. They are superposed by strong atomic lines of nickel. While analyzing the bands it has not been found possible to arrange all the observed bands into a single system. The bands have been analyzed to form five fragmentary systems having a few progressions and short sequences. By taking the bands at 16874.6, 16911.2, 17015.2, 17050.9, and 17100.7 cm^{-1} as the 0,0 bands, the vibrational analysis has been carried out. The band-head data of the bands analyzed here are given in Table 1. The vibrational constants evaluated from the analysis are given in Table 2.

The analysis indicates that the approximate vibrational frequencies of the upper and lower states of the various systems agree well with the known vibrational frequencies of the NiCl molecule. However, the nature of electronic states involved cannot be suggested unambiguously without rotational analysis. The authors have attempted a rotational analysis of some suitable bands and the results shall be published shortly.

Table 1—Band-Head Data of NiCl in the Region 5700-5950 Å

System	Relative intensity	Wavenumber in vacuum (ν) cm^{-1}	Assignment v', v''	$\nu_{obs} - \nu_{calc}$ cm^{-1}
	2	17655.9	2,0	−0.1
	3	17267.4	1.0	0.0
	1	17257.9	2,1	0.4
IX	5	16874.6	0,0	0.0
	2	16868.8	1,1	−0.1
	1	16860.5	2,2	−0.1
	2	16476.8	0,1	0.1
	3	17678.9	2,0	0.0
	3	17295.9	1,0	−0.1
	1	17280.4	2,1	−0.3
VII	6	16911.2	0,0	0.0
	3	16897.1	1,1	−0.5
	2	16885.6	2,2	0.8
	2	16513.2	0,1	0.2
	2	17805.3	2,0	−0.6
	1	17778.0	3,1	0.6
	3	17412.1	1,0	0.0
VII	1	17386.1	2,1	−0.4
	4	17015.2	0,0	0.0
	2	16992.8	1,1	−0.1
	1	16969.8	2,2	0.2
	2	16596.0	0,1	−0.1
	2	17442.2	1,0	−0.2
	1	17425.6	2,1	0.5
	5	17050.9	0,0	0.0
VI	3	17039.8	1,1	0.4
	2	16648.1	0,1	−0.8
	1	16638.1	1.2	0.9
	2	17100.7	0,0	—
V	1	17075.3	1,1	—
	1	17060.4	2,2	—

Table 2—Vibrational Constants (in cm^{-1}) of NiCl

System	ν_e	ω_e'	ω_e''	$\omega_e'x_e'$	$\omega_e''x_e''$
IX	16876.5	397.0	400.1	2.1	0.80
VIII	16918.3	386.1	400.5	0.75	1.15
VII	17026.0	400.0	421.3	1.55	1.05
VI	17054.8	397.3	403.8	2.80	0.40
V	—	400.6	—	—	—

References

1 More K R, *Phys Rev* (*USA*), **54** (1938) 122-125.

2 Mesnage P, *Ann Phys* (*France*), **12** (1939) 5-87.

3 Krishnamurty V G, *Indian J Phys*, **29** (1952) 207-225.

4 Reddy S P & Rao P T, *Proc Phys Soc Lond* (*GB*), **75** (1960) 275-279.

5 Bulewicz E M & Phillips L F, *Trans Faraday Soc* (*GB*), **57** (1961) 921-931.

6 Rao S V, Reddy S P & Rao P T, *Z Phys* (*Germany*), **166** (1962) 261-264.

7 Rao N V K & Rao P T, *Curr Sci* (*India*), **38** (1969) 589.

8 Darji A B & Shah N R, *Curr Sci* (*India*), **48** (1979) 809-810.

9 Darji A B & Shah N R, *Indian J Pure & Appl Phys*, **18** (1980) 802-805.

10 Gopal R, *Curr Sci* (*India*), **50** (1981) 854.

INSTRUCTIONS TO AUTHORS

SCOPE

The journal welcomes, for publication, full papers and short notes, reporting significant new results of research, in all areas of physics except space physics. The applied fields covered are electronics, electrical engineering, instrumentation and applied mathematics. However, papers in applied mathematics with emphasis on only derivation and proofs and having no direct physical significance, will not be considered. Review articles are not published normally.

SUBMISSION OF MANUSCRIPT

Manuscripts for consideration should be submitted, *in duplicate*, to Editor, Indian Journal of Pure & Applied Physics, Publications & Information Directorate, Hillside Road, New Delhi 110012. They should neither have been already published nor be under consideration elsewhere.

Manuscripts should be in English and typewritten on only one side of good quality paper, in double space, with adequate margin on all four sides. One original and one carbon or photo-copy, each complete in all respects including abstract, illustrations, appendixes, etc. are to be submitted.

PREPARATION OF MANUSCRIPT

Authors may consult recent issues of the Journal to familiarize themselves with the general style and practices adopted in regard to the various elements of a paper.

General

Manuscript should be presented in as concise a form as possible. Good attention should be given to spelling and grammar. In giving names of chemical compounds and structures, abbreviations of units of measurements, symbols and notations, the style and practices recommended by the IUPAP and IUPAC, should be followed.

Frequently repeating combinations of words, e.g. electric field gradient (EFG), junction field effect transistor (JFET), stimulated Raman emission (SRE), should be abbreviated subsequently, indicating the abbreviated form in parenthesis, as shown, at the place of their first occurrence.

Pages should be numbered consecutively and arranged in the following order: Title, authors' names with their institutional affiliations and abstract, along with relevant footnotes whenever necessary (on a separate sheet); introduction; experimental details/theory/method/analysis; results; discussion; conclusion(s); acknowledgement; references and appendixes. Tables, captions for figures (with legends) and appendixes should be typed *on separate sheets* and attached at the end of the manuscript.

Title

The title should be neither too brief/general nor unnecessarily long. It should reflect the content of the paper so as to derive the maximum advantage in indexing. If a paper forms part of a general series, a specific subtitle, indicating the particular aspect of the work covered in the paper, should be provided.

A short running title for the paper, the broad subject heading under which it should be classified in the contents page (authors may consult recent numbers of the journal for this purpose), and the author (indicated by an asterisk on the relevant author's name) and address for correspondence, should also be provided on the title page.

Abstract

The abstract, usually not exceeding 200 words, should indicate the scope and significant content of the paper, highlighting the principal findings and conclusions. It should be in such a form that abstracting periodicals can use it without modification.

Introduction

Long and elaborate introduction should be avoided. It should be brief and state the exact scope of the study in relation to the present status of knowledge in the field. Literature review should be limited strictly to what is necessary to indicate the essential background and the justification for undertaking the study.

Materials, methods, apparatus, etc.

The sources of materials and their purity, methods of preparation, procedure for measurements and their accuracies, etc. should be clearly stated to enable any other worker to repeat the work if necessary. New methods, techniques, theories, etc. should be described in adequate detail; but if they are well known, a mere literature reference to them will do; differences from standard ones, improvements or innovations should, however, be clearly mentioned.

Results

Only such primary data as are essential for understanding the discussion and main conclusions emerging from the study should be included. All secondary data as are of interest to a specific category of readership *should not be included* in the paper. Such data should be retained by the authors for supply, on request, to any interested research worker. A footnote to this effect may be inserted at the relevant place in the paper.

The results must be presented in a coherent sequence in a unified logical structure, avoiding repetition or confusion. Limitations of the results should be clearly stated.

The same data should not be presented in both tabular and graphic forms. Only such tables and figures as are essential should be included. Simple linear plots that can easily be discussed in the text, should not be included. Infrared, ultraviolet, NMR and other spectra, DTA curves, etc. should be included only if they pertain to new compounds and/or are essential to the discussion; otherwise only significant numerical data should be given in the text or in a table.

Discussion

Long rambling discussion should be avoided. The discussion should deal with the interpretation of results without repeating information already presented under results. It should relate new findings to the known and include logical deductions. A separate section on 'conclusions' can be given only when they are well established and of outstanding significance. Mere observation of qualitative trends of results should be distinguished from firm conclusions. Also, limitations, if any, to the conclusions should be clearly pointed out.

Mathematical portions

Special attention should be given to the mathematical portions of the paper. Equations must be well separated from the text and written clearly with good separation between the successive lines. The usual norms of breaking long mathematical expressions should be adhered to. Equations should be numbered consecutively in Arabic numerals with the number in parenthesis near the right hand margin. Superscripts and subscripts should be clearly indicated in pencil by V and Λ sign respectively. Capital and small letters,

particularly of the same letter when both occur, as well as letters or *symbols likely to be confused* one for the other, *should be* clearly *distinguished*. Special characters (e.g. Greek, script, vector, tensor, etc.) required must be indicated by marginal notes. Letters and symbols which should appear in bold face must be clearly indicated. To simplify typesetting: (i) long and complicated mathematical expressions which are frequently repeated should be replaced with single letter/symbol, *without clashing with the others used* in the paper; (ii) the "exp" form of complex exponential functions should be used; and (iii) to simplify fractions, the solidus (/) is to be used and fractional exponents are to be used instead of root signs, e.g.

write $\exp\{-i\omega_0(t_1-t_2)/2\}$ and *not* $e^{-i\omega_0(t_1-t_2)/2}$

write $(4\omega_{pl} K_{3\lambda}^2/\tilde{\omega} K_D^2)^{1/2}$ and *not* $\sqrt{\dfrac{4\omega_{pl} K_{3\lambda}^2}{\tilde{\omega} K_D^2}}$

Tables

Tables should be numbered consecutively in Arabic numerals and *should bear brief titles. Column headings should be brief*. Units of measurement should be abbreviated and placed below the headings. Nil results should be indicated and distinguished clearly from absence of data. Inclusion of structural formulae inside the tables should be avoided as far as possible. Tables should be referred to in the text by numbers and not by terms like 'above', 'below', 'preceding' or 'following'. Results should not be presented to a greater accuracy than that of the method employed.

Illustrations

The number of illustrations should be kept to the minimum. Wherever possible, e.g. a number of individual analogous figures referring to different variables, substances, molecules, etc. may be combined into one composite figure. All illustrations should be numbered consecutively in Arabic numerals. *Captions and legends* to the figures should be *self-explanatory*. Line drawings should be made with Indian ink on white drawing paper/cellophane sheet/tracing cloth, and drawn to approximately twice the printed size.

The lettering should be uniform, preferably in stencil, so as to be *not less than* 1.5 *mm after reduction* widthwise to full page size (165 mm) or column size (80 mm). The size of geometrical shapes (used to distinguish different graphs), dots, lines, etc. should be sufficiently *large to permit* the necessary *reduction without loss of detail*. In the case of photographs, *prints must be on glossy paper and contrasty*. If an illustration is taken from another publication, reference to the source should be given and prior permission secured. Illustrations should be referred to in the text by numbers and not by terms like 'above', 'following' etc.

Acknowledgement

Acknowledgements should not be exuberant and must be made only to real assistance rendered in connection with the work reported in the paper.

References

References cited should be limited to the absolute minimum (particularly in the case of short notes) based on their essential relevance. In the text, references to literature should be *numbered consecutively, in the order of their first occurrence*, and should be indicated by superscript Arabic numbers at the relevant places; as far as possible the placement of references on numerals or other symbols should be avoided; in such cases the reference may be given in parenthesis in running text, e.g. "this yielded for n a value of 2.3 (Ref. 5)". Full bibliographic details for all the references mentioned in the text should be listed in serial order at the end of the paper.

In citing references to research papers, names and initials of authors should be followed, in order, by the title of the periodical in the abbreviated form (underlined), the volume number (two lines underneath), the year within circular brackets and the page number [e.g. Chandra B P & Shrivastava K K, *J Phys & Chem Solids (GB)*, 39 (1978) 939]. For names of periodicals, the abbreviations followed by the *Physics Abstracts* should be used. For periodicals not covered by *Physics Abstracts*, the title abbreviations should be according to the *Bibliographic Guide for Editors and Authors*, 1974, published by the American Chemical Society, Washington DC, USA; additionally the country from which the journal is published should be given in parenthesis immediately after the title abbreviation. If a paper has been accepted for publication, the names of the authors and the journal (with volume number and year, if known) should be given followed by the words "in press" [e.g. Wahi P K & Patel N D, *Can J Spectrosc (Canada)*, in press.].

In references containing *up to four authors*, the *names of all* the *authors* with their respective initials should *be given*. The abbreviations *et al.*, idem and ibid should be avoided. When there are more than four authors, *only* the names of the *first three authors* with their respective initials should *be given*, followed by the words '*et al.*'

Reference to a book should include details in the following order: name and initials of authors, the title of the book (underlined), name of publisher and place of publication within circular brackets and year and page (s) [e.g. Clayton G B, *Operational amplifiers* (Newnes-Butterworths, London), 4th Edn, 1977, 26]. If the reference is to the work of an author published in a book by a different person, the fact that it is cited from the source book should be clearly indicated [e.g. Turnhout Van J, 'Thermally stimulated discharge of electrets' in *Topics in applied physics*: Vol. 33—*Electrets*, edited by C M Sessler (Springer Verlag, Berlin), 1980, 130].

Proceedings of conferences and symposia should be treated in the same manner as books. Reference to a paper presented at a conference, the proceedings of which are not published, should include, in the following order, names and initials of authors, title of the paper (underlined), name of the conference, and where and when it was held (e.g. Herczeg P, *Symmetry-violating kaon decays*, paper presented to the International Conference on High Energy Physics and Nuclear Structure, Vancouver, Canada, 13-17 August 1979).

Reference to a thesis should include the name of the author, title of the thesis (underlined), university or institution to which it was submitted and year of submission (e.g. Mehrotra S N, *Many-body techniques and their applications to interacting bosons*, Ph D thesis, Ranchi University, 1976).

Reference to a patent should include names of patentees, country of origin (underlined) and patent number, the organization to which the patent has been assigned (within circular brackets), date of acceptance of the patent and reference to an abstracting periodical where available [e.g. Labes M M, *US Pat.* 4,066,567 (to Temple University), 3 January 1978; *Chem. Abstr.*, **88** (No. 20) (1978), 138350 n].

PROOFS & REPRINTS

Authors will receive galley proofs and a reprint order form. The galley proofs, indicating the essential corrections, should be returned to the Editor without delay, enclosing the reprint order form. Authors are given 25 *free reprints* for each paper. *Extra* reprints can be had *at cost. If the reprint order is not received with the corrected proofs, it will be presumed that the author needs no extra reprints.* Later requests for *more* reprints cannot be complied with. Covers for reprints cannot be provided.

THE WEALTH OF INDIA

An Encyclopaedia of Indian Raw Materials and Industrial Products, published in two series: **(i) Raw Materials**, and **(ii) Industrial Products**.

RAW MATERIALS

The articles deal with Animal Products, Dyes & Tans, Essential Oils, Fats & Oils, Fibres & Pulps, Foods & Fodders, Drugs, Minerals, Spices & Flavourings, and Timbers and other Forest products. Names in Indian languages, and trade names are provided.

For important crops, their origin, distribution, evolution of cultivated types, and methods of cultivation, harvesting and storage are mentioned in detail. Data regarding area and yield and import and export are provided. Regarding minerals, their occurrence and distribution in the country and modes of exploitation and utilization are given. The articles are well illustrated. Adequate literature references are provided.

Eleven volumes of the series covering letters A–Z have been published.

Vol. I(A-B) Rs. 80.00; Vol. II (C) Rs. 95.00; Vol. III (D-E) Rs. 105.00; Vol. IV (F-G) Rs. 65.00; Vol. IV: Suppl. Fish & Fisheries Rs. 40.00; Vol. V (H-K) Rs. 75.00; Vol. VI (L-M) Rs. 90.00; Vol. VI: Suppl. Livestock Rs. 60.00; Vol. VII (N-Pc) Rs. 30.00; Vol. VIII (Ph-Re) Rs. 86.00; Vol. IX (Rh-So) Rs. 104.00; Vol. X (Sp-W) Rs. 152.00; Vol. XI (X-Z) Rs. 102.00.

INDUSTRIAL PRODUCTS

Includes articles giving a comprehensive account of various large, medium and small scale industries. Some of the major industries included are: Acids, Carriages, Diesel Engines, Fertilizers, Insecticides & Pesticides, Iron & Steel, Paints & Varnishes, Petroleum Refining, Pharmaceuticals, Plastics, Ship & Boat-building, Rubber, Silk, etc.

The articles include an account of the raw materials and their availability, manufacturing processes, and uses of products, and industrial potentialities. Specifications of raw materials as well as finished products and statistical data regarding production, demand, exports, imports, prices, etc., are provided. The articles are suitably illustrated. References to the sources of information are provided.

Nine volumes of the series covering letters A–Z have been published.

Part I (A-B) Rs. 54.00; Part II (C) Rs. 64.00; Part III (D-E) Rs. 25.00; Part IV (F-H) Rs. 25.00; Part V (I-L) Rs. 30.00; Part VI (M-Pi) Rs. 28.00; Part VII (Pl-Sh) Rs. 60.00; Part VIII (Si-Ti) Rs. 66.00; Part IX (To-Z) Rs. 80.00.

HINDI EDITION: BHARAT KI SAMPADA—PRAKRITIK PADARTH

Vols. I to VI and two supplements of Wealth of India—Raw Materials series in Hindi already published.

Published Volumes:

Vol. I (अ-औ) Rs. 38; Vol. II (क) Rs. 36; Vol. III (ख-न) Rs. 36; Vol. IV (प) Rs. 83; Vol. V (फ-मेरे) Rs. 60; Vol. VI (मेल-ह) Rs. 80.

Supplements:

Fish & Fisheries (Matsya & Matsyaki) Rs. 49; Liverstock (*Pashudhan aur Kukkut Palan*) Rs. 34.

Vols. VII to XI under publication.

Please contact:

Manager (Sales & Advertisement)

PUBLICATIONS & INFORMATION DIRECTORATE, CSIR

Hillside Road, New Delhi 110012

RN 7092/63

CSIR PUBLICATIONS

WEALTH OF INDIA

An encyclopaedia of the economic products and industrial resources of India issued in two series.

RAW MATERIALS SERIES—contains articles on plant, animal and mineral resources

	Rs	$	£
Vol. I (A-B)	80.00	30.00	13.00
Vol. II (C)	95.00	33.00	17.00
Vol. III (D-E)	105.00	32.00	20.00
Vol. IV (F-G)	65.00	27.00	12.00
Supplement (Fish & Fisheries)	40.00	16.00	7.00
Vol. V (H-K)	75.00	28.00	12.50
Vol. VI (L-M)	90.00	34.00	15.00
Supplement (Livestock)	60.00	18.00	6.00
Vol. VII (N-Pe)	30.00	9.00	3.00
Vol. VIII (Ph-Re)	86.00	32.00	14.00
Vol. IX (Rh-So)	104.00	35.00	19.00
Vol. X (Sp-W)	152.00	65.00	23.00
Vol. XI (X-Z)	102.00	42.00	20.00

INDUSTRIAL PRODUCTS SERIES—deals with major, small-scale and cottage industries

Part I (A-B)	54.00	20.00	9.00
Part II (C)	64.00	24.00	11.00
Part III (D-E)	25.00	7.50	2.50
Part IV (F-H)	25.00	7.50	2.50
Part V(I-L)	30.00	9.00	3.00
Part VI (M-Pi)	28.00	8.00	2.80
Part VII (Pl-Sh)	60.00	18.00	6.00
Part VIII (Si-Ti)	66.00	27.00	10.00
Part IX (To-Z)	80.00	34.00	12.00

BHARAT KI SAMPADA (Hindi Edition of Wealth of India, Raw Materials)

Vol. I (अ-औ)	38.00	16.00	6.50
Vol. II (क)	36.00	15.00	6.00
Vol. III (ख-न)	36.00	15.00	6.00
Vol. IV (प)	83.00	34.00	16.00
Vol. V (फ-मेरे)	60.00	22.00	10.00
Vol VI (मेल-ह)	80.00	27.00	13.00
Livestock (Kukkut Palan)	34.00	15.00	6.00
Fish & Fisheries (Matsya aur Matsyaki)	49.00	21.00	8.00
A Dictionary of Generic & Specific Names of Plants and Animals Useful to Man with their English and Latin pronunciation in Devanagari.	30.00	11.00	5.00

OTHER PUBLICATIONS

	Rs	$	£
Proceedings seminar on primary communications in Science & Technology in India by Sh. R.N. Sharma & S. Seetharama	52.00	17.50	9.00
Flora of Delhi by J.K. Maheshwari	28.00	8.00	2.80
Indian Fossil Pteridophytes by K.R. Surange	23.00	8.00	2.30
Indian Thysanoptera by T.N. Ananthakrishnan	26.00	8.00	2.60
The Millipede Thyropygus by G. Krishnan	12.00	3.50	1.20
Drug Addiction with special reference to India by R.N. Chopra & I.C. Chopra	12.00	3.50	1.20
Glossary of Indian Medicinal Plants by R.N. Chopra & I.C. Chopra	35.00	13.00	6.00
Fluidization & Related Processes	12.00	4.00	1.20
Evolution of Life by M.S. Randhawa, A.K. Dey, Jagjit Singh & Vishnu Mitre	22.50	7.00	2.25
Collected Scientific Papers of Meghnad Saha	30.00	9.00	3.00
Proteaceae by C. Venkata Rao	34.00	11.00	3.40
Pinus by P. Maheshwari & R.N. Konar	30.00	11.00	5.00
Cellulose Research I	3.00	0.90	0.30
Cellulose Research II	6.00	1.75	0.60
Chemical Process Design	9.00	2.50	0.90
Low Temperature Carbonization of Non-coking Coals & Lignites & Briquetting Coal Fines:			
Vol. I	17.50	5.50	1.75
Vol. II	17.50	5.50	1.75
Nucleic Acids	10.00	3.00	1.00
IGY Symposium: Vol. I	9.00	2.50	0.90
IGY Symposium: Vol. II	9.00	2.50	0.90
CNS Drugs	16.50	5.00	1.65
Kinetics of Electrode Processes & Null Points of Metals	2.50	0.75	0.25
Indian Sardines by R.V. Nair	22.00	7.00	2.20
Termite Problems in India	9.00	3.00	0.90
Loranthaceae by B.M. Johri & S.P. Bhatnagar	32.00	11.00	3.20
Abies and Picea by K.A. Chowdhury	14.00	6.00	2.10
Gnetum by P. Maheshwari and Vimla Vasil	20.00	6.00	2.00
Aquatic Angiosperms by K. Subramanyam	20.00	6.00	2.00
Supplement to Glossary of Indian Medicinal Plants by R.N. Chopra, I.C. Chopra & B.S. Varma	18.00	7.00	3.00
Herbaceous Flora of Dehra Dun by C.R. Babu	144.00	60.00	22.00
Diosgenin and Other Steroid Drug Precursors by Y.R. Chadha & Miss L.V. Asolkar	36.00	13.00	6.00
Research & Development Management by Inder Dev	25.00	10.00	—
Rural Development and Technology—A Status Report-cum-Bibliography by P.R. Bose & V.N. Vashist	100.00	38.00	17.00

Packing and Postage extra

Please contact:

Manager (Sales & Advertisement)

PUBLICATIONS & INFORMATION DIRECTORATE, CSIR

Hillside Road, New Delhi 110012

Printed & Published by D.S. Sastry, Editor, Publications & Information Directorate (PID)
Hillside Road, New Delhi 110012, at PID Photocomposition Unit

D(C)540